

Bridging pico-to-nanoNewton: Ratiometric Force Probe for Nanoscale Polymer Physics Before Damage

Ryota Kotani¹, Soichi Yokoyama¹, Shunpei Nobusue², Shigehiro Yamaguchi³, Atsuhiko Osuka¹, Hiroshi Yabu^{4*}, Shohei Saito^{1,5*}

Affiliations:

¹Graduate School of Science, Kyoto University, Kyoto 606-8502, Japan.

²Institute of Advanced Energy, Kyoto University, Uji 611-0011, Japan.

³Graduate School of Science, Nagoya University, Nagoya 464-8602, Japan.

⁴WPI-Advanced Institute for Materials Research (AIMR), Tohoku University, Sendai 980-8577, Japan.

⁵PRESTO, Japan Science and Technology Agency, Kyoto 606-8502, Japan

Abstract: Understanding nanoscale force transmission in pico-to-nanoNewton range is important in polymer physics. While physical approaches have limitations to analyze local force distribution in condensed environments, chemical doping of mechano-probes is promising. However, there are demanding requirements to probe the local force without structural damage, which corresponds to the force range below covalent bond scission (nanoNewton) and over thermal fluctuation (picoNewton). Here we report a conformationally flexible dual fluorescent mechano-probe with 100-picoNewton threshold that realizes ratiometric analysis on nanoscale force distribution in stretched polymer chain network. Without changing original polymer properties, the force distribution has been reversibly monitored in real time. Chemical control of the probe location demonstrated that local stress concentration is twice more biased at crosslinkers than main chains particularly in a strain-hardening region. Due to the sensitive response, proportion of the stressed force probe was estimated more than 1000 times higher than activation ratio of conventional mechanophores.

Main Text:

Understanding pico-to-nanoNewton force transmission in complex hierarchical structures is a main goal in polymer physics (1) and mechanobiology (2). Physical approaches such as optical/magnetic tweezers and atomic force microscopy (AFM) are widely used to evaluate picoNewton force, while these techniques have difficulty in acquiring force distribution inside condensed materials or molecular crowding environments (Fig. 1A). (3) Instruments of surface force apparatus (SFA), rheometer, and tensile testing machine are also available for studying more than microNewton force transmitted in meso-to-macroscopic structures, but direct quantification method of molecular-level force distribution is still being pursued. Promising alternative is a chemical doping of mechanoresponsive molecules as a force probe (4). Those chromophores for materials- and biology-oriented purposes have been independently developed in this decades, because the force ranges of interest are different in these fields. While FRET-type chromophore conjugates have been developed to analyze several picoNewton in mechanobiology (5-8), a variety of mechanophores show responses in several nanoNewton with an internal covalent bond scission (9-12), giving rise to the upsurge of stress-responsive materials (13-20). On the other hand, there

are still severe requisites in the design of a force probe that can realize quantitative monitoring of local stress concentration before damage of polymer chain network, without changing original polymer properties by covalent doping. Although sacrificial bond scission of polymer materials has been monitored using turn-on mechanophores (21,22), nanoscale force distribution in entangled polymer chains has not been elucidated, in spite of the importance for reasonable design of unique tough materials (23-27). Target force range for this purpose is around 10–100 piconewton, below covalent bond scission (several nanonewton) and beyond spontaneous thermal fluctuation at room temperature ($k_B T = 4.1$ pN nm) (28) (Fig. 1B). Here we demonstrate that a conformationally flexible flapping mechano-probe enables this study by ratiometric analysis of its bright dual fluorescence, in which well-suited potential energy profiles are designed in the ground state (S_0) and the lowest singlet excited state (S_1). High brightness permits minimum chemical doping to preserve original polymer properties. By controlling chemical locations of the probe in crosslinked polymers, new quantitative insights into biased nanoscale stress concentration have been obtained through real-time observation of the dual emission from the stretched polymers.

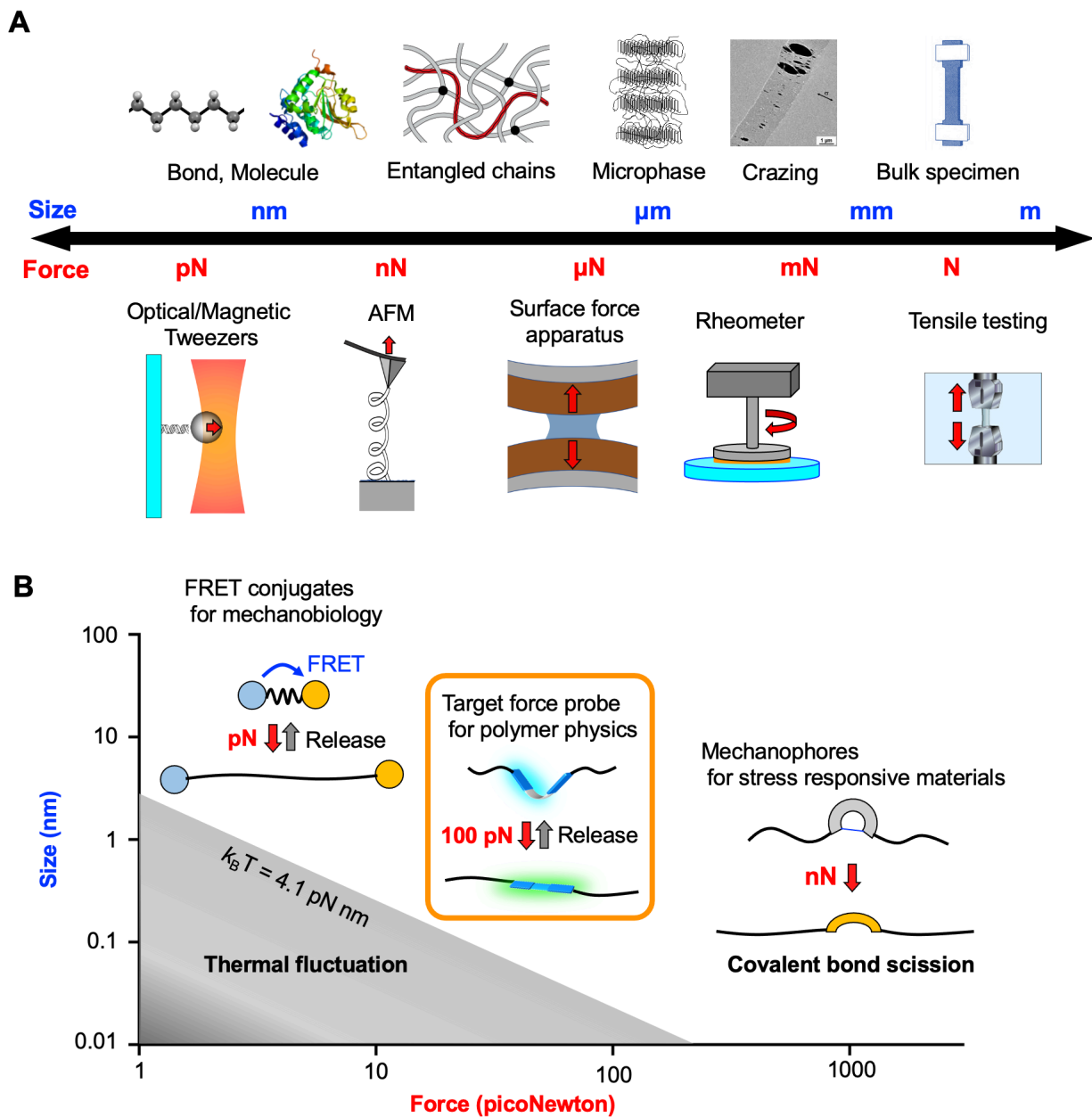


Fig. 1. A) Hierarchical structures of materials and physical measurement methods of mechanical force in different scales. B) Target force range for nanoscale study of polymer physics.

Dual fluorescent flapping molecular probe

A flapping molecule (FLAP), composed of two rigid anthraceneimide wings fused with a conformationally flexible eight-membered ring (cyclooctatetraene, COT), shows dual fluorescence (FL) property (Fig. 2A,B) (29). In S_0 , a bent form is most stable, while a planar form has higher energy due to strain effects of the flat COT ring (30). On the other hand, FLAP has two energy minima in S_1 at bent and planar geometries. Emissions from these minima are both allowed, exhibiting a blue FL around 460 nm and a green FL around 520 nm, respectively. Since the energy barrier is low and the planar geometry is slightly more stable in S_1 , FLAP takes a bent-to-planar conformational change within subnanosecond timescale after UV excitation in a solution phase (31), emitting the green FL dominantly with high FL quantum yield ($\Phi_F \approx 0.3$). Population of excited species at these S_1 minima are largely dependent on local viscosity in solution, while polarity dependence can be ignored due to the non-charge-transfer character. Whereas the viscosity probing function is active in the presence of solvent molecules, the planarization dynamics crossing the barrier in S_1 is suppressed in a polymer matrix, and then the blue FL is only observed ($\Phi_F \approx 0.3$). On the other hand, compulsory planarization in S_0 can be induced by external force, as we demonstrated the mechanophore function in a crystal phase transition of FLAP (32). Among conformationally flexible mechanophores that can show detectable signals without covalent bond scission (33-35), FLAP is unique in its dual FL property, which enables ratiometric FL analysis (Fig. 2B). Although a variety of single-component dual-fluorescent chromophores have been reported in photochemistry (36, 37), the force probe application has not been reported. By the ratiometric FL analysis, quantitative evaluation can be realized even when the molecular force probes are distributed heterogeneously and the concentration of the probe changes by polymer deformation.

100-pN threshold for the fluorescence switching before covalent bond elongation

Flapping mechanophores bearing OH groups were prepared for covalent doping in polycarbonate (PC) and polyurethane (PU). Terminal bulky substituents were introduced for suppressing aggregation of FLAPs (38). Due to the high brightness, doping ratio can be minimized less than 10^{-4} equivalent to other monomer components. Original mechanical properties of host polymers were preserved by the covalent doping (Fig. S20 for PC and Fig. S27 for PU), which is the essential requisite for a force probe. Average distance between doped FLAPs was estimated to be ≈ 20 nm, much farther than the distance allowed for Förster resonance energy transfer (FRET, < 10 nm). Negative control experiments by the corresponding physical doping confirmed almost no mechanical response of FLAP (Fig. S38). Its sensitive mechanical response was confirmed in chemically doped polymeric environments. A linear PC prepared from the components in Fig. 2C showed less elastomeric property, rather glassy with glass transition temperature T_g of 153 °C (Fig. S19), thereby permitting microscopy observation with small displacement. When the notched PC film was slowly stretched over the inverted microscopy, equipped with a compact tensile testing machine and a hyperspectral camera, rapid growth of stressed region was visualized in micro-to-millimeter scale by a FL change from bluish to greenish colors under UV light. Two-dimensional imaging as a function of the FL intensity ratio at 525 and 470 nm made the situation clearer. The spectral response started much earlier than crack propagation from the notch (Fig. 2D). This result strongly suggested that the conformational planarization of FLAP can be specifically induced prior to covalent bond scission of the stressed polymer chains. In addition, the green FL enhancement was less pronounced in a backward region of the crack (region b), in comparison with the crack tip (region c). This observation indicates spatial transmission of the relaxation process, whereas

the mechanically irreversible chromophores have a limitation to trace the relaxation after the activation (20-22).

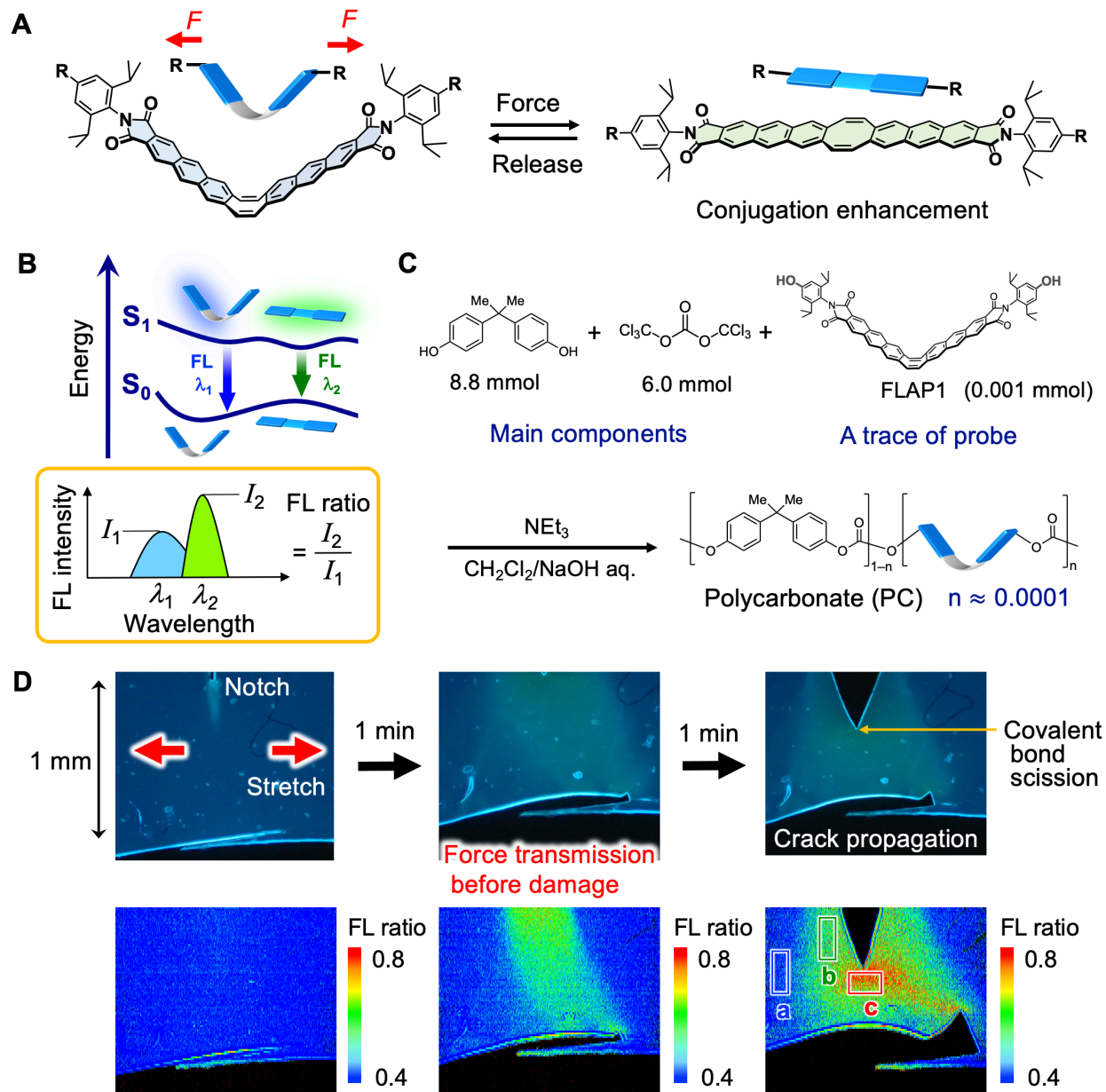


Fig. 2. (A) Flapping molecular force probe (FLAP) that enables (B) quantitative ratiometric analysis based on the dual fluorescence. (C) Preparation of polycarbonate (PC) from bisphenol A and triphosgene, chemically-doped with a trace of FLAP1 (0.05 wt%). (D) Fluorescence microscopy images of the notched PC specimen under 365-nm UV irradiation. Force transmission induced before crack propagation by tensile testing (strain rate of $2.0 \times 10^{-3} \text{ s}^{-1}$) (top). The corresponding two-dimensional ratiometric FL imaging ($\text{FL}_{525}/\text{FL}_{470}$) obtained by a hyperspectral camera (bottom). In the last image, an unstretched region (a), a backward region of the crack (b), and the crack tip (c) were indicated.

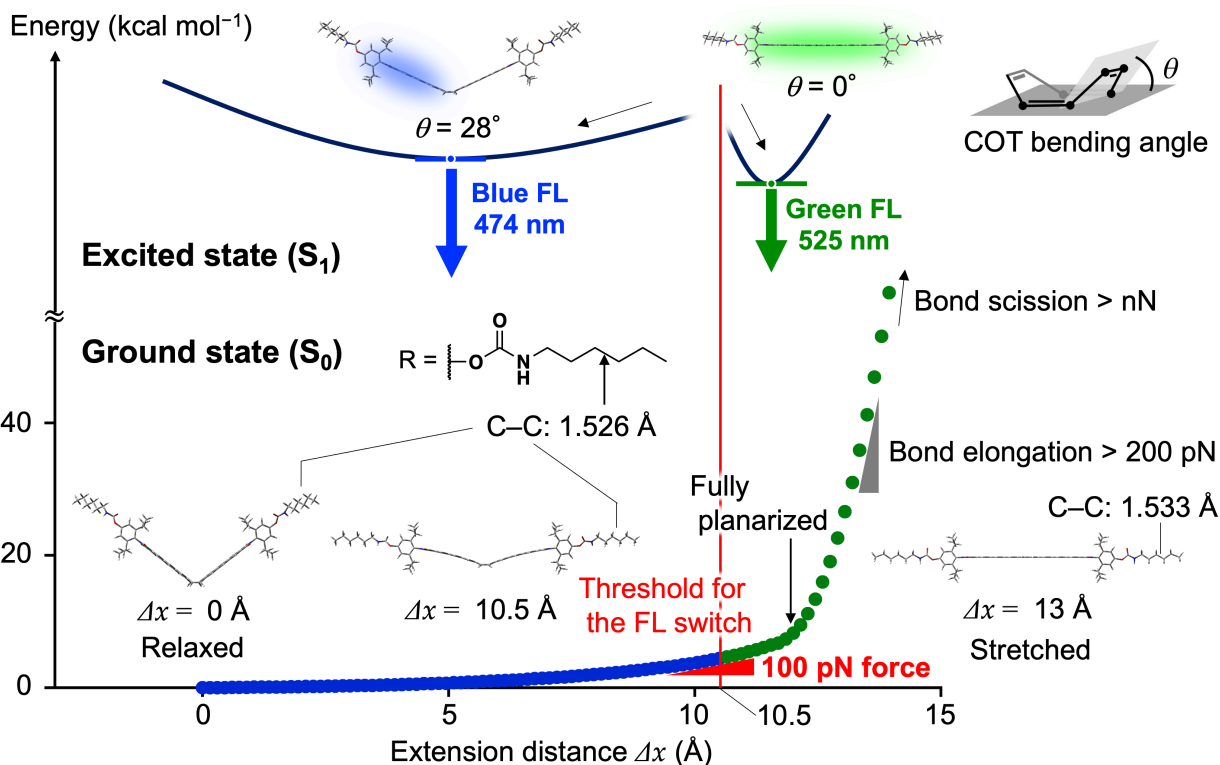


Fig. 3. DFT calculated energy profile of a polymer-chain substructure in the vicinity of FLAP ($R = N$ -hexylcarbamate in Fig 2A). Constrained geometry optimization was performed in S_0 at the PBE0/6-31G(d) level (bottom), in which the distance between terminal carbon atoms was fixed. From the most relaxed geometry, the relative potential energy was scanned as a function of extension, Δx , by 0.15 Å. Excited-state geometry optimization in S_1 at the TD-PBE0/6-31G(d) level was also performed (top) for each geometry obtained in S_0 , where the extension was fixed at the same length. The presence of two relaxed conformers of the FLAP skeleton were indicated in S_1 , whose COT bending angles were 28° (bent) and 0° (planar). Note that the conformational coordinates along the abscissa in S_1 (top) is different from that of S_0 (bottom) in this Figure.

To estimate the threshold of the FL switch at the single-molecule level, (TD-)DFT calculations were performed in S_0 and S_1 on the polymer substructure in the vicinity of FLAP (Fig. 3). Energy profile in S_0 was obtained by plotting relative potential energy of optimized geometries with a fixed distance between terminal carbon atoms. When the structure is relaxed with minimum energy, the distance is 40.4 Å (where extension = 0 Å) and the COT bending angle takes 40.2°. Scanning the extension until 15 Å indicated that, in the early stage, the planarization of FLAP occurs specifically without C-C bond elongation in the terminal carbon chains. The planarization completed by 12.0-Å extension is an energetically uphill process, but it only requires 6.7 kcal/mol. Steepness of the early-stage slope, that is the required force for the conformational planarization, is several tens of picoNewton (pN). Rapid energy increase over 200-pN slope is displayed by further extension, involving the covalent bond elongation. Note that a C-C bond length in the side chain becomes longer, only after the FLAP planarization (Fig. S14). Eventually, the side chain breaks outside the FLAP skeleton. To determine the threshold for the FL switching, the corresponding S_1 energy profile must be also considered, because small conformational relaxation

in S_1 should be expected even in the polymeric environment that suppresses a large structural change in principle. In fact, FL spectral conversion by stretching FLAP-doped PUs (see Fig. 4) only showed relative intensity change of two FL bands at 474 and 525 nm, rather than a gradual red shift. The observed unshifted FL bands indicates that population of the excited species are accumulated at two S_1 minima. Since the S_1 relaxation of FLAP proceeds in the ultrafast timescale (31), polymer chains around the force probe cannot move at this moment. Therefore, further optimizations in S_1 were conducted with the same extension at each geometry obtained in S_0 . Importantly, the S_1 optimization from half stretched structures below and above 10.5-Å extension converged into two specific conformations of the FLAP skeleton, in which the COT bending angles were 28° (bent) and 0° (planar). Accordingly, the threshold of the FL switching can be expected around the 10.5-Å extension, at which the activation energy is calculated to be 4.5 kcal/mol with the required force of 100 pN.

Controlling chemical location of the force probe in crosslinked polyurethanes

By controlling chemical location of FLAP as a force probe, we gained new quantitative insights into biased local stress concentration of crosslinked PUs. Two different polyurethanes, PU1 and PU2, were synthesized by chemical doping of FLAP1 and FLAP2, respectively (Fig. 4A). Photophysical properties of FLAP1 and FLAP2 were identical in solution. Due to the different numbers and positions of the reactive OH groups, FLAP1 is incorporated into a PU main chain, while FLAP2 into a crosslinking point. Except for the difference in the probe locations, the following parameters of these PUs are all the same: stoichiometric amounts of monomer components, polymerization conditions using a tin catalyst, and preparation methods for dumbbell-shaped test specimen. Indeed, PU1 and PU2 as well as undoped PU (PU0) reproducibly showed ignorable difference in mechanical and thermal properties (Fig. 4B and Figs. S25–27). In Fig. 4, crosslinking density, the molar fraction of triethanolamine (TEA) to the sum of the monomers, was set to be 0.10, while the molar ratio of FLAP1 and FLAP2 was small enough to be ignored, that is, 0.0001 equivalent to the poly(tetrahydrofuran) (PTHF) monomer (0.02 wt% to the obtained PUs). Stress–strain curve of the PU specimens indicated highly elastomeric properties (Fig. 4B). Typical rubbery deformations with Young’s modulus of 1.0–1.1 MPa were confirmed for these PUs. Yield point was not clearly observed for the rubbery PU. After a typical plateau-like region around 1 MPa, strain-hardening started around 500% strain, and eventually rupture occurred around 750% strain with \approx 6 MPa. It is worth noting that the rubbery PU was gradually transformed into semi-crystalline PU in several days (Figs. S39–41), as we focused the rubbery PUs in this study.

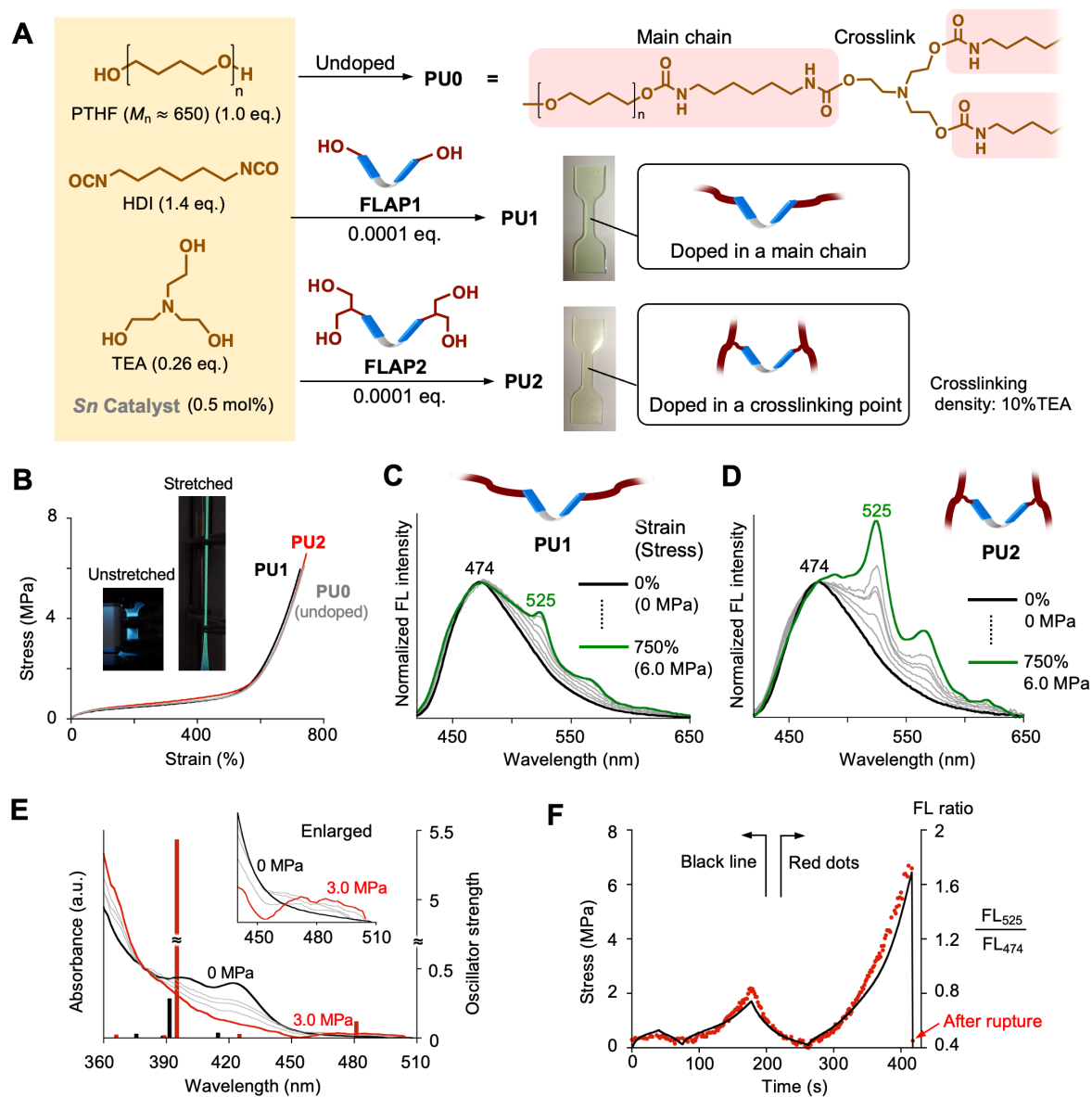


Fig. 4. (A) Controlled chemical doping of FLAP1 and FLAP2 in crosslinked polyurethanes, PU1 and PU2, respectively. PTHF: poly(tetrahydrofuran); HDI: hexamethylenediisocyanate; TEA: triethanolamine; Sn catalyst: dibutyltin dilaurate. Crosslinking density can be tuned by molar ratio of TEA to the other monomer components. (B) Stress–strain curves of rubbery polyurethanes, PU1, PU2 and undoped PU0 with the crosslinking density of 10%TEA. Inset images: the unstretched and stretched fluorescent specimens of PU2 under UV light. (C,D) FL spectral changes during the tensile testing of PU1 and PU2. FL intensity was normalized at 474 nm. Excitation wavelength: 365 nm. (E) An absorption spectral change of PU2 by stretching the specimen. Oscillator strengths were calculated at the unstretched and fully stretched geometries (Tables S12 and S13) at the TD PBE0/6-31+G(d) level. (F) Real-time and reversible FL response during the loading–unloading cycle of PU2. Time-dependent stress (black) and FL ratio plots (red).

Fluorescence spectroscopy simultaneously conducted with tensile testing

During the mechanical testing, FL spectra of the PU specimens were measured in a real-time manner (Fig. 4C and 4D). Under continuous UV irradiation (365 nm, $\approx 100 \text{ mW cm}^{-2}$), the fluorescence emission was collected by an optical fiber connected to a multi-channel photodetector. Before stretching, both PU1 and PU2 showed the same blue FL band with a single peak top at 474 nm, corresponding to the emission from the bent FLAP conformation in S_1 . As the stress increased, a green FL band at 525 nm appeared along with vibronic sub-bands at 565 and 618 nm, emitted from the planarized conformation. On the other hand, the blue FL band did not disappear in the late stage of stretching, meaning that considerable numbers of the force probes are still relaxed even just before the specimens ruptured. Namely, the macroscopic stress was not ideally distributed to the whole polymer network. The nanoscale stress concentration cannot be discussed by using “turn-on” mechanophores that show no characteristic signal in their unactivated forms. More importantly, the relative degree of the green FL enhancement was remarkably larger in PU2 than PU1, clearly indicating biased nanoscale stress concentration at the crosslinkers, compared with the PU main chains. Stretch-induced absorption spectral change was also confirmed for PU2 (Fig. 4E). Appearance of a detectable absorption band in the long-wavelength region reaching 500 nm provided the strong evidence for the compulsory conformational change of FLAP in the ground state. This weak absorption band can be assigned to a partially allowed excitation in a visible range (Table S13) for the effectively π conjugated system of the fully planarized FLAP conformation in S_0 . Loading-unloading cycle test was also carried out to confirm a repeated and real-time response of the mechanically reversible force probe (Fig. 4F and Fig. S36). The FL ratio beautifully traced time-dependent stress macroscopically loaded on the PU specimen. After the rupture, the FL ratio value went back immediately to the extent of the unstretched initial phase, which confirmed the reversible response of the FLAP force probe as well as the ignorable influence of photodegradation.

Quantifying biased nanoscale stress concentration by ratiometric fluorescence analysis

The biased stress concentration at crosslinking points was demonstrated in different crosslinking densities of 8.7%, 10% and 13%TEA (Fig. 5). Stress-strain curves of these polyurethanes are shown in Fig. 5A. The rupture stress and the rupture strain became smaller as the crosslinking density increased. Strain-hardening region of the highly crosslinked PU (13%TEA) started earlier from $\approx 400\%$ strain, while the other PUs from $\approx 500\%$ strain. The FL ratio values (FL_{525}/FL_{474}) were plotted as a function of strain and stress, respectively (Fig. 5B, C). Here we obtained an important insight. For all these PU2 specimens containing FLAP at crosslinking points, the FL ratio remarkably increased in the strain-hardening region. This behavior is in sharp contrast to the moderate increase in the PU1 specimens with FLAP at main chains. In the plateau-like region of the stress-strain curve (observed below 1-MPa stress), the FL ratios were not largely different between PU1 and PU2, indicating that the local stress concentration were observed to the same degree at main chains and crosslinkers. However, biased stress concentration at crosslinkers became pronounced in the strain-hardening process over 1-MPa stress. With decreasing the crosslinking density, the gap of the FL ratios between PU1 and PU2 at the rupture point became larger. On the other hand, when we focus on the specific strain level in a strain-hardening region (for example 600% strain), larger macroscopic stress was generated for more highly crosslinked polymers, and, accordingly, the FL ratio values for PU1 and PU2 were relatively larger at the same strain. On the basis of spectral separation analysis of the dual FL, we have estimated the corresponding percentage of the number of the stressed FLAP probes over the threshold for the FL switching (Fig. 5D and Fig S37), where the efficiencies of UV absorption and FL emission of

the bent and planar conformations were theoretically considered. With the 10%TEA crosslinking density, the estimated stressed-probe percentage at the rupture point reached up to $18.3 \pm 1.5\%$ (PU2) among the crosslinking FLAPs, whereas that in the main chains were around $8.8 \pm 0.9\%$ (PU1). Note that the low threshold (100 pN) of the FLAP force probe made the stressed-probe percentage more than 1000 times larger in comparison with reported mechanophores that require covalent bond dissociations (39), demonstrating suitability of FLAP for the polymer physics study.

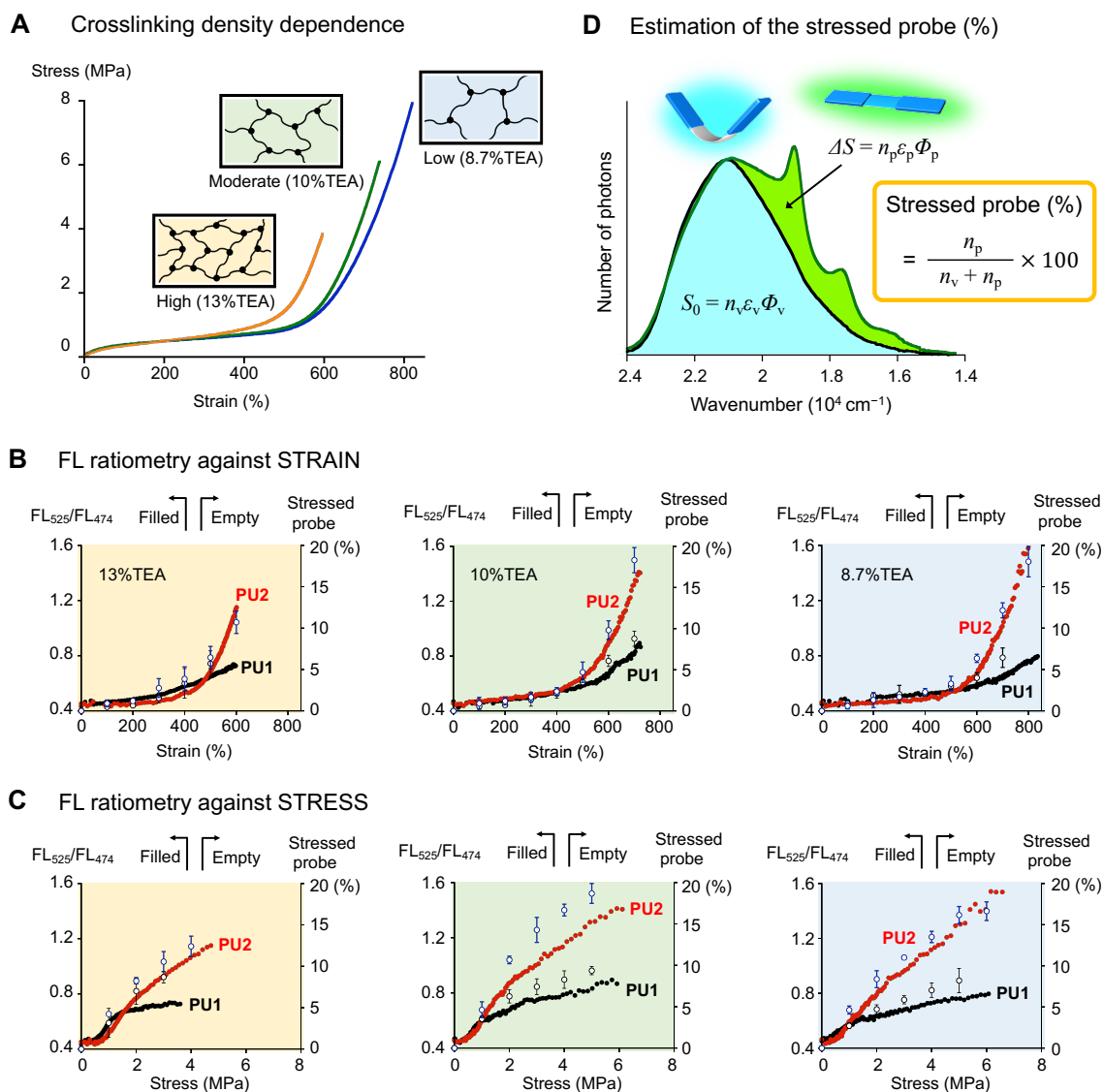


Fig. 5. (A) Stress-strain curves of undoped PU0 with different crosslinking densities. Almost same curves were obtained for PU1 and PU2 at each crosslinking density (Fig. S27). (B,C) FL ratio (filled) and percentages of the stressed FLAP probe (empty) as a function of strain (B) and stress (C) in the tensile testing. Error bars in the stressed probe (%) indicate standard deviation obtained from three tensile tests. (D) Estimation of the stressed probe (%) over the 100-pN threshold, based on the observed FL spectrum. n : number of FLAP molecules, ϵ : molar absorption coefficient at the excitation wavelength (365 nm), and Φ : FL quantum yield, where the subscripts of “v” and “p” means V-shaped (bent) and planar conformers, respectively. See the details in Fig. S37.

References and Notes:

1. Y. C. Simon, S. L. Craig, *Mechanochemistry in Materials* (Royal Society of Chemistry, UK 2017; vol 26).
2. T. Iskratsch, H. Wolfenson, M P. Sheetz, Appreciating force and shape — the rise of mechanotransduction in cell biology. *Nat. Rev. Mol. Cell Biol.* **14**, 825–833 (2014).
3. K. C. Neuman, A. Nagy, Single-molecule force spectroscopy: optical tweezers, magnetic tweezers and atomic force microscopy. *Nat. Methods.* **5**, 491–505 (2008).
4. Z. Huang, R. Boulatov, Chemomechanics with molecular force probes. *Pure Appl. Chem.* **82**, 931–951 (2010).
5. A. Freikamp, A.-L. Cost, C. Grashoff, The Piconewton Force Awakens: Quantifying Mechanics in Cells, *Trends in Cell Biol.* **26**, 838–847 (2016).
6. Y. Liu, K. Galior, V. P.-Y. Ma, K. Salaita, Molecular Tension Probes for Imaging Forces at the Cell Surface, *Acc. Chem. Res.* **50**, 2915–2924 (2017).
7. F. Meng, T. M. Suchyna, F. Sachs, A fluorescence energy transfer-based mechanical stress sensor for specific proteins in situ. *FEBS J.* **275**, 3072–3087 (2008).
8. C. Grashoff, B. D. Hoffman, M. D. Brenner, R. Zhou, M. Parsons, M. T. Yang, M. A. McLean, S. G. Sligar, C. S. Chen, T. Ha, M. A. Schwartz, Measuring mechanical tension across vinculin reveals regulation of focal adhesion dynamics. *Nature*, **466**, 263–267 (2010).
9. I. M. Klein, C. C. Husic, D. P. Kovács, N. J. Choquette, M. J. Robb, Validation of the CoGEF Method as a Predictive Tool for Polymer Mechanochemistry. *J. Am. Chem. Soc.* **142**, 16364–16381 (2020).
10. M. N. Silberstein, J. Ribas-Arino, D. Mark, Covalent Mechanochemistry: Theoretical Concepts and Computational Tools with Applications to Molecular Nanomechanics. *Chem. Rev.* **112**, 5412–5487 (2012).
11. A. L. Black, J. M. Lenhardt, S. L. Craig, From molecular mechanochemistry to stress-responsive materials. *J. Mater. Chem.* **21**, 1655–1663 (2011).
12. C. L. Brown, S. L. Craig, Molecular engineering of mechanophore activity for stress-responsive polymeric materials. *Chem. Sci.* **6**, 2158–2165 (2015).
13. D. A. Davis, A. Hamilton, J. Yang, L. D. Cremar, D. V. Gough, S. L. Potisek, M. T. Ong, P. V. Braun, T. J. Martínez, S. R. White, J. S. Moore, N. R. Sottos, Force-induced activation of covalent bonds in mechanoresponsive polymeric materials. *Nature* **459**, 68–72 (2009).
14. M. M. Caruso, D. A. Davis, Q. Shen, S. A. Odom, N. R. Sottos, S. R. White, J. S. Moore, Mechanically-Induced Chemical Changes in Polymeric Materials. *Chem. Rev.* **109**, 5755–5798 (2009).
15. Y. Chen, A. J. H. Spiering, S. Karthikeyan, G. W. M. Perers, E. W. Meijer, R. P. Sijbesma, Mechanically induced chemiluminescence from polymers incorporating a 1,2-dioxetane unit in the main chain. *Nat. Chem.* **4**, 559–562, (2012).

16. J. Li, C. Nagamani, J. S. Moore, Polymer Mechanochemistry: From Destructive to Productive. *Acc. Chem. Res.* **48**, 2181–2190 (2015).
17. Z. Chen, J. A. M. Mercer, X. Zhu, J. A. H. Romaniuk, L. Cegelski, T. J. Martinez, N. Z. Burns, Y. Xia, Mechanochemical unzipping of insulating poly(ladderene) to semiconducting polyacetylene. *Science* **357**, 475–479 (2017).
18. K. Imato, H. Otsuka, Reorganizable and stimuli-responsive polymers based on dynamic carbon-carbon linkages in diarylbibenzofuranones. *Polymer* **137**, 395–413 (2018).
19. N. Willis-Fox, E. Rognin, T. A. Aljohani, R. Daly, Polymer Mechanochemistry: Manufacturing Is Now a Force to Be Reckoned With. *Chem* **4**, 1–39, (2018).
20. A.-D. N. Celestine, N. R. Sottos, S. R. White, Strain and stress mapping by mechanochemical activation of spiropyran in poly(methyl methacrylate). *Strain* **55**, e12310 (2019).
21. E. Ducrot, Y. Chen, M. Bulters, R. P. Sijbesma, C. Creton. Toughening Elastomers with Sacrificial Bonds and Watching Them Break. *Science* **344**, 186–189 (2014).
22. J. Slootman, V. Waltz, C. J. Yeh, C. Baumann, R. Göstl, J. Comtet, C. Creton, Quantifying and mapping covalent bond scission during elastomer fracture. <https://arxiv.org/abs/2006.09468> (2020).
23. J. P. Gong, Y. Katsuyama, T. Kurokawa, Y. Osada, Double-Network Hydrogels with Extremely High Mechanical Strength. *Adv. Mater.* **15**, 1155–1158 (2003).
24. Y. Okumura, K. Ito, The Polyrotaxane Gel: A Topological Gel by Figure-of-Eight Cross-links. *Adv. Mater.* **13**, 485–487 (2001).
25. J.-Y. Sun, X. Zhao, W. R. K. Illeperuma, O. Chaudhuri, K. H. Oh, D. J. Mooney, J. J. Vlassak, Z. Suo, Highly stretchable and tough hydrogels. *Nature* **489**, 133–136 (2012).
26. E. Filippidi, T. R. Cristiani, C. D. Eisenbach, J. H. Waite, J. N. Israelachvili, B. K. Ahn, M. T. Valentine, Toughening elastomers using mussel-inspired iron-catechol complexes. *Science* **358**, 502–505 (2017).
27. T. Matsuda, R. Kawakami, R. Namba, T. Nakajima, T., J. P. Gong, Mechanoresponsive self-growing hydrogels inspired by muscle training. *Science* **363**, 504–508 (2019).
28. M. K. Beyer, H. Clausen-Schaumann, Mechanochemistry: The Mechanical Activation of Covalent Bonds. *Chem. Rev.* **105**, 2921–2948, (2005).
29. C. Yuan, S. Saito, C. Camacho, S. Irle, I. Hisaki, S. Yamaguchi, A π -conjugated System with Flexibility and Rigidity That Shows Environment-Dependent RGB Luminescence. *J. Am. Chem. Soc.* **135**, 8842–8845 (2013).
30. C. S. Wannere, D. Moran, N. L. Allinger, B. A. Hess, Jr., L. J. Schaad, P. v. R. Schleyer, On the Stability of Large $[4n]$ Annulenes. *Org. Lett.* **5**, 2983–2986 (2003).
31. R. Kotani, H. Sotome, H. Okajima, S. Yokoyama, Y. Nakaike, A. Kashiwagi, C. Mori, Y. Nakada, S. Yamaguchi, A. Osuka, A. Sakamoto, H. Miyasaka, S. Saito, Flapping viscosity probe that shows polarity-independent ratiometric fluorescence. *J. Mater. Chem. C.* **5**, 5248–5256 (2017).

32. T. Yamakado, K. Otsubo, A. Osuka, S. Saito, Compression of a Flapping Mechanophore Accompanied by Thermal Void Collapse in a Crystalline Phase. *J. Am. Chem. Soc.* **140**, 6245–6248 (2018).
33. G. A. Filonenko, J. R. Khusnutdinova, Dynamic Phosphorescent Probe for Facile and Reversible Stress Sensing. *Adv. Mater.* 1700563 (2017).
34. Y. Sagara, M. Karman, E. Verde-Sesto, K. Matsuo, Y. Kim, N. Tamaoki, C. Weder, Rotaxanes as Mechanochromic Fluorescent Force Transducers in Polymers. *J. Am. Chem. Soc.* **140**, 1584–1587 (2018).
35. K. Straková, J. López-Andarias, N. Jiménez-Rojo, J. E. Chamber, S. J. Marciniak, H. Riezman, N. Sakai, S. Matile, HaloFlippers: A General Tool for the Fluorescence Imaging of Precisely Localized Membrane Tension Changes in Living Cells. *ACS Central Science* **6**, 1376-1385 (2020).
36. M. H. Lee, J. S. Kim, J. L. Sessler, Small molecule-based ratiometric fluorescence probes for cations, anions, and biomolecules. *Chem. Soc. Rev.* **44**, 4185–4191 (2015).
37. J. Gierschner, S. K. Behera, S. Y. Park, Dual Emission: Classes, Mechanism and Conditions. *Angew. Chem. Int. Ed. in press* DOI: 10.1002/anie.202009789 (2020).
38. C. Yuan, S. Saito, C. Camacho, T. Kowalczyk, S. Irle, S. Yamaguchi, Hybridization of a Flexible Cyclooctatetraene Core and Rigid Aceneimide Wings for Multiluminescent Flapping π Systems. *Chem. Eur. J.* **20**, 2193–2200 (2014).
39. K. Imato, T. Kanehara, T. Ohishi, M. Nishihara, H. Yajima, M. Ito, A. Takahara, H. Otsuka, Mechanochromic Dynamic Covalent Elastomers: Quantitative Stress Evaluation and Autonomous Recovery. *ACS Macro Lett.* **4**, 1307–1311 (2015).

Acknowledgments: We thank Dr Hiroya Abe and Dr Yuta Saito (Tohoku Univ.) for their help in the early stage of the preliminary study; **Funding:** JST, PRESTO, FRONTIER, Grant number JPMJPR16P6; MEXT/JSPS, KAKENHI, Grant Numbers JP18H01952, 20H04625, 19KK0357, 18H05482, and JP18J22477; Inoue foundation for science; **Author contributions:** H.Y. and S.S. conceived the concept. R.K., H.Y., and S.S. designed the experiments. R.K., S.Y., and S.N. performed the experiments. R.K. and S.S. conducted the quantum calculations. R.K. and S.S. analyzed the data. R.K. and S.S. wrote the manuscript, and S.Y., A.O., and H.Y. proofread it; **Competing interests:** Authors declare no competing interests; and **Data and materials availability:** All data is available in the main text or the supplementary materials.

Supplementary Materials:

Materials and Methods

Figures S1-S68

Tables S1-S24

Supplementary materials

Synthesis and purification

All reagents and solvents were of commercial grade and were used without further purification unless where noted. Tetrahydrofuran (THF) was dried using Glass Contour solvent purification system. Superdehydrated dimethylformamide (DMF) was purchased from Wako Chemicals. Polytetrahydrofutan ($M_n \sim 650$) was dried under vacuum at 70 °C for 2 h before use. Thin layer chromatography (TLC) was performed by silica gel 60 F₂₅₄ (Merck). Column chromatography was performed using Wako gel C-300.

Measurements

¹H and ¹³C NMR spectra were recorded on a JEOL ECA-600 (600 MHz for ¹H and 151 MHz for ¹³C NMR) spectrometer for **FLAP1**, **FLAP2**, compounds **4–11**, and compounds **S1–S4**. Chemical shifts were expressed as the δ scale in ppm relative to internal standards CHCl₃ ($\delta = 7.26$ ppm for ¹H and $\delta = 77.16$ ppm for ¹³C) and DMSO ($\delta = 2.50$ ppm for ¹H and $\delta = 39.52$ ppm for ¹³C). High-resolution atmospheric-pressure-chemical-ionization time-of-flight mass-spectrometry (HR-APCI-TOF-MS) was recorded on a BRUKER micrOTOF model using positive mode. UV-visible absorption spectra were recorded on Shimadzu UV-3600 spectrometers. Fluorescence (FL) spectra were recorded on a JASCO Spectrofluorometer FP-8500. Absolute FL quantum yields were determined on a HAMAMATSU C9920-02S. FL lifetime was recorded on Hamamatsu Photonics Quantaaurus-Tau C11367. Tensile tests were carried out using a SHIMADZU AUTOGRAPH AGS-X with a 1-kN load cell at crosshead. Differential scanning calorimetry (DSC) was recorded on a Hitachi High-Tech TA7000. Rheological measurements were conducted on an Anton Paar MCR702. Real-time FL measurements of PU specimens were performed using an Otsuka Electronics MULTI CHANNEL PHOTO DETECTOR MCPD-68000. Cross-Nicol images and scales under microscope were obtained by a Leica DM2500 P optical microscope equipped with a Linkam LTS420E temperature-controlled microscope stage. Photographs and movies of specimens were taken using an OLYMPUS digital camera Tough TG-6.

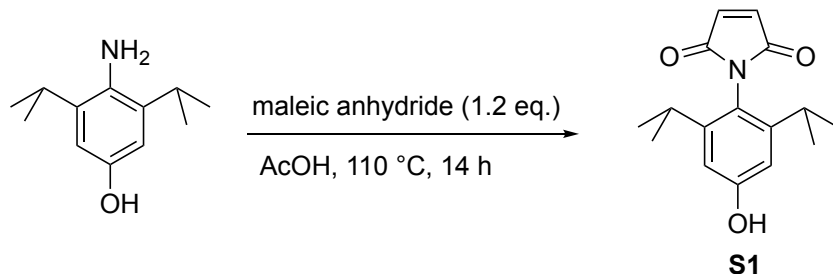
Fluorescence microscopy imaging of the stretched polycarbonate film

This experiment was conducted by combination use of a microscope (OLYMPUS inverted research microscope IX83 equipped with a mercury lump U-HGLGPS), a tensile testing machine (AcroEdge tensile testing machine OZ911) and a hyperspectral camera (EBAJAPAN hyperspectral camera NH-8). A strip **PC1** specimen (width ≈ 1 mm and thickness ≈ 0.03 mm), bearing a small notch was used for the tensile testing. This specimen was held with an initial distance of 25 mm, and extended from both sides at the speed of 0.05 mm s⁻¹. Since the stretching is performed symmetrically, the focused notch stays within the field of view of the microscope. At the same time, FL spectrum at each pixel was collected on the hyperspectral camera. The data was acquired by an exposure time of 500 ms at a wavelength interval of 5 nm. The FL optical micrograph (Fig. 2D, top) was taken by a digital camera (OLYMPUS TG-6), while the FL ratio mapping (Fig. 2D, bottom) was obtained by an analytical software (EBAJAPAN HSAAnalyzer) of the collected FL spectra.

Theoretical study

Theoretical calculations were performed using the Gaussian 16 program (see below). (40)

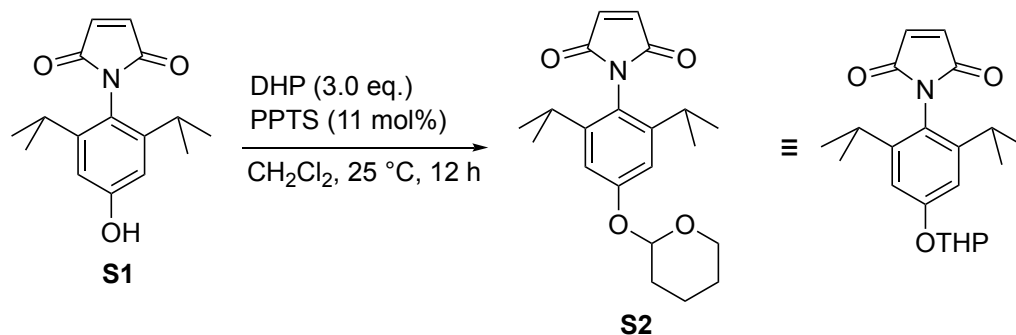
Synthesis of new compounds



N-(4-Hydroxy-2,6-diisopropylphenyl)maleimide (**S1**)

Under Ar atmosphere, 4-amino-3,5-diisopropylphenol (**41**) (2.77 g, 14.3 mmol) and maleic anhydride (1.68 g, 17.2 mmol) were added to a round-bottom flask (500 mL). After addition of AcOH (70 mL), the reaction mixture was stirred at 110 °C for 14 h. The resulting mixture diluted with EtOAc was poured into a separatory funnel, washed with saturated aqueous NaHCO₃ (3 times) and brine, dried over anhydrous Na₂SO₄ and evaporated. The crude product was purified by silica gel column chromatography (eluent: CH₂Cl₂/EtOAc = 20/1 by volume). Recrystallization from *n*-hexane furnished **S1** as a white solid (3.08 g, 79%).

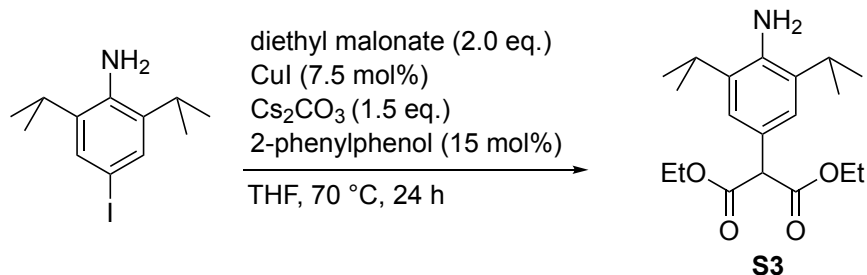
¹H NMR (600 MHz, CDCl₃) δ (ppm) 6.87 (s, 2H), 6.69 (s, 2H), 4.80 (s, 1H), 2.56 (sept, *J* = 6.9 Hz, 2H) and 1.13 (d, *J* = 6.9 Hz, 12H); ¹³C NMR (151 MHz, CDCl₃) δ (ppm) 170.99, 157.10, 149.54, 134.43, 118.95, 111.26, 29.50 and 23.95; HR-APCI TOF-MS (*m/z*) found 273.1358, calcd for C₁₆H₁₉NO₃: 273.1365 [*M*]⁺.



N-(2,6-Diisopropyl-4-((tetrahydro-2*H*-pyran-2-yl)oxy)phenyl)maleimide (**S2**)

Under Ar atmosphere, **S1** (3.08 g, 11.3 mmol) and pyridinium *p*-toluenesulfonate (PPTS, 310 mg, 1.23 mmol) were added to a round-bottom flask (300 mL). After addition of CH₂Cl₂ (85 mL) and 3,4-dihydro-2*H*-pyran (DHP, 2.87 mL, 33.4 mmol) at 0 °C, the reaction mixture was stirred at 25 °C for 12 h. The reaction mixture was quenched with H₂O and poured into a separatory funnel, then washed with brine, dried over anhydrous Na₂SO₄ and evaporated. Recrystallization from CH₂Cl₂/*n*-hexane furnished **S2** as a white solid (3.86 g, 96%).

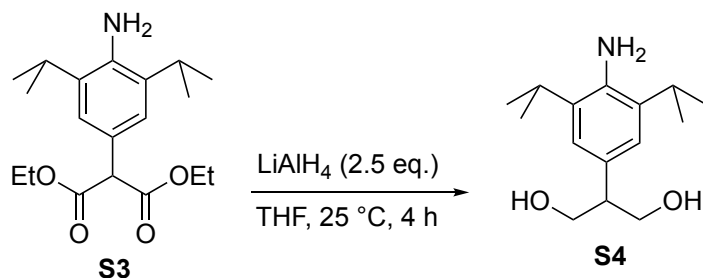
¹H NMR (600 MHz, CDCl₃) δ (ppm) 6.92 (s, 2H), 6.86 (s, 2H), 5.45 (m, 1H), 3.92 (m, 1H), 3.63 (m, 1H), 2.57 (sept, *J* = 6.9 Hz, 2H), 2.02 (m, 1H), 1.87 (m, 2H), 1.67–1.69 (m, 2H), 1.62–1.63 (m, 1H) and 1.13 (d, *J* = 6.9 Hz, 12H); ¹³C NMR (151 MHz, CDCl₃) δ (ppm) 170.94, 158.76, 148.89, 134.36, 119.52, 112.33, 96.34, 61.94, 30.49, 29.55, 25.36, 23.95 and 18.71; HR-APCI TOF-MS (*m/z*) found 357.1946, calcd for C₂₁H₂₇NO₄: 357.1946 [*M*]⁻.



Diethyl 2-(4-amino-3,5-diisopropylphenyl)malonate (**S3**)

Under Ar atmosphere, 4-iodo-2,6-diisopropylaniline (**42**) (6.06 g, 20.0 mmol), CuI (285 mg, 1.50 mmol), Cs₂CO₃ (9.78 g, 30.0 mmol) and 2-phenylphenol (510 mg, 3.00 mmol) were added to a round-bottom flask (100 mL). After addition of THF (20 mL) and diethyl malonate (6.10 mL, 40.0 mmol), the reaction mixture was stirred at 70 °C for 24 h. The reaction mixture was quenched with H₂O and diluted with EtOAc. The resulting mixture was poured into a separatory funnel, washed with brine, dried over anhydrous Na₂SO₄ and evaporated. The crude product was purified by silica gel column chromatography (eluent: CH₂Cl₂) and **S3** was obtained as a brown oil (4.00 g, 59%).

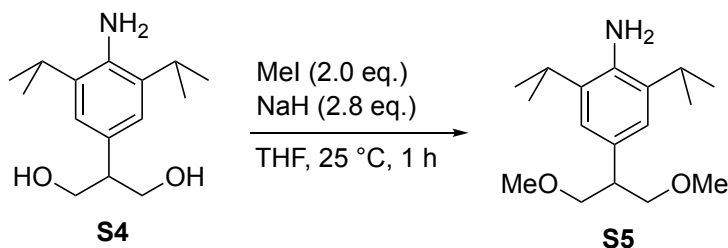
¹H NMR (600 MHz, CDCl₃) δ (ppm) 7.04 (s, 2H), 4.50 (s, 1H), 4.25–4.16 (m, 4H), 3.75 (s, 2H), 2.90 (sept, *J* = 6.9 Hz, 2H) and 1.28–1.25 (m, 18H); ¹³C NMR (151 MHz, CDCl₃) δ (ppm) 168.96, 140.43, 132.45, 124.04, 122.55, 61.61, 58.06, 28.16, 22.50 and 14.21; HR-APCI TOF-MS (*m/z*) found 336.2183, calcd for C₁₉H₃₀NO₄: 336.2169 [*M*+H]⁺.



2-(4-Amino-3,5-diisopropylphenyl)propane-1,3-diol (**S4**)

Under Ar atmosphere, to the suspension of LiAlH₄ (396 mg, 10.4 mmol) in THF (10 mL), a THF (10 mL) solution of **S3** (1.52 g, 4.18 mmol) was added at 0 °C. The mixture was stirred at 25 °C for 4 h. The reaction mixture was quenched with saturated aqueous Na₂SO₄, filtered to remove aluminum salts, and washed with EtOAc (50 mL). The filtrate was purified by silica gel column chromatography (eluent: EtOAc). Recrystallization from CH₂Cl₂/*n*-hexane furnished **S4** as a white solid (910 mg, 87%).

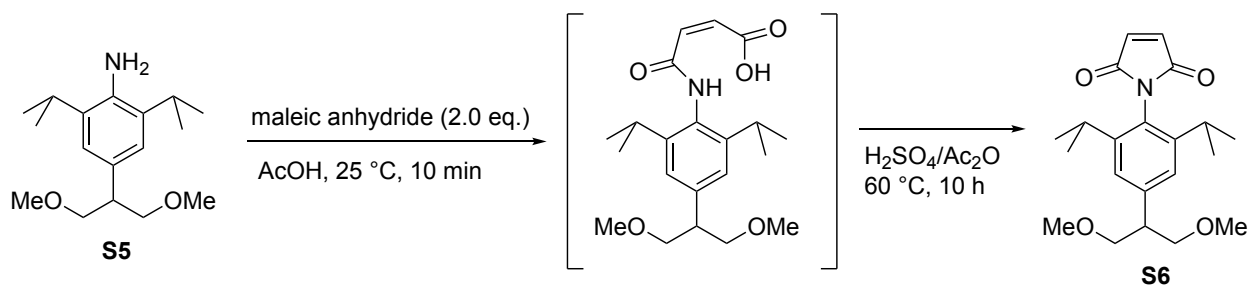
¹H NMR (600 MHz, CDCl₃) δ (ppm) 6.87 (s, 2H), 3.98–3.94 (m, 2H), 3.91–3.88 (m, 2H), 3.70 (s, 2H), 3.03 (tt, *J* = 7.8, 5.4 Hz, 1H), 2.92 (sept, *J* = 6.6 Hz, 2H), 1.92 (t, *J* = 5.4 Hz, 2H) and 1.26 (d, *J* = 6.6 Hz, 12H); ¹³C NMR (151 MHz, CDCl₃) δ (ppm) 139.44, 132.97, 128.69, 122.43, 66.55, 49.75, 28.09 and 22.52; HR-APCI TOF-MS (*m/z*) found 252.1968, calcd for C₁₅H₂₆NO₂: 252.1958 [*M*+H]⁺.



4-(1,3-Dimethoxypropan-2-yl)-2,6-diisopropylaniline (**S5**)

Under Ar atmosphere, to the suspension of NaH (60% dispersion in paraffin liquid, 401 mg, 10.0 mmol) and MeI (445 μL , 7.16 mmol) in THF (9.0 mL), a THF (4.5 mL) solution of **S4** (900 mg, 3.58 mmol) was added at 0 $^\circ\text{C}$. The mixture was stirred at 25 $^\circ\text{C}$ for 1 h. The reaction mixture was diluted with EtOAc (20 mL) and evaporated. The crude product was purified by silica gel column chromatography (eluent: CH_2Cl_2 :*n*-hexane:EtO₂ = 1:1:1 by volume) to furnish **S5** as brown oil (932 mg, 93%).

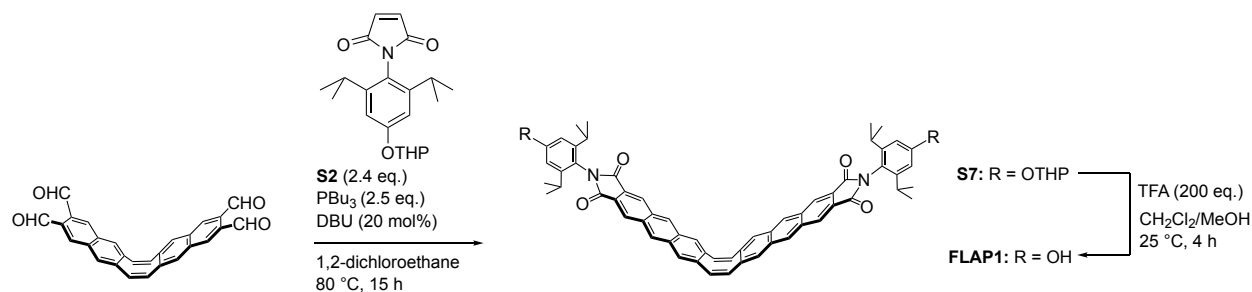
¹H NMR (600 MHz, CDCl_3) δ (ppm) 6.92 (s, 2H), 3.63 (dd, J = 9.2, 6.8 Hz, 2H), 3.57 (dd, J = 9.7, 6.4 Hz, 2H), 3.39 (s, 6H), 3.06 (tt, J = 9.2, 6.4 Hz, 1H), 2.91 (sept, J = 6.9 Hz, 2H), and 1.27 (d, J = 6.9 Hz, 12H); ¹³C NMR (151 MHz, CDCl_3) δ (ppm) 139.12, 132.45, 130.54, 122.43, 74.79, 58.99, 45.84, 28.13 and 22.56; HR-APCI TOF-MS (m/z) found 280.2271, calcd for $\text{C}_{17}\text{H}_{30}\text{NO}_2$: 280.2271 [$M+\text{H}$]⁺.



N-(4-(1,3-Dimethoxypropan-2-yl)-2,6-diisopropylphenyl)maleimide (**S6**)

Under Ar atmosphere, **S5** (1.03 g, 3.69 mmol) and maleic anhydride (723 mg, 7.37 mmol) were added to a Schlenk flask (20 mL). After addition of AcOH (2.21 mL), the reaction mixture was stirred at 25 $^\circ\text{C}$ for 10 min. Then, H_2SO_4 (95%, 369 μL) and acetic anhydride (184 μL) were added to the reaction mixture, and the reaction vessel was warmed at 60 $^\circ\text{C}$ for 10 h. The reaction mixture was quenched with H_2O and diluted with EtOAc. The solution was poured into a separatory funnel, washed with brine, dried over anhydrous Na_2SO_4 and evaporated. The crude product was purified by silica gel column chromatography (eluent: CH_2Cl_2 /Et₂O = 6/1 by volume) and **S6** was obtained as a white solid (1.06 g, 80%).

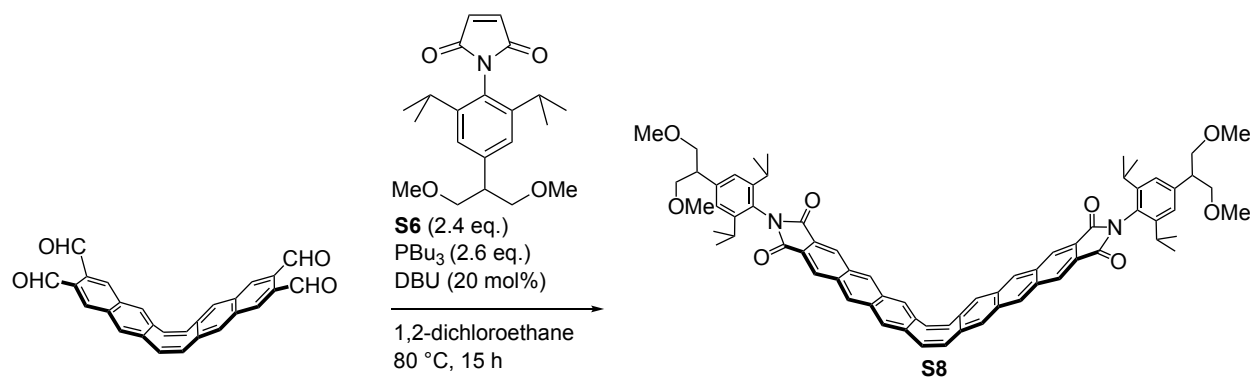
¹H NMR (600 MHz, CDCl_3) δ (ppm) 7.12 (s, 2H), 6.88 (s, 2H), 3.67–3.64 (m, 2H), 3.63–3.60 (m, 2H), 3.35 (s, 6H), 3.13 (tt, J = 7.2, 6.0 Hz, 1H), 2.59 (sept, J = 6.9 Hz, 2H) and 1.15 (d, J = 6.9 Hz, 12H); ¹³C NMR (151 MHz, CDCl_3) δ (ppm) 170.84, 147.24, 142.95, 134.43, 124.79, 123.94, 74.04, 59.09, 46.37, 29.45, and 24.09; HR-APCI TOF-MS (m/z) found 359.2096, calcd for $\text{C}_{21}\text{H}_{30}\text{NO}_4$: 359.2091 [M]⁺.



FLAP1

Under Ar atmosphere, **S2** (559 mg, 1.56 mmol) and 1,2-dichloroethane (12 mL) were added to a round-bottom flask (20 mL). After addition of tributylphosphine (410 μL , 1.66 mmol) at $0\text{ }^\circ\text{C}$, the reaction mixture was stirred at $25\text{ }^\circ\text{C}$ for 30 min. A 1,2-dichloroethane (10 mL) solution of tetraformyl dinaphthocyclooctatetraene (**29,31**) (271 mg, 0.651 mmol) was added to the reaction mixture at $0\text{ }^\circ\text{C}$, followed by addition of DBU (19.5 μL , 0.130 mmol). The reaction mixture was stirred at $80\text{ }^\circ\text{C}$ for 15 h, and then quenched with H_2O . The resulting mixture was poured into a separatory funnel, washed with brine, dried over anhydrous Na_2SO_4 and evaporated. The crude product was purified by silica gel column chromatography (eluent: $\text{CH}_2\text{Cl}_2/\text{AcOEt} = 20/1$ by volume), and **S7** was obtained as a yellow solid (138 mg, 20% from tetraformyl dinaphthocyclooctatetraene), which was used for the subsequent reaction. **S7** was added to a round-bottom flask (100 mL). After addition of CH_2Cl_2 (30 mL), MeOH (10 mL), and TFA (2.0 mL, 26 mmol), the reaction mixture was stirred at $25\text{ }^\circ\text{C}$ for 4 h. The reaction mixture was quenched with H_2O and poured into a separatory funnel, then washed with brine, dried over anhydrous Na_2SO_4 and evaporated. The crude product was purified by silica gel column chromatography (eluent: $\text{CH}_2\text{Cl}_2/\text{EtOAc} = 20/1$ by volume). Recrystallization from $\text{CH}_2\text{Cl}_2/n$ -hexane furnished **FLAP1** as a yellow solid (107 mg, 92% from **S7**).

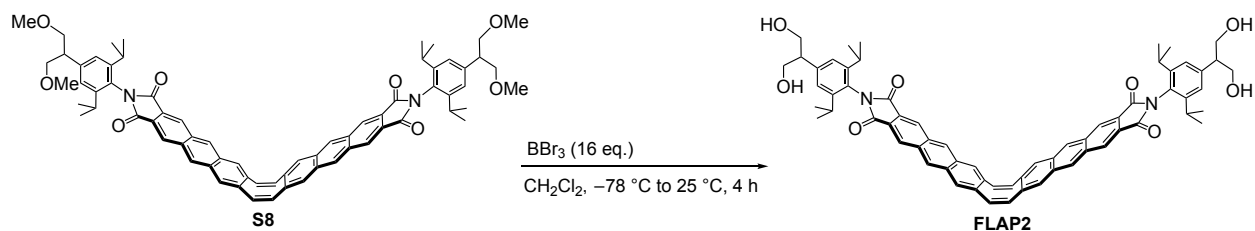
^1H NMR (600 MHz, CDCl_3) δ (ppm) 8.55 (m, 4H + 4H), 7.94 (s, 4H), 7.24 (s, 4H), 6.75 (s, 4H), 4.90 (s, 2H), 2.70 (sept, $J = 6.9\text{ Hz}$, 4H) and 1.14 (d, $J = 6.9\text{ Hz}$, 24H); ^{13}C NMR (151 MHz, $\text{DMSO}-d_6$) δ (ppm) 167.47, 158.59, 147.92, 136.12, 133.09, 131.88, 131.44, 129.93, 128.34, 126.56, 125.73, 118.40, 110.50, 28.65 and 23.56; HR-MALDI TOF-MS (m/z) found 895.33, calcd for $\text{C}_{60}\text{H}_{51}\text{N}_2\text{O}_6$: 895.37 [$M+\text{H}$] $^+$. UV/visible absorption (CH_2Cl_2): λ_{max} ($\epsilon/\text{M}^{-1}\text{ cm}^{-1}$) = 332 nm (9.28×10^4); fluorescence (CH_2Cl_2 , $\lambda_{\text{ex}} = 340\text{ nm}$): $\lambda_{\text{max}} = 523, 564, \text{ and } 610\text{ nm}$, $\Phi_{\text{FL}} = 0.26$.



S8

Under Ar atmosphere, **S6** (682 mg, 1.90 mmol) and 1,2-dichloroethane (30 mL) were added to a round-bottom flask (200 mL). After addition of tributylphosphine (507 μ L, 2.05 mmol) at 0 °C, the reaction mixture was stirred at 25 °C for 30 min. Then, a 1,2-dichloroethane (15 mL) solution of tetraformyl dinaphthocyclooctatetraene (329 mg, 0.79 mmol) was added to the reaction mixture at 0 °C, followed by addition of DBU (24 μ L, 0.16 mmol). The reaction mixture was stirred at 80 °C for 12 h, and then quenched with H₂O. The resulting mixture was poured into a separatory funnel, washed with brine, dried over anhydrous Na₂SO₄ and evaporated. The crude product was purified by silica gel column chromatography (eluent: CH₂Cl₂/Et₂O = 5:1 by volume) and **S8** was obtained as a yellow solid (208 mg, 25% from tetraformyl dinaphthocyclooctatetraene).

¹H NMR (600 MHz, CDCl₃) δ (ppm) 8.55 (s, 4H + 4H), 7.94 (s, 4H), 7.24 (s, 4H), 7.17 (s, 4H), 3.69–3.62 (m, 8H), 3.37 (s, 12H), 3.16 (tt, J =7.2, 6.0 Hz, 2H), 2.72 (sept, J =6.8 Hz, 4H) and 1.15 (d, J =6.8 Hz, 24H); ¹³C NMR (151 MHz, CDCl₃) δ (ppm) 167.88, 146.68, 142.80, 136.63, 133.36, 132.39, 132.20, 129.84, 128.49, 126.64, 125.92, 123.88, 123.56, 74.16, 59.07, 46.37, 29.48, and 24.12; HR-MALDI TOF-MS (m/z) found 1089.53, calcd for C₇₀H₇₀N₂O₈Na: 1089.50 [M +Na]⁺.



FLAP2

Under Ar atmosphere, **S8** (9.8 mg, 9.2 μmol) and CH_2Cl_2 (0.7 mL) were added to a Schlenk flask (20 mL). After addition of a CH_2Cl_2 solution of BBr_3 (1.0 M, 147 μL) at $-78\text{ }^\circ\text{C}$, the reaction mixture was stirred and warmed to $25\text{ }^\circ\text{C}$ over 4 h. The reaction mixture was quenched with H_2O and poured into a separatory funnel, then washed with brine, dried over anhydrous Na_2SO_4 and evaporated. The crude product was purified by silica gel column chromatography (eluent: EtOAc) and **FLAP2** was obtained as a yellow solid (6.7 mg, 72%).

^1H NMR (600 MHz, CDCl_3) δ (ppm) 8.56 (s, 4H), 8.55 (s, 4H), 7.94 (s, 4H), 7.24 (s, 4H), 7.14 (s, 4H), 4.05–4.00 (m, 8H), 3.18–3.14 (m, 2H), 2.74 (sept, $J = 6.8$ Hz, 4H), 2.01 (t, $J = 6.0$ Hz, 4H) and 1.16 (d, $J = 6.8$ Hz, 24H); ^{13}C NMR (151 MHz, $\text{DMSO}-d_6$) δ (ppm) 167.30, 145.81, 143.99, 136.18, 133.13, 131.89, 131.47, 129.99, 128.37, 126.76, 125.69, 125.42, 123.63, 62.64, 50.82, 28.70, and 23.67; HR-MALDI TOF-MS (m/z) found 1033.42, calcd for $\text{C}_{66}\text{H}_{62}\text{N}_2\text{O}_8\text{Na}$: 1033.44 $[M+\text{Na}]^+$. UV/visible absorption (CH_2Cl_2): λ_{max} ($\epsilon / \text{M}^{-1} \text{cm}^{-1}$) = 331 nm (9.37×10^4); fluorescence (CH_2Cl_2 , $\lambda_{\text{ex}} = 340$ nm): $\lambda_{\text{max}} = 524, 565,$ and 610 nm, $\Phi_{\text{FL}} = 0.32$.

Photophysical properties of parent FLAP molecules

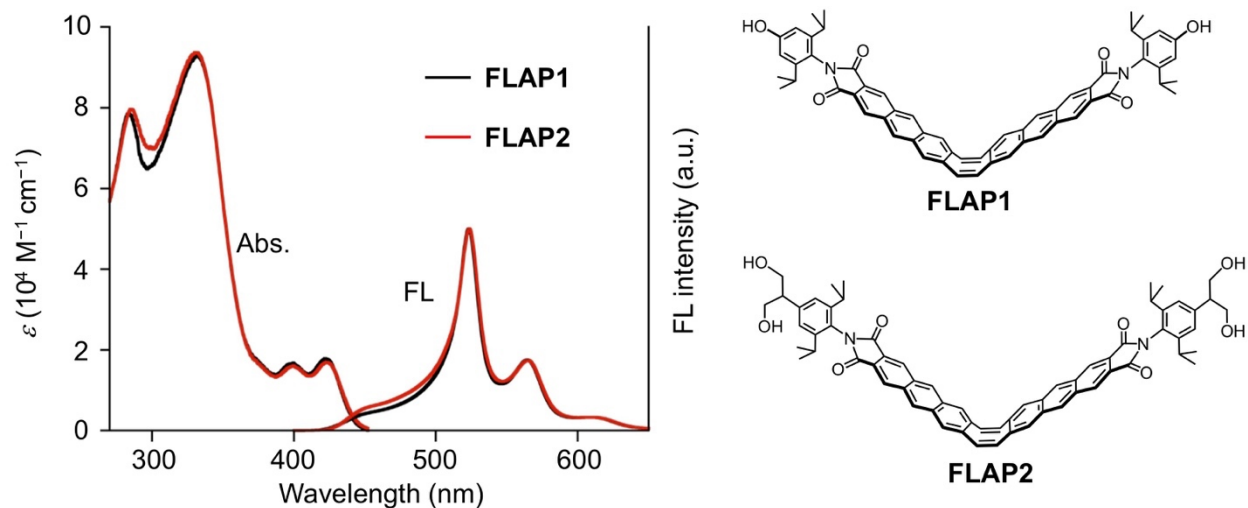


Fig. S1. UV/visible absorption (Abs) and FL spectra of **FLAP1** and **FLAP2** in CH_2Cl_2 .

Table S1. Photophysical constants of **FLAP1** and **FLAP2** in CH_2Cl_2 . $\lambda_{\text{ex}} = 365 \text{ nm}$.

	Φ_{FL}	$\tau_{\text{FL}} \text{ (ns)}^{\text{a}}$	$k_{\text{r}} \text{ (s}^{-1}\text{)}^{\text{b}}$	$k_{\text{nr}} \text{ (s}^{-1}\text{)}^{\text{c}}$
FLAP1	0.26	11.0	2.4×10^7	6.7×10^7
FLAP2	0.32	10.6	3.0×10^7	6.4×10^7

^a FL lifetime monitored at 525 nm. ^b Radiative decay constant. ^c Nonradiative decay constant. k_{r} and k_{nr} were estimated from the equations below.

$$\Phi_{\text{FL}} = k_{\text{r}} / (k_{\text{r}} + k_{\text{nr}})$$

$$\tau_{\text{FL}} = 1 / (k_{\text{r}} + k_{\text{nr}})$$

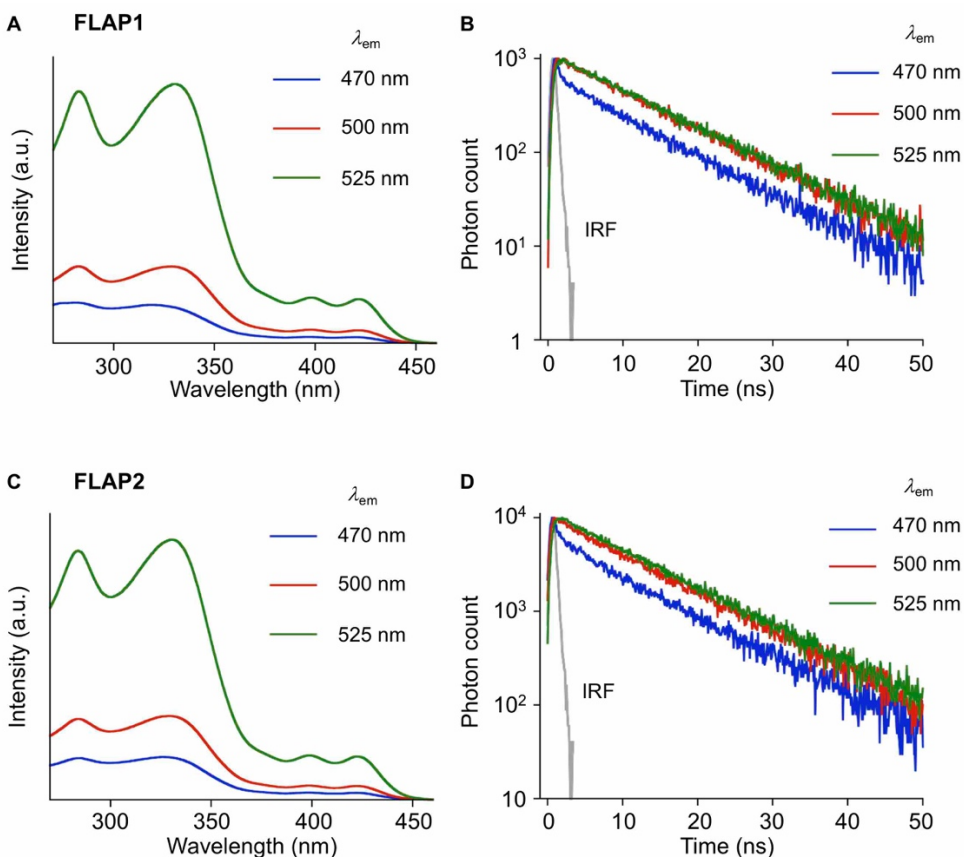


Fig. S2. (A) Excitation spectra and (B) FL decay profiles of **FLAP1** in CH_2Cl_2 , monitored at different emission wavelengths, and (C, D) those of **FLAP2**. Concentration: *ca.* 10^{-6} M. IRF: The instrument response function.

Table S2. Photophysical constants of **FLAP1** and **FLAP2** in CH_2Cl_2 . $\lambda_{\text{ex}} = 365$ nm.

	λ_{em} (nm)	χ^2	τ_{FL} (ns) ^a	τ_1 (ns)	τ_2 (ns)	A_1	A_2
FLAP1	470	1.06	9.0	0.2	9.9	320	66
	500	1.16	10.6	0.3	10.8	88	110
	525	1.03	11.0				
FLAP2	470	1.25	8.9	0.2	9.8	270	66
	500	1.07	10.4	0.3	10.7	94	104
	525	1.05	10.6				

^a Mean FL lifetime calculated from the equation below.

$$\tau_{\text{FL}} = \frac{\tau_1^2 A_1 + \tau_2^2 A_2}{\tau_1 A_1 + \tau_2 A_2}$$

where A_1 and A_2 was determined by analysis of the fitting equation below.

$$G(t) = A_1 \exp\left(-\frac{t}{\tau_1}\right) + A_2 \exp\left(-\frac{t}{\tau_2}\right)$$

where $G(t)$ was photon count as a function of time.

Computational studies of FLAP molecules

Density functional theory (DFT) and time-dependent (TD) DFT calculations of the isolated molecules were performed using the Gaussian 16 program. The appropriate density functional (PBE0) was selected because of reproducibility of the absorption spectrum of the FLAP series (32). All the optimized structures gave no imaginary frequency, bearing C_1 symmetry. In the Figs. S4–12, compositions (%) and oscillator strength f were calculated based on the respective optimized structure. H and L stand for HOMO and LUMO, respectively. Here and elsewhere, compositions were calculated by taking the square of the dominant configuration and multiplying the result by two, in order to account for excitations involving α and β spin orbitals. In the optimization calculation in S_1 , two energy minima at bent and planar geometries were found (Figs. S5 and S6). Here the oscillator strength of the S_1 bent geometry was calculated by the PBE0 functional to be zero (Table S4), although a non-zero oscillator strength was obtained by a different functional, CAM-B3LYP (Fig. S11 and Table S10). This indicates that the calculation results of the S_1 electronic state are sensitive to the applied calculation level.

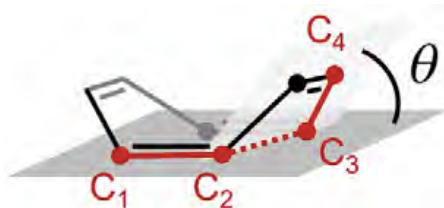


Fig. S3. Definition of the COT bending angle θ used in the computational studies. The angle θ was defined as a dihedral angle between the two planes, the C_1 – C_2 – C_3 plane and the C_2 – C_3 – C_4 plane.

Calculations performed at the PBE0/6-31+G(d) level of theory

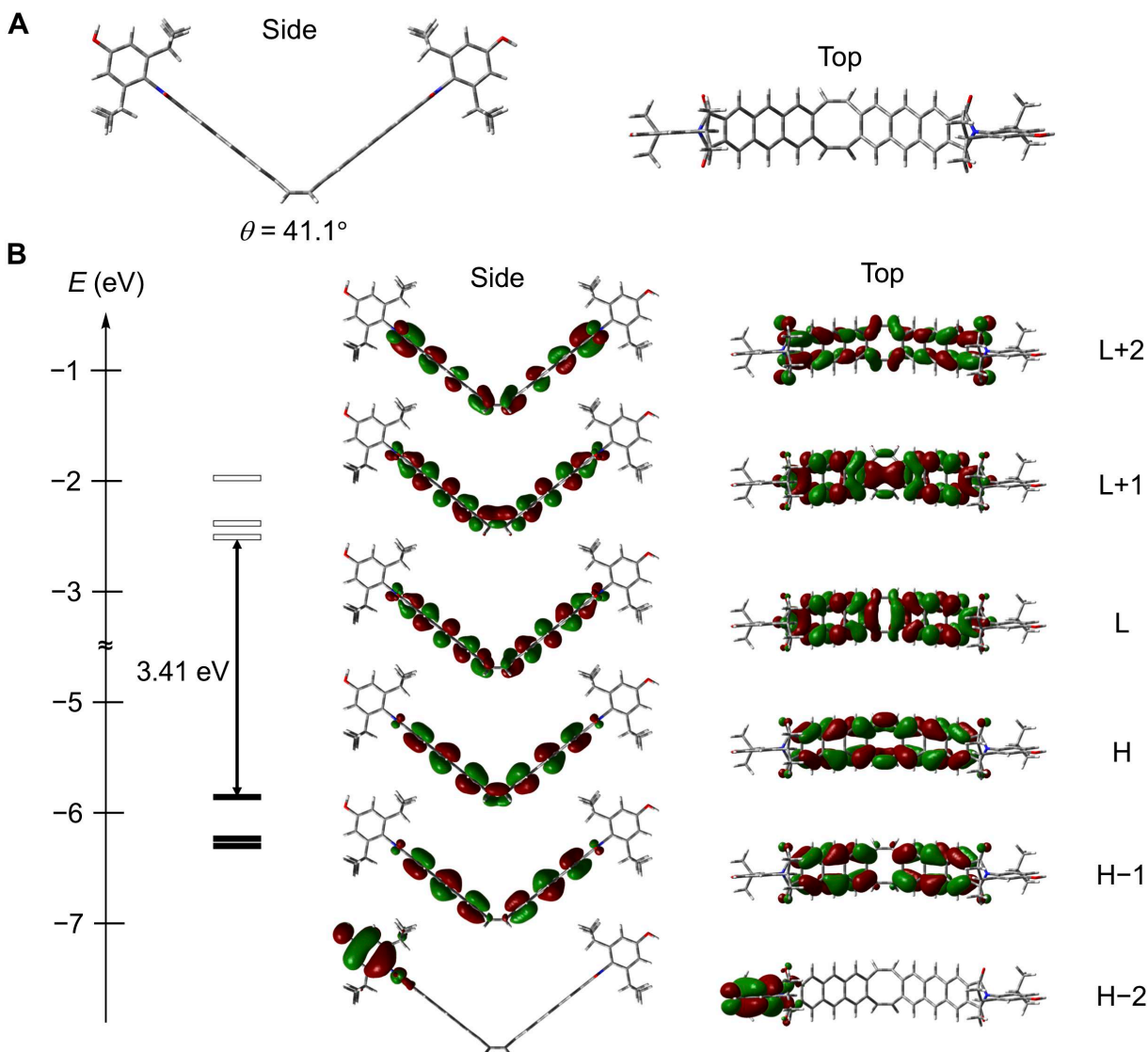


Fig. S4. (A) S_0 optimized geometry of **FLAP1** at the PBE0/6-31+G(d) level and (B) the representative molecular orbitals and their energy levels.

Table S3. Excitation energies, configurations, and oscillator strengths of the $S_0 \rightarrow S_n$ ($n \leq 3$) transitions for the S_0 optimized **FLAP1** at the TD PBE0/6-31+G(d) level.

Transition	Excitation energy	Configuration(s)	Oscillator strength
$S_0 \rightarrow S_1$	2.89 eV (429 nm)	H \rightarrow L (96%)	0.0000
$S_0 \rightarrow S_2$	2.99 eV (415 nm)	H-1 \rightarrow L (7%) H \rightarrow L+1 (93%)	0.0385
$S_0 \rightarrow S_3$	3.19 eV (389 nm)	H-7 \rightarrow L+1 (4%) H-6 \rightarrow L (16%) H-1 \rightarrow L+3 (8%) H \rightarrow L+2 (68%)	0.2660

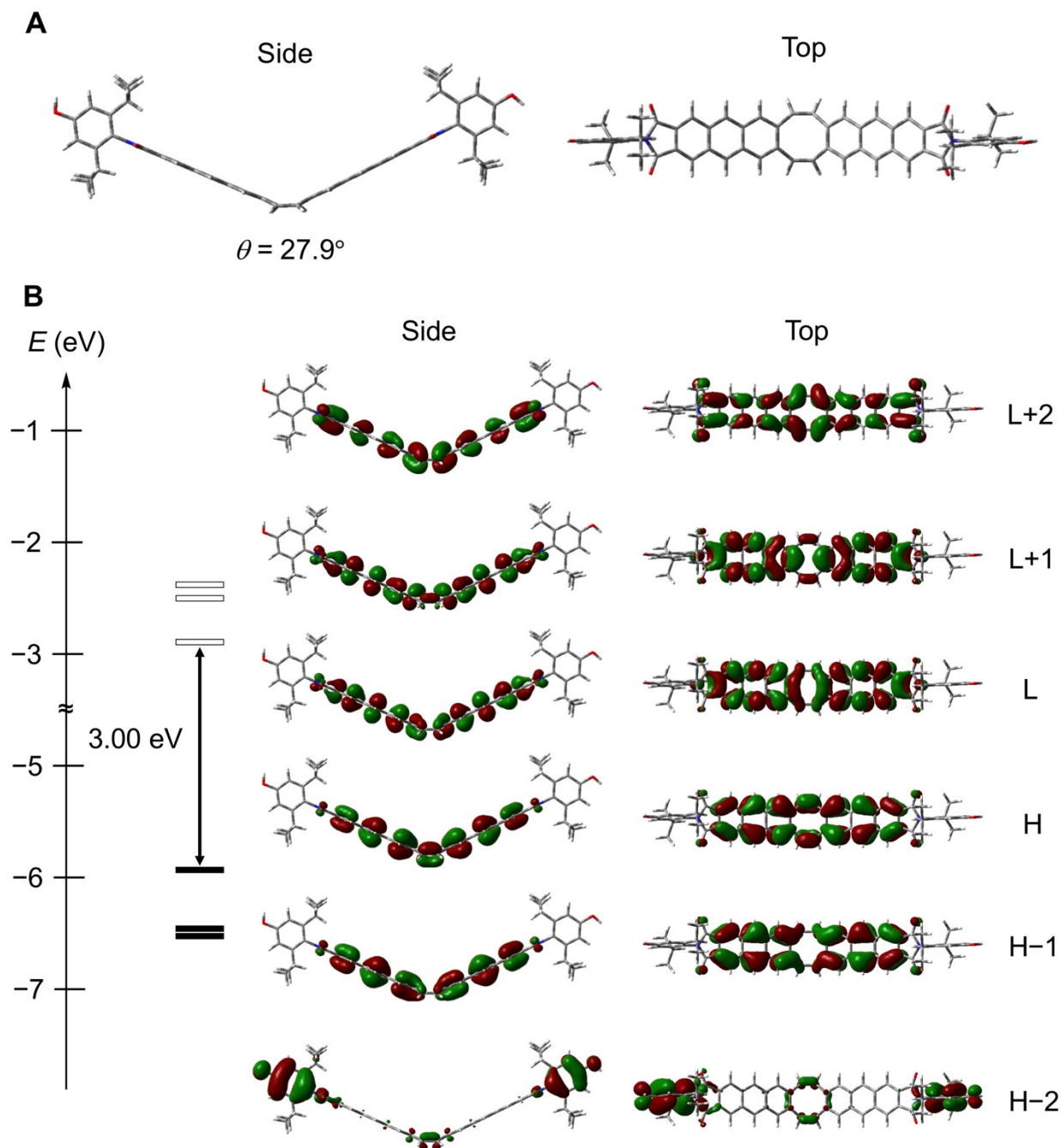


Fig. S5. (A) S_1 optimized geometry of **FLAP1** (bent) at the TD PBE0/6-31G+(d) level and (B) the representative molecular orbitals and their energy levels.

Table S4. Excitation energy, configuration, and oscillator strength of the $S_0 \rightarrow S_1$ transition for the S_1 optimized **FLAP1** (bent) at the TD PBE0/6-31+G(d) level.

Transition	Excitation energy	Configuration	Oscillator strength
$S_0 \rightarrow S_1$	2.52 eV (492 nm)	H \rightarrow L (98%)	0.0000

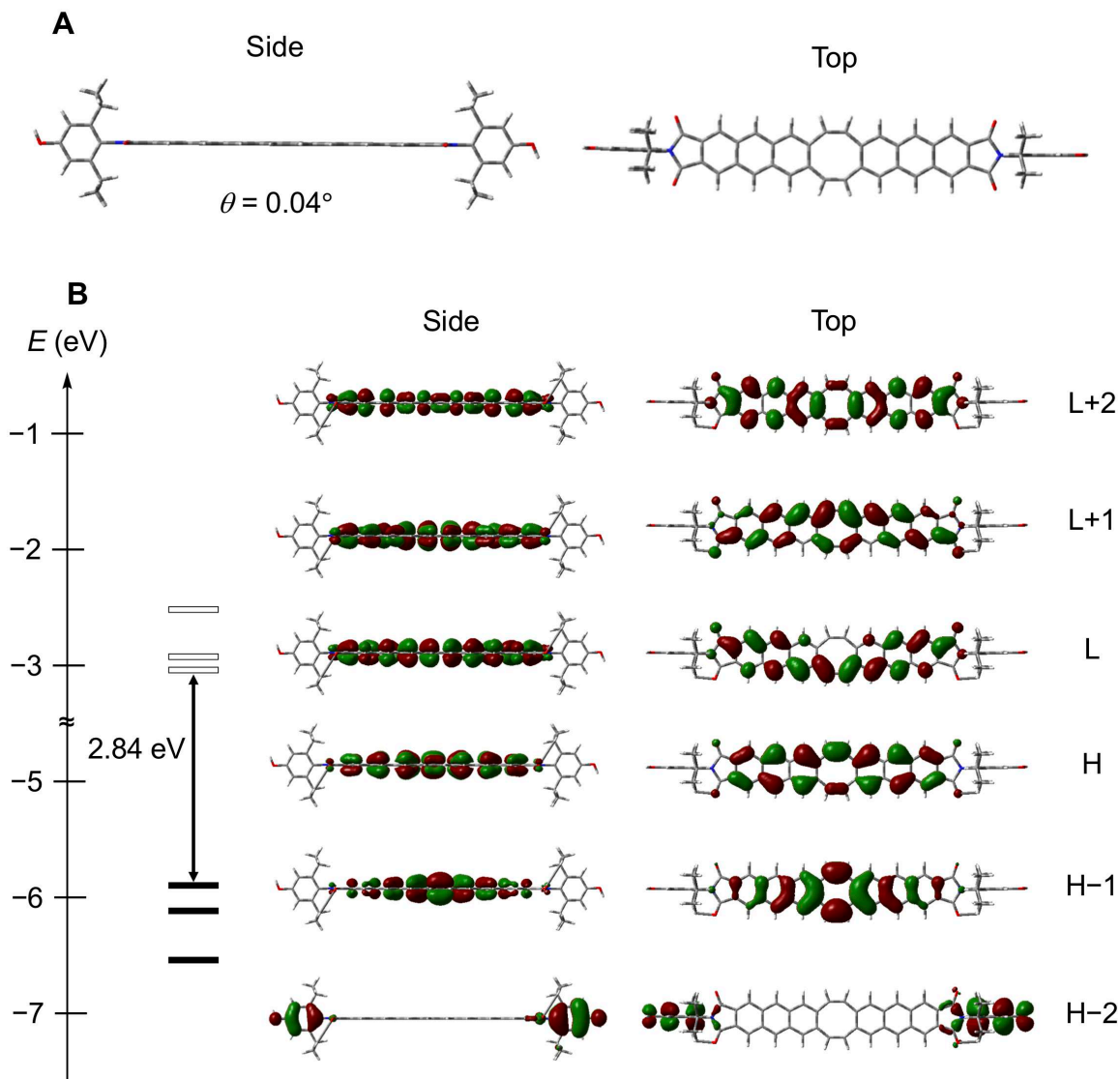


Fig. S6. (A) S_1 optimized geometry of FLAP1 (planar) at the TD PBE0/6-31G+(d) level and (B) the representative molecular orbitals and their energy levels.

Table S5. Excitation energy, configurations, and oscillator strength of the $S_0 \rightarrow S_1$ transition for the S_1 optimized FLAP1 (planar) at the TD PBE0/6-31+G(d) level.

Transition	Excitation energy	Configurations	Oscillator strength
$S_0 \rightarrow S_1$	2.21 eV (561 nm)	H-1 \rightarrow L (35%) H \rightarrow L (44%) H \rightarrow L+1 (19%)	0.0731

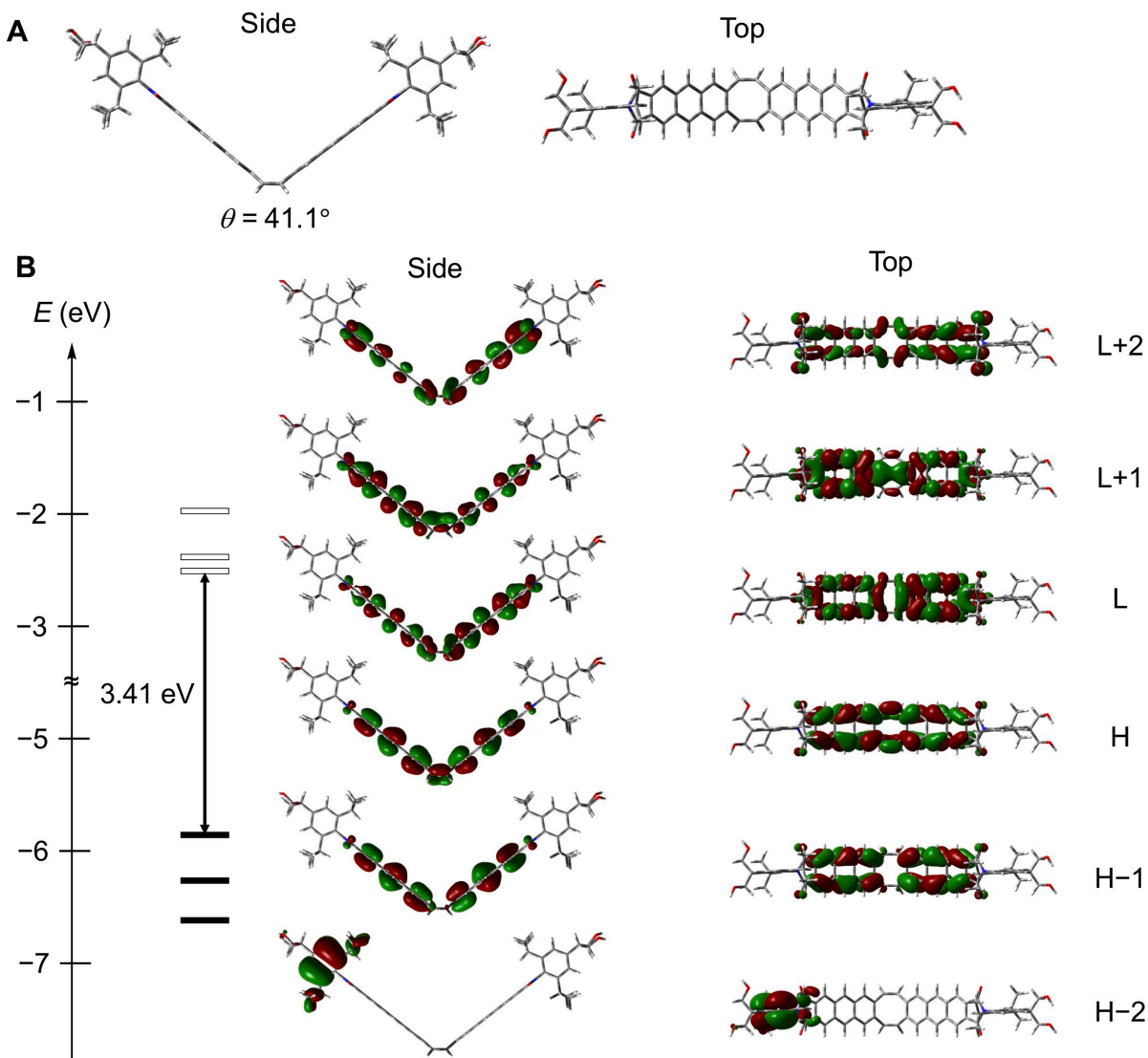


Fig. S7. (A) S_0 optimized geometry of **FLAP2** at the PBE0/6-31+G(d) level and (B) the representative molecular orbitals and their energy levels.

Table S6. Excitation energies, configurations, and oscillator strengths of the $S_0 \rightarrow S_n$ ($n \leq 3$) transitions for the S_0 optimized **FLAP2** at the TD PBE0/6-31+G(d) level.

Transition	Excitation energy	Configuration(s)	Oscillator strength
$S_0 \rightarrow S_1$	2.89 eV (429 nm)	H \rightarrow L (96%)	0.0000
$S_0 \rightarrow S_2$	2.99 eV (415 nm)	H-1 \rightarrow L (7%) H \rightarrow L+1 (92%)	0.0387
$S_0 \rightarrow S_3$	3.19 eV (389 nm)	H-7 \rightarrow L+1 (4%) H-6 \rightarrow L (13%) H-1 \rightarrow L+3 (8%) H \rightarrow L+2 (69%)	0.2882

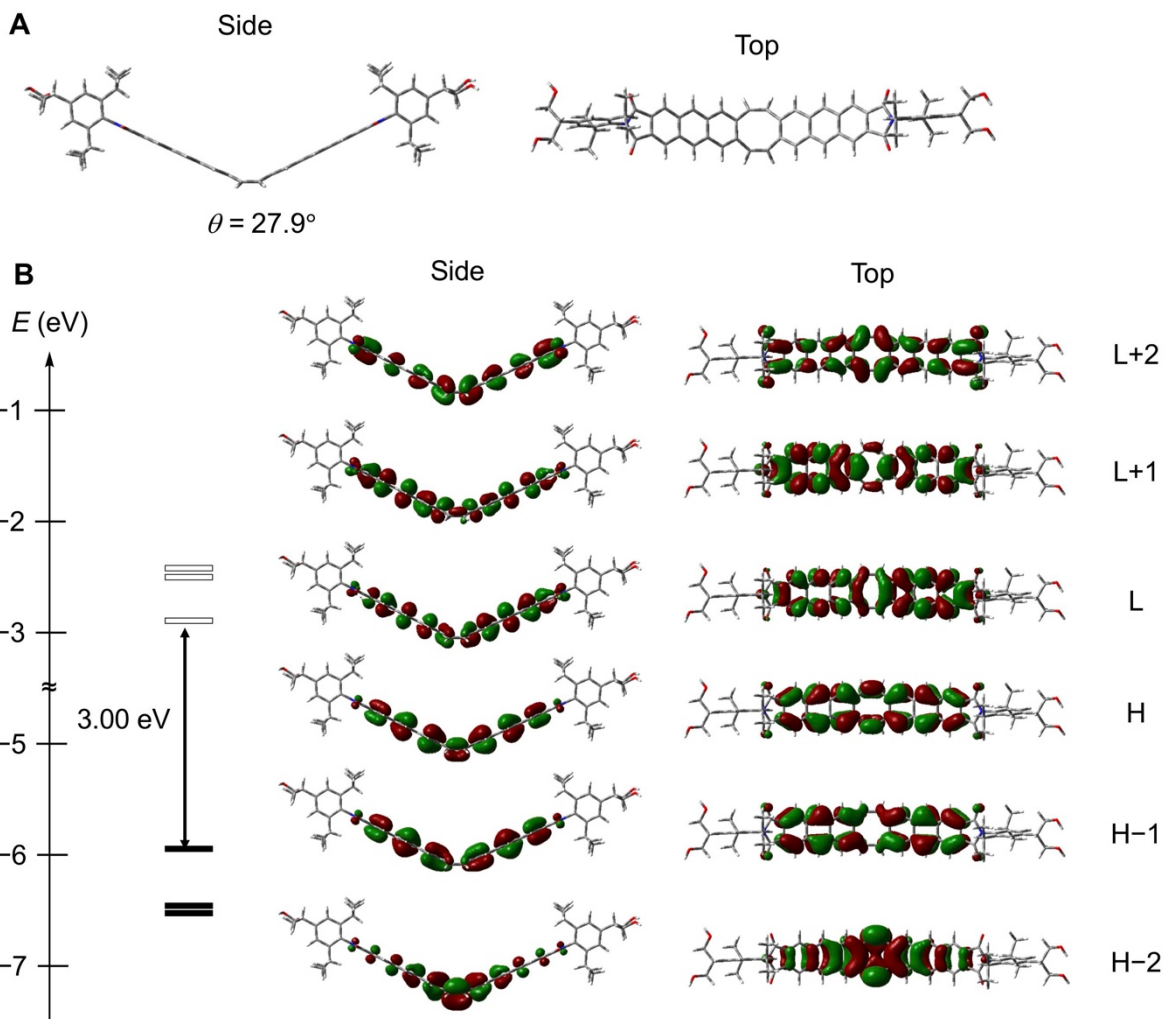


Fig. S8. (A) S₁ optimized geometry of FLAP2 (bent) at the TD PBE0/6-31G+(d) level and (B) the representative molecular orbitals and their energy levels.

Table S7. Excitation energy, configuration, and oscillator strength of the S₀ → S₁ transition for the S₁ optimized FLAP2 (bent) at the TD PBE0/6-31+G(d) level.

Transition	Excitation energy	Configuration	Oscillator strength
S ₀ → S ₁	2.52 eV (492 nm)	H → L (98%)	0.0005

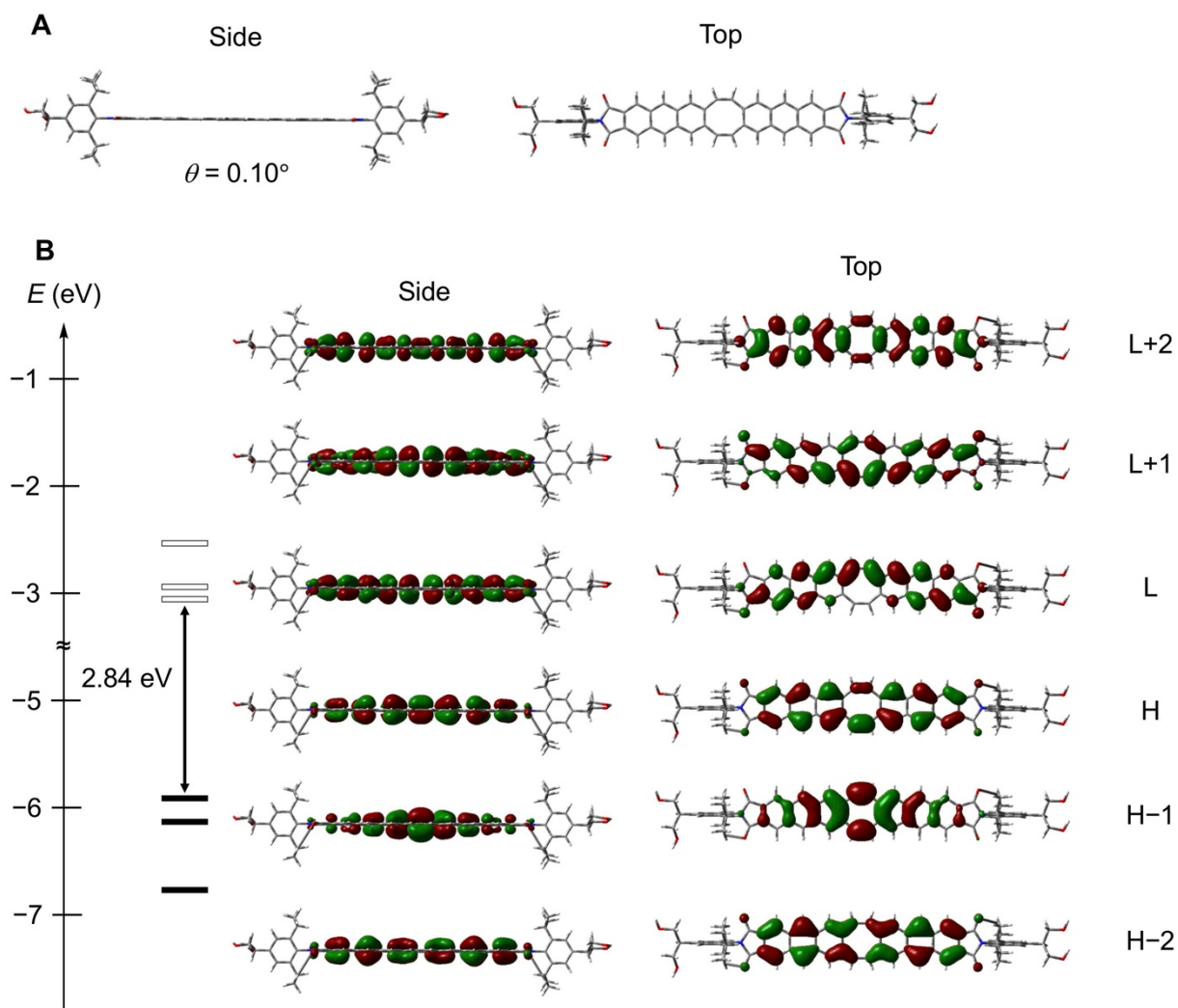


Fig. S9. (A) S₁ optimized planar geometry of FLAP2 (planar) at the TD PBE0/6-31G+(d) level and (B) representative molecular orbitals and their energy levels.

Table S8. Excitation energy, configurations, and oscillator strength of the S₀ → S₁ transition for planar S₁ optimized FLAP2 at the TD PBE0/6-31+G(d) level.

Transition	Excitation energy	Configurations	Oscillator strength
S ₀ → S ₁	2.21 eV (561 nm)	H-1 → L (35%) H → L (44%) H → L+1 (19%)	0.0749

Calculations performed at the CAM-B3LYP/6-31+G(d) level of theory

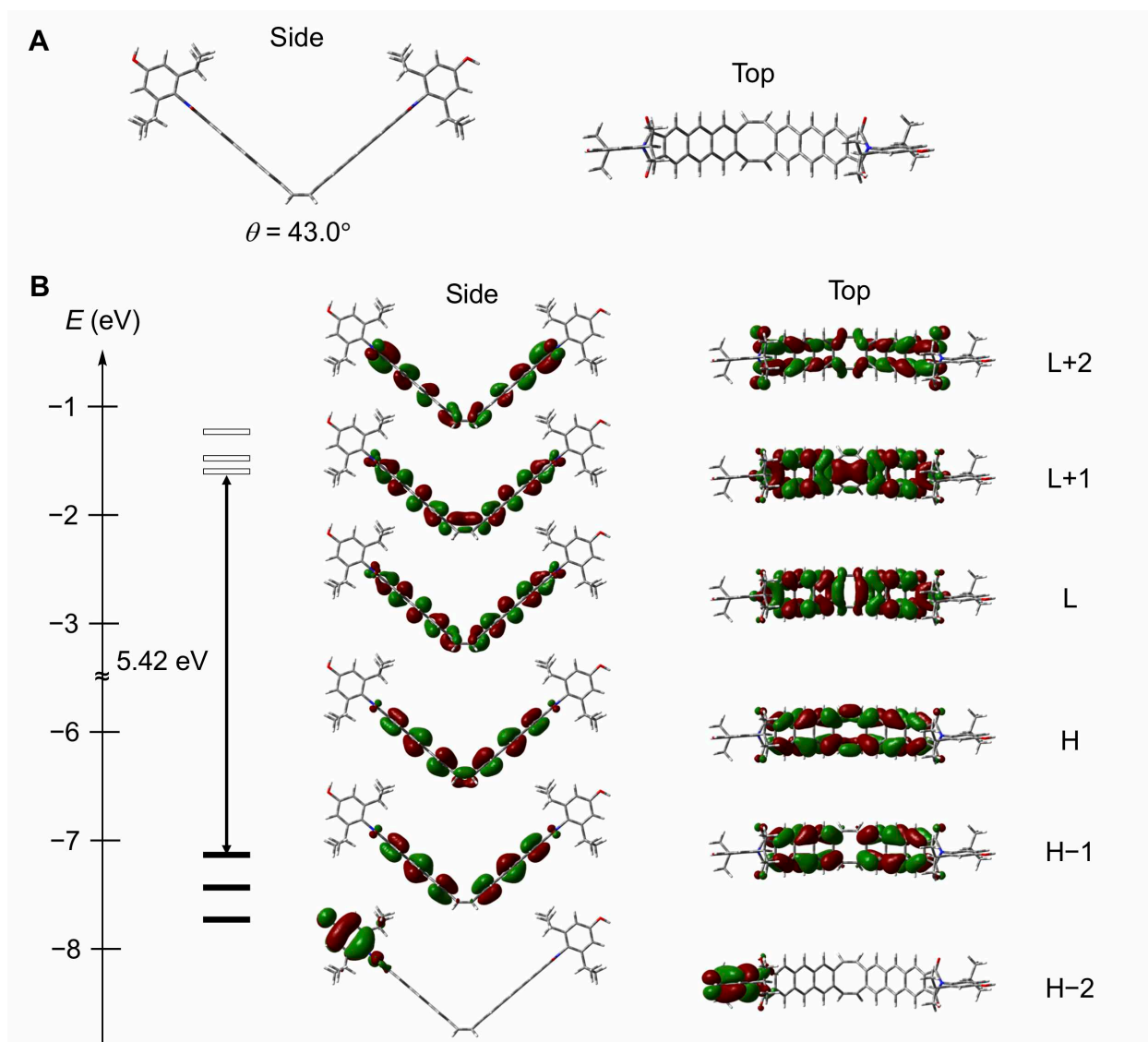


Fig. S10. (A) S_0 optimized geometry of **FLAP1** at the CAM-B3LYP/6-31+G(d) level and (B) the representative molecular orbitals and their energy levels.

Table S9. Excitation energies, configurations and oscillator strengths of the $S_0 \rightarrow S_n$ ($n \leq 3$) transitions for the S_0 optimized **FLAP1** at the TD CAM-B3LYP/6-31+G(d) level.

Transition	Excitation energy	Configurations	Oscillator strength
$S_0 \rightarrow S_1$	3.38 eV (367 nm)	H-1 \rightarrow L+1 (33%) H \rightarrow L (63%)	0.0000
$S_0 \rightarrow S_2$	3.40 eV (365 nm)	H-1 \rightarrow L (40%) H \rightarrow L+1 (57%)	0.0847
$S_0 \rightarrow S_3$	3.65 eV (340 nm)	H-7 \rightarrow L+1 (11%) H-5 \rightarrow L (15%) H-1 \rightarrow L+3 (22%) H \rightarrow L+2 (43%)	0.2185

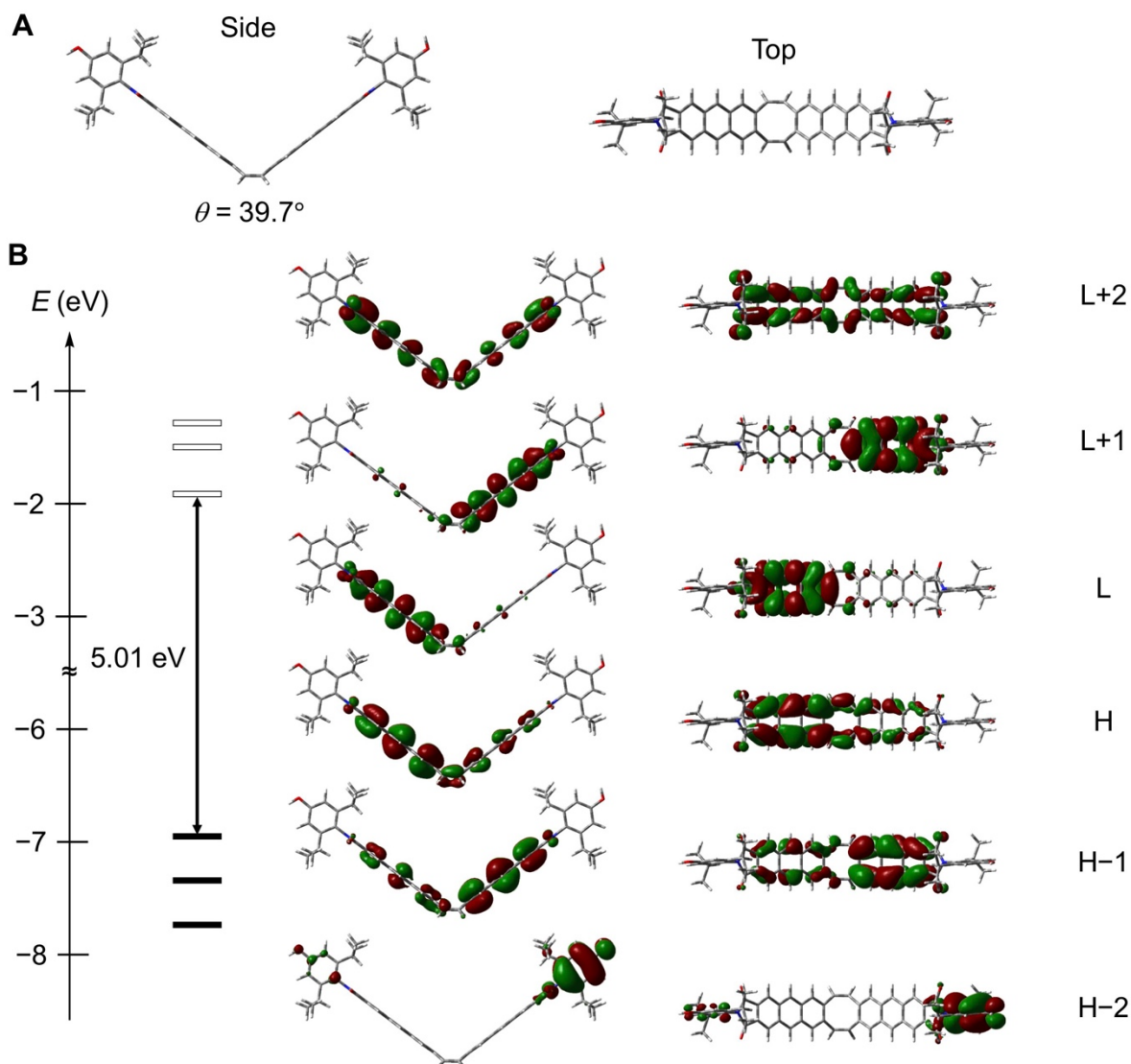


Fig. S11. (A) S_1 optimized geometry of **FLAP1** at the TD CAM-B3LYP/6-31G+(d) level and (B) the representative molecular orbitals and their energy levels.

Table S10. Excitation energy, configurations, and oscillator strength of the $S_0 \rightarrow S_1$ transition for the S_1 optimized **FLAP1** (bent) at the TD CAM-B3LYP/6-31+G(d) level.

Transition	Excitation energy	Configurations	Oscillator strength
$S_0 \rightarrow S_1$	2.90 eV (428 nm)	H-1 \rightarrow L (8%) H \rightarrow L (88%)	0.0423

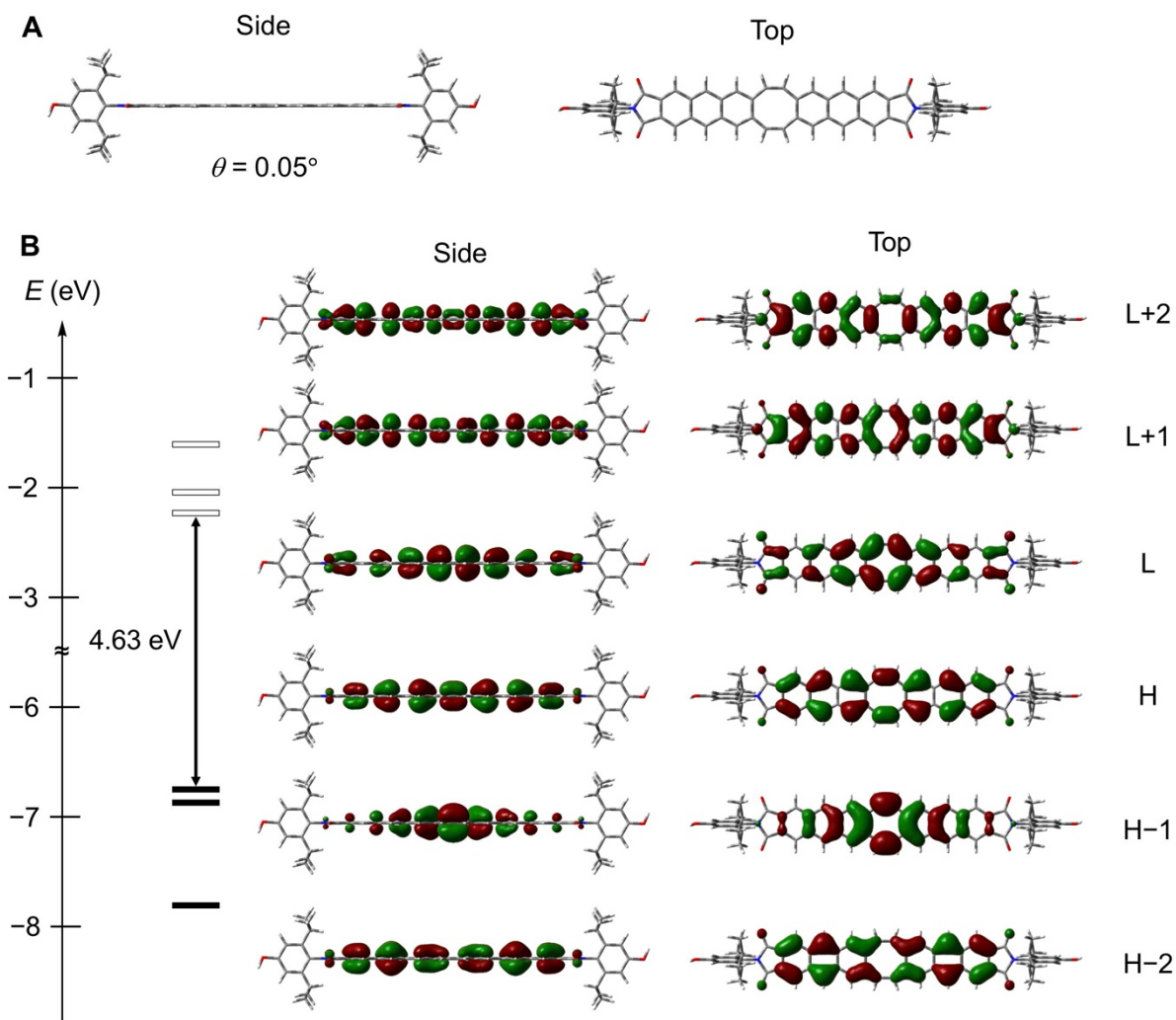


Fig. S12. (A) S_1 optimized geometry of FLAP1 (planar) at the TD CAM-B3LYP/6-31G+(d) level and (B) the representative molecular orbitals and their energy levels.

Table S11. Excitation energy, configuration, and oscillator strength of the $S_0 \rightarrow S_1$ transition for the S_1 optimized FLAP1 (planar) at the TD CAM-B3LYP/6-31+G(d) level.

Transition	Excitation energy	Configuration	Oscillator strength
$S_0 \rightarrow S_1$	2.22 eV (558 nm)	H \rightarrow L (94%)	0.0000

Computational studies of the polymer-chain substructure in the vicinity of FLAP

The following substructure of a FLAP-doped polyurethane chain, **FLAP1'**, was calculated in Fig. 3 of the main text. The distance between the C^A and C^B atoms was fixed in each optimization by using the *opt=modredundant* keyword of Gaussian16.

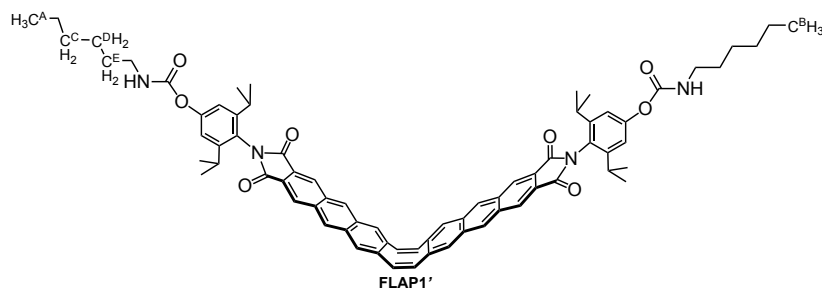


Fig. S13. Substructure of a FLAP-doped polyurethane chain, **FLAP1'**, in Fig. 3.

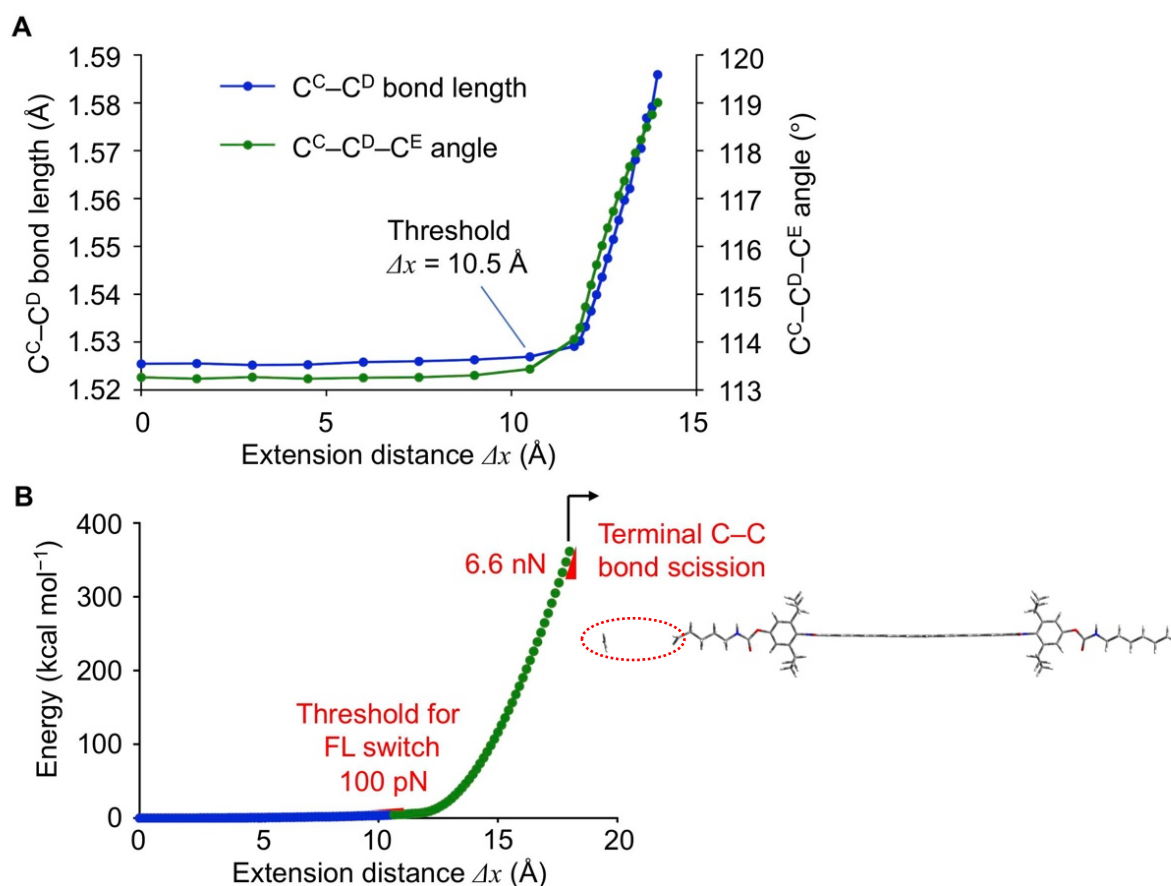


Fig. S14. (A) Changes in the C^C-C^D bond length and the $C^C-C^D-C^E$ bond angle of **FLAP1'**. The bond length and angle are not remarkably increased at the threshold for the FL switch, indicating the FL response of the FLAP force probe before mechanical damage. (B) Calculated energy diagram of **FLAP1'** until the formal C–C bond scission at the PBE0/6-31G(d) level.

Calculated electronic transitions for the absorption

To interpret the absorption spectral change of the polyurethane film upon mechanical testing, TD-DFT calculations of FLAPI' were performed for the unstretched ($\Delta x = 0 \text{ \AA}$) and fully stretched ($\Delta x = 13.0 \text{ \AA}$) geometries. Details of the calculation results in Fig. 3E are shown below.

Table S12. Excitation energies ($> 360 \text{ nm}$), configurations, and oscillator strengths of the $S_0 \rightarrow S_n$ transitions for the unstretched ($\Delta x = 0 \text{ \AA}$) geometry at the TD PBE0/6-31+G(d) level.

Transition	Excitation energy	Configuration(s)	Oscillator strength
$S_0 \rightarrow S_1$	2.87 eV (431 nm)	H \rightarrow L (97%)	0.0000
$S_0 \rightarrow S_2$	2.99 eV (415 nm)	H-1 \rightarrow L (7%) H \rightarrow L+1 (92%)	0.0377
$S_0 \rightarrow S_3$	3.16 eV (391 nm)	H-6 \rightarrow L (16%) H-2 \rightarrow L (2%) H-1 \rightarrow L+3 (7%) H \rightarrow L+2 (69%)	0.2858
$S_0 \rightarrow S_4$	3.20 eV (389 nm)	H-1 \rightarrow L (91%) H \rightarrow L+1 (7%)	0.0149
$S_0 \rightarrow S_5$	3.30 eV (376 nm)	H-6 \rightarrow L+1 (22%) H-2 \rightarrow L+1 (4%) H-1 \rightarrow L+2 (29%) H \rightarrow L+3 (33%)	0.0299
$S_0 \rightarrow S_6$	3.31 eV (375 nm)	H-1 \rightarrow L+1 (96%)	0.0000

Table S13. Excitation energies ($> 360 \text{ nm}$), configurations, and oscillator strengths of the $S_0 \rightarrow S_n$ transitions for the fully stretched ($\Delta x = 13.0 \text{ \AA}$) geometry at the TD PBE0/6-31+G(d) level.

Transition	Excitation energy	Configurations	Oscillator strength
$S_0 \rightarrow S_1$	2.55 eV (486 nm)	H \rightarrow L (98%)	0.0000
$S_0 \rightarrow S_2$	2.58 eV (481 nm)	H-1 \rightarrow L (38%) H \rightarrow L+1 (59%)	0.1196
$S_0 \rightarrow S_3$	2.89 eV (429 nm)	H-1 \rightarrow L+1 (95%) H-1 \rightarrow L+4 (3%)	0.0000
$S_0 \rightarrow S_4$	2.92 eV (425 nm)	H \rightarrow L+2 (96%)	0.0228
$S_0 \rightarrow S_5$	3.09 eV (401 nm)	H-2 \rightarrow L+1 (37%) H-1 \rightarrow L+2 (49%) H \rightarrow L+3 (9%)	0.0000
$S_0 \rightarrow S_6$	3.14 eV (395 nm)	H-1 \rightarrow L (59%) H \rightarrow L+1 (38%)	5.4348
$S_0 \rightarrow S_7$	3.19 eV (389 nm)	H-2 \rightarrow L (95%) H \rightarrow L+2 (3%)	0.0185
$S_0 \rightarrow S_8$	3.39 eV (366 nm)	H-4 \rightarrow L+2 (10%) H-3 \rightarrow L (87%)	0.0000
$S_0 \rightarrow S_9$	3.39 eV (366 nm)	H-4 \rightarrow L (87%) H-3 \rightarrow L+2 (10%)	0.0236

Synthesis and characterization of the linear polycarbonates (PCs)

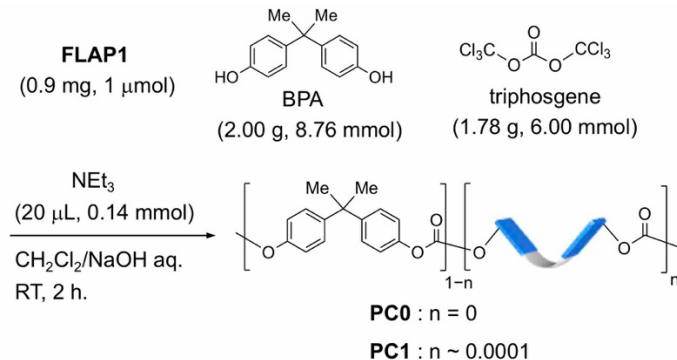


Fig. S15. Synthesis of the linear polycarbonates (PCs). The amount of **FLAP1** is given for the **PC1** synthesis, while **PC0** does not contain **FLAP1**.

Bisphenol A (BPA) was recrystallized in advance from AcOH, and washed with H₂O. To the mixture of bisphenol A (BPA) (2.00 g, 8.76 mmol) and NaOH (2.73 g, 68.2 mmol) in H₂O (20 mL), **FLAP1** (0.9 mg, 1 μ mol) and triphosgene (2.60 g, 8.76 mmol) in CH₂Cl₂ (20 mL) were added. After addition of triethylamine (TEA) (20 μ L, 0.14 mmol), the reaction mixture was stirred vigorously at 25 °C for 2 h. Then, the aqueous layer was removed by decantation and the remaining organic layer was poured into MeOH (100 mL). The precipitation was washed with MeOH (100 mL) followed by H₂O (100 mL), and dried under vacuum to give a lump of **PC1** (~ 2.3 g). To obtain **PC0**, the same procedure was performed without **FLAP1**. The resulting linear PCs were soluble in common organic solvents, and therefore shape of the PC samples can be easily designed. By punching a PC sheet, a dumbbell-shaped specimen, JIS K 6251 (No. 3) meeting the requirements of ISO 37, was obtained.

PC0: ¹H NMR (600 MHz, CDCl₃) δ (ppm) 7.25–7.23 (m, 4H), 7.17–7.15 (m, 4H), and 1.67 (s, 6H).

PC1: ¹H NMR (600 MHz, CDCl₃) δ (ppm) 7.25–7.24 (m, 4H), 7.17–7.15 (m, 4H), and 1.68 (s, 6H). Note that peaks arising from the FLAP dopant were too small to detect.

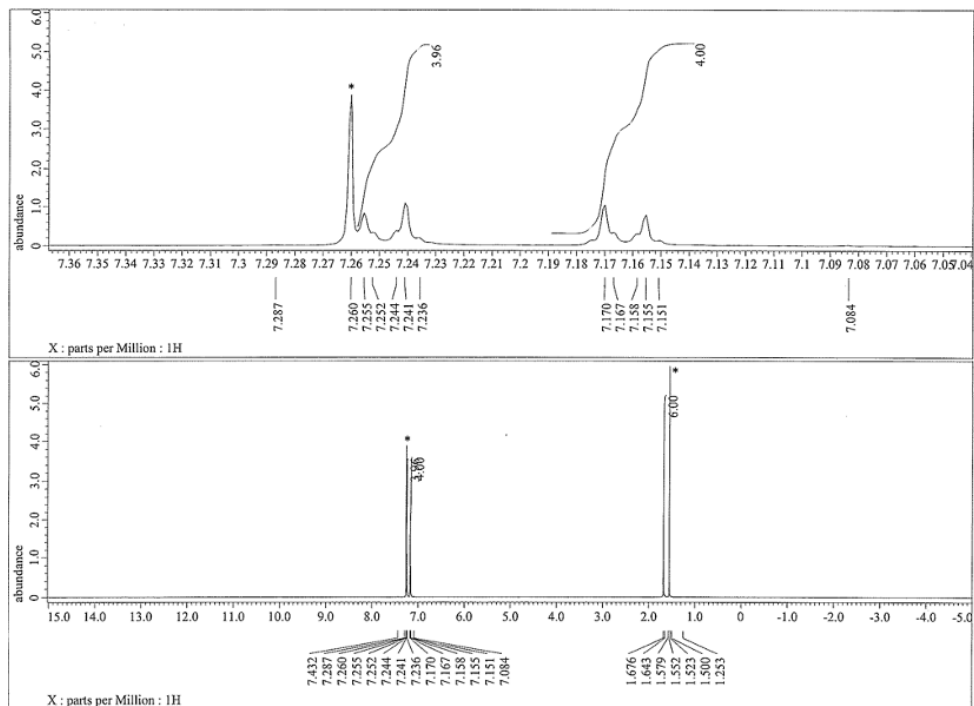


Fig. S16. ^1H NMR spectrum of PC0 in CDCl_3 at 25°C . Peaks marked with * indicate residual solvents.

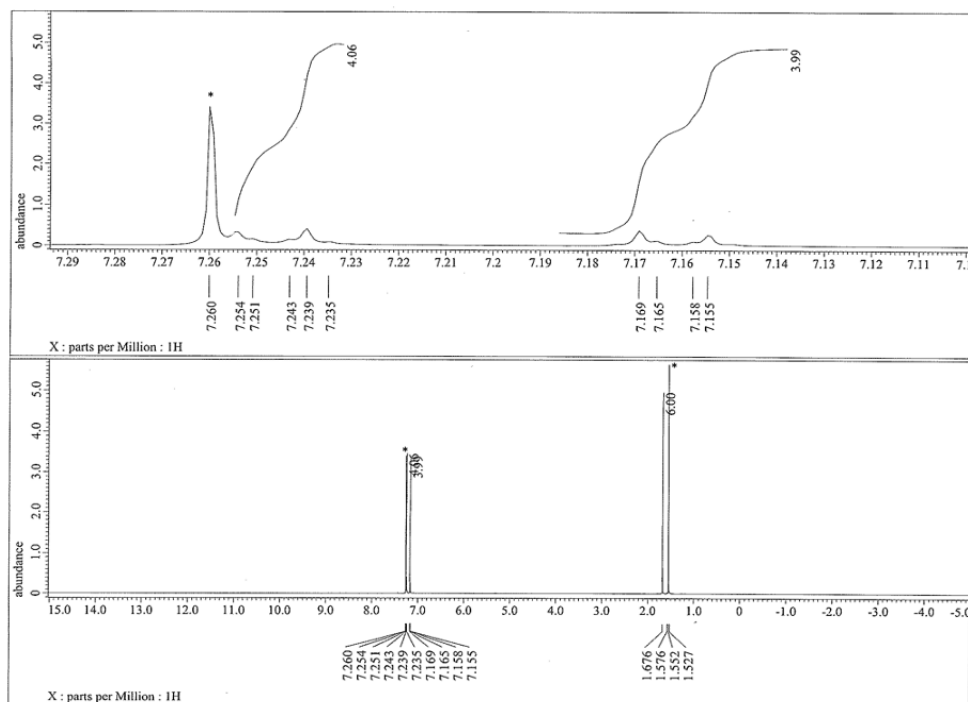


Fig. S17. ^1H NMR spectrum of PC1 in CDCl_3 at 25°C . Peaks marked with * indicate residual solvents.

DSC analysis of the linear polycarbonates (PCs)

Differential scanning calorimetry (DSC) measurement of the linear polycarbonates (PCs) was conducted under N_2 atmosphere at a flow speed of 30 mL min^{-1} . Programmed heating and cooling cycles are shown in Fig S18. Fig S19 shows DSC profiles of the 2nd cooling (E→F) and heating (G→H) cycles. Each sample was placed into an aluminum pan and covered with an aluminum cover, which was well pressed with a designated pressing tool. As a reference sample, a vacant pan was also pressed with the cover.

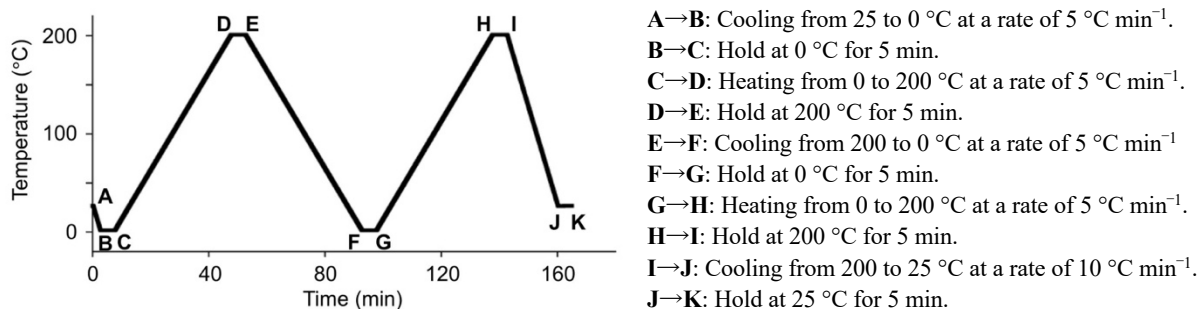


Fig. S18. Programmed heating and cooling cycles in the DSC measurement of the PCs.

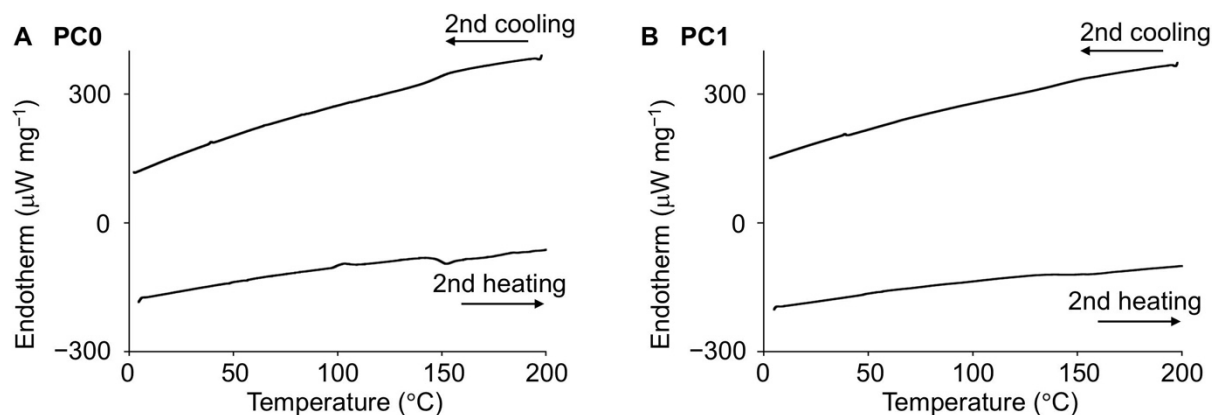


Fig. S19. DSC traces of PC0 and PC1. Glass transition temperatures (T_g) were estimated to be 151 °C for PC0 and 153 °C for PC1.

Mechanical properties of the linear polycarbonates (PCs)

Uniaxial tensile tests were carried out on dumbbell-shaped specimens. True strain (ϵ_{true}) is calculated by $\epsilon_{\text{true}} = \ln(L/L_0)$, where L means crosshead displacement and the initial length $L_0 = 30$ mm. True stress (σ_{true}) is calculated by $\sigma_{\text{true}} = F/A$, where F is the recorded force and A is the cross-sectional area of the deformed specimen, approximated by $A = A_0(L_0/L)$. Toughness was calculated as the integrated area under the true stress–strain curve. Young’s modulus was defined as the slope of stress–strain curves at 0–1% true strain. Stretching rate was fixed at 5 mm min^{-1} , corresponding to the strain rate of $2.8 \times 10^{-3} \text{ s}^{-1}$.

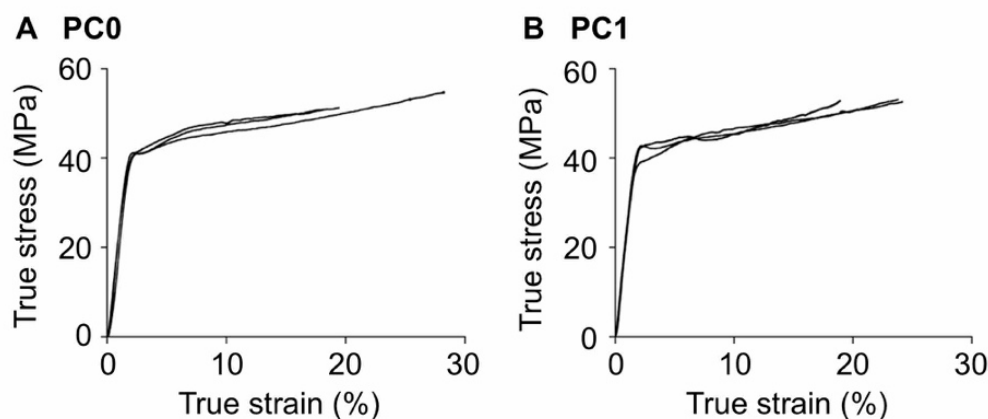


Fig. S20. Stress-strain curves of PC0 and PC1.

Table S14. Mechanical properties for the PCs.

	True rupture strain (%)	True rupture stress (MPa)	Toughness (MJ m^{-3})	Young's modulus (GPa)
PC0	22.0 ± 5.4	52.3 ± 2.1	10.3 ± 2.3	2.20 ± 0.28
PC1	22.3 ± 2.9	52.9 ± 0.3	10.0 ± 1.4	2.49 ± 0.10

Photophysical properties of the unstretched polycarbonate (PC)

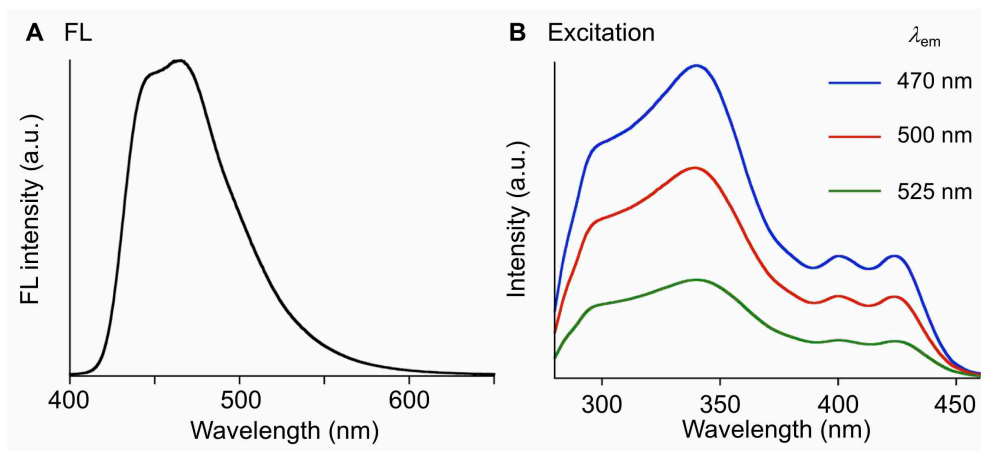


Fig. S21. (A) FL spectrum ($\lambda_{ex} = 365$ nm) and (B) excitation spectra of the **PC1** film. No excimer emission was observed.

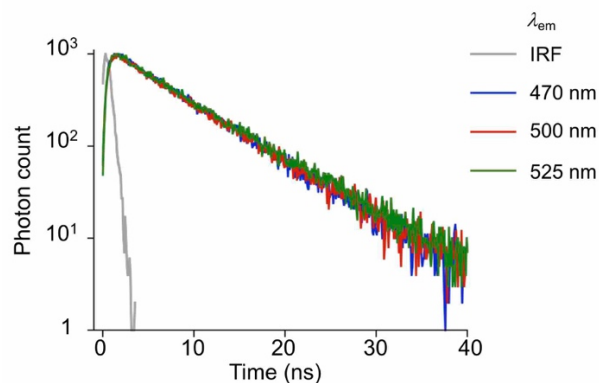


Fig. S22. FL decay profiles of **PC1** ($\lambda_{ex} = 365$ nm), in which the FL lifetime is almost constant ($\tau_{FL} = 6.8$ – 7.0 ns) regardless of the monitored FL wavelengths.

Table S15. Photophysical constants of **PC1**. $\lambda_{ex} = 365$ nm.

Φ_{FL}	τ_{FL} (ns) ^a	k_r (s ⁻¹)	k_{nr} (s ⁻¹)
0.30	6.8	4.4×10^7	1.0×10^8

^a $\lambda_{em} = 470$ nm.

Synthesis of the crosslinked polyurethanes (PUs)

Poly(tetrahydrofuran) (PTHF, $M_n \sim 650$, Aldrich) was dried under vacuum (~ 2 torr) for 2 h at 70 °C. After cooling to 25 °C, dimethylformamide (DMF, Super dehydrated grade, Wako Chemicals), a trace of FLAP dopant (**FLAP1** or **FLAP2**), hexamethylene diisocyanate (HDI, TCI chemicals) and triethanolamine (TEA, Wako Chemicals) were added, and the reaction mixture was stirred at 25 °C for 10 min. Then, dibutyltin dilaurate (DBTDL, Aldrich) (30 μ L, 50 μ mol) in THF (0.5 mL) was added to the reaction and stirred at 25 °C for 2 min. The reaction mixture was poured into a custom-made mold of PTFE (polytetrafluoroethylene), and polymerized under N₂ atmosphere at 25 °C for 48 h. Then, dumbbell-shaped polyurethane (PU) specimens were washed with H₂O and dried under vacuum for 8 h at 70 °C to obtain transparent PU films, **PU1** or **PU2**, with thickness of 1.5 mm and width of 6 mm. **PU0** was obtained by the same procedure without the FLAP dopant.

The average distance between the FLAP molecules doped in PU was estimated to be 20 nm as follows; the weight ratio of FLAP to the polymer was 0.2 mg g⁻¹ equal to 0.2 μ mol m⁻³ (polymer density: 1.0 g cm⁻³). Therefore, the average volume occupied by a single FLAP molecule was calculated to be 8.0 $\times 10^{-24}$ m³. Taking the cube root, the average distance between the FLAP molecules was determined to be 2.0 $\times 10^{-8}$ m³ (20 nm).

Table S16. Components and solvent in the synthesis of **PU0**.

	PU0 (8.7%TEA)	PU0 (10%TEA)	PU0 (13%TEA)
PTHF	5.22 g (8.03 mmol)	4.80 g (7.38 mmol)	4.99 g (7.68 mmol)
HDI	1.73 mL (10.8 mmol)	1.65 mL (10.3 mmol)	1.94 mL (12.1 mmol)
TEA	268 mg (1.80 mmol)	292 mg (1.96 mmol)	439 mg (2.94 mmol)
DMF	14.9 mL	13.9 mL	14.5 mL

Table S17. Components and solvent in the synthesis of **PU1**.

	PU1 (8.7%TEA)	PU1 (10%TEA)	PU1 (13%TEA)
FLAP1	1.5 mg (1.7 μ mol)	1.3 mg (1.5 μ mol)	1.6 mg (1.8 μ mol)
PTHF	5.14 g (7.91 mmol)	4.67 g (7.18 mmol)	5.03 g (7.74 mmol)
HDI	1.69 mL (10.5 mmol)	1.61 mL (10.0 mmol)	1.96 mL (12.2 mmol)
TEA	262 mg (1.75 mmol)	285 mg (1.91 mmol)	443 mg (2.97 mmol)
DMF	14.7 mL	13.5 mL	14.5 mL
FLAP/polymer ^a	0.21 mg g ⁻¹	0.20 mg g ⁻¹	0.21 mg g ⁻¹

^a Weight ratio of FLAP to the polymer.

Table S18. Components and solvent in the synthesis of **PU2**.

	PU2 (8.7%TEA)	PU2 (10%TEA)	PU2 (13%TEA)
FLAP2	1.5 mg (1.5 μ mol)	1.5 mg (1.5 μ mol)	1.5 mg (1.5 μ mol)
PTHF	5.21 g (8.01 mmol)	5.49 g (8.45 mmol)	4.92 g (7.57 mmol)
HDI	1.71 mL (10.6 mmol)	1.89 mL (11.8 mmol)	1.91 mL (11.9 mmol)
TEA	266 mg (1.78 mmol)	335 mg (2.24 mmol)	430 mg (2.88 mmol)
DMF	14.9 mL	15.9 mL	14.2 mL
FLAP/polymer ^a	0.21 mg g ⁻¹	0.19 mg g ⁻¹	0.20 mg g ⁻¹

^a Weight ratio of FLAP to the polymer.

DSC analysis of the crosslinked polyurethanes (PUs)

Differential scanning calorimetry (DSC) measurement of the crosslinked polyurethane (PU) specimen was conducted under N_2 atmosphere at a flow speed of 30 mL min^{-1} . Programmed heating and cooling cycles are shown in Fig S23. Fig S25 shows DSC profiles of the 2nd cooling ($E \rightarrow F$) and heating ($G \rightarrow H$) cycles. Each PU sample was placed into an aluminum pan, covered with an aluminum cover, and then pressed with a designated tool. As a reference sample, a vacant pan was also pressed with the cover.

Spontaneous crystallization behavior was more pronounced in the PU samples with a smaller crosslinking density, as suggested in the values of $\Delta H_{r \rightarrow c}$ and $\Delta H_{c \rightarrow r}$. Cross-Nicol images in Fig. S24 also suggest that the semicrystalline sample is transformed into the rubbery one upon heating.

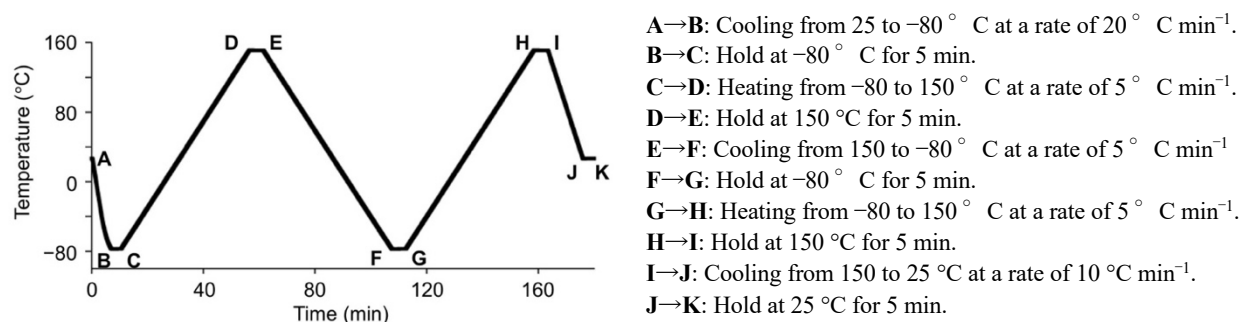


Fig. S23. Programmed heating and cooling cycles in the DSC measurement of the PUs.

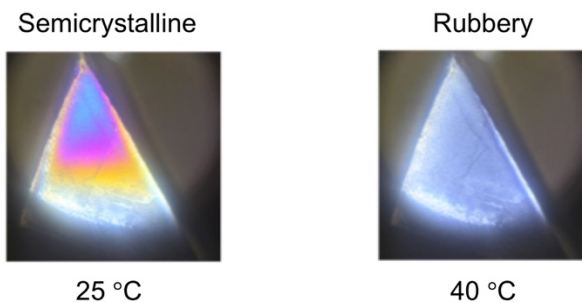


Fig. S24. Cross-Nicol images of PU0 (8.7%TEA) at 20 and 40 °C.

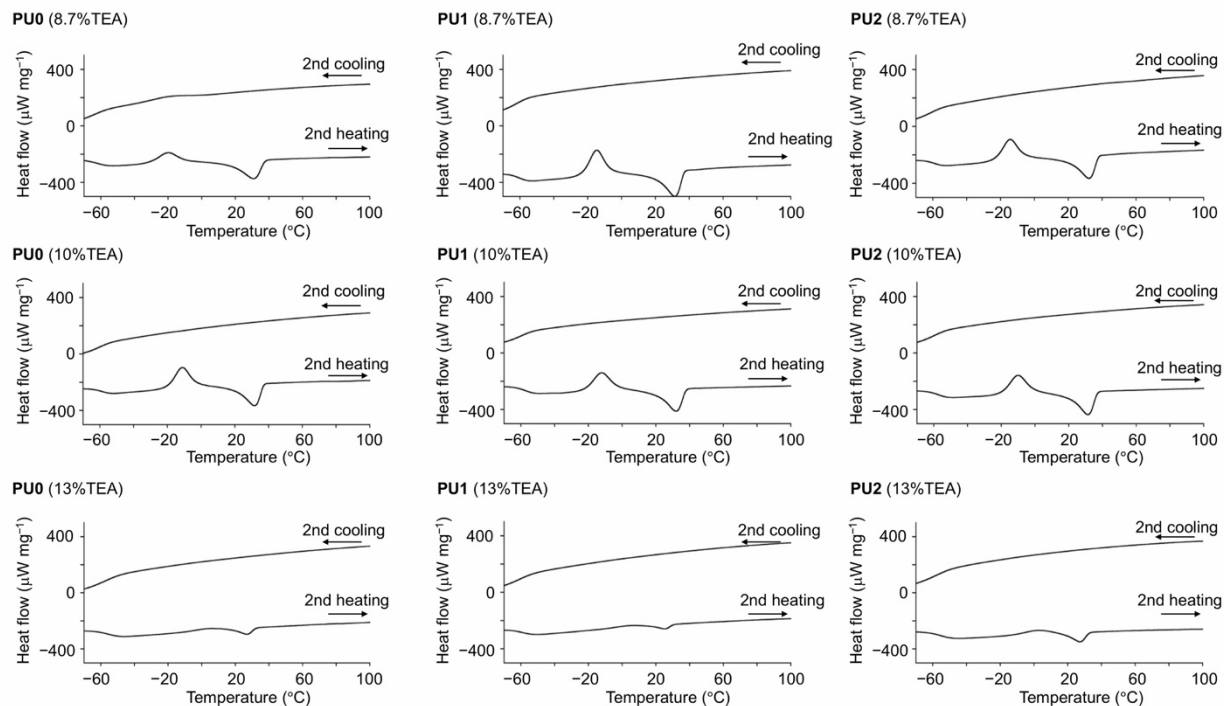


Fig. S25. DSC traces of the crosslinked PUs.

Table S19. DSC parameters of the PU films with each crosslinking density (%TEA).

	weight (mg)	T_g^a (°C)	$T_{r \rightarrow c}^b$ (°C)	$\Delta H_{r \rightarrow c}^c$ (J g ⁻¹)	$T_{c \rightarrow r}^d$ (°C)	$\Delta H_{c \rightarrow r}^e$ (J g ⁻¹)
PU0 (8.7%TEA)	7.50	-60	-19	-16	31	21
PU1 (8.7%TEA)	6.42	-60	-14	-24	31	24
PU2 (8.7%TEA)	6.25	-58	-14	-24	32	22
PU0 (10%TEA)	6.84	-58	-11	-23	32	20
PU1 (10%TEA)	9.99	-56	-12	-24	32	22
PU2 (10%TEA)	7.33	-57	-10	-26	31	19
PU0 (13%TEA)	6.67	-56	5	-3.7	27	5.7
PU1 (13%TEA)	6.01	-59	8	-2.8	25	4.0
PU2 (13%TEA)	5.88	-56	3	-3.9	27	6.5

^a Glass transition temperature determined by the 2nd heating profile.

^b Rubbery-to-semicrystalline transition temperature determined by the 2nd heating profile.

^c Enthalpy change in the rubbery-to-semicrystalline transition determined by the DSC signal area.

^d Semicrystalline-to-rubbery transition temperature determined by the 2nd heating profile.

^e Enthalpy change in the semicrystalline-to-rubbery transition determined by the DSC signal area.

Rheological analysis of the crosslinked polyurethanes (PUs)

Dynamic viscoelasticity was measured for the rubbery PUs. After heating to 100 °C, the storage modulus G' and loss modulus G'' were measured up to 0 °C at a cooling rate of 5 °C min⁻¹ (frequency: 1 Hz, a 10-mm parallel plate). As the temperature dropped, both G' and G'' increased gradually. The increments were small, and the G' value stayed in the range of 10⁵–10⁶ Pa, indicating much softer properties of the crosslinked PUs than the linear PCs prepared above.

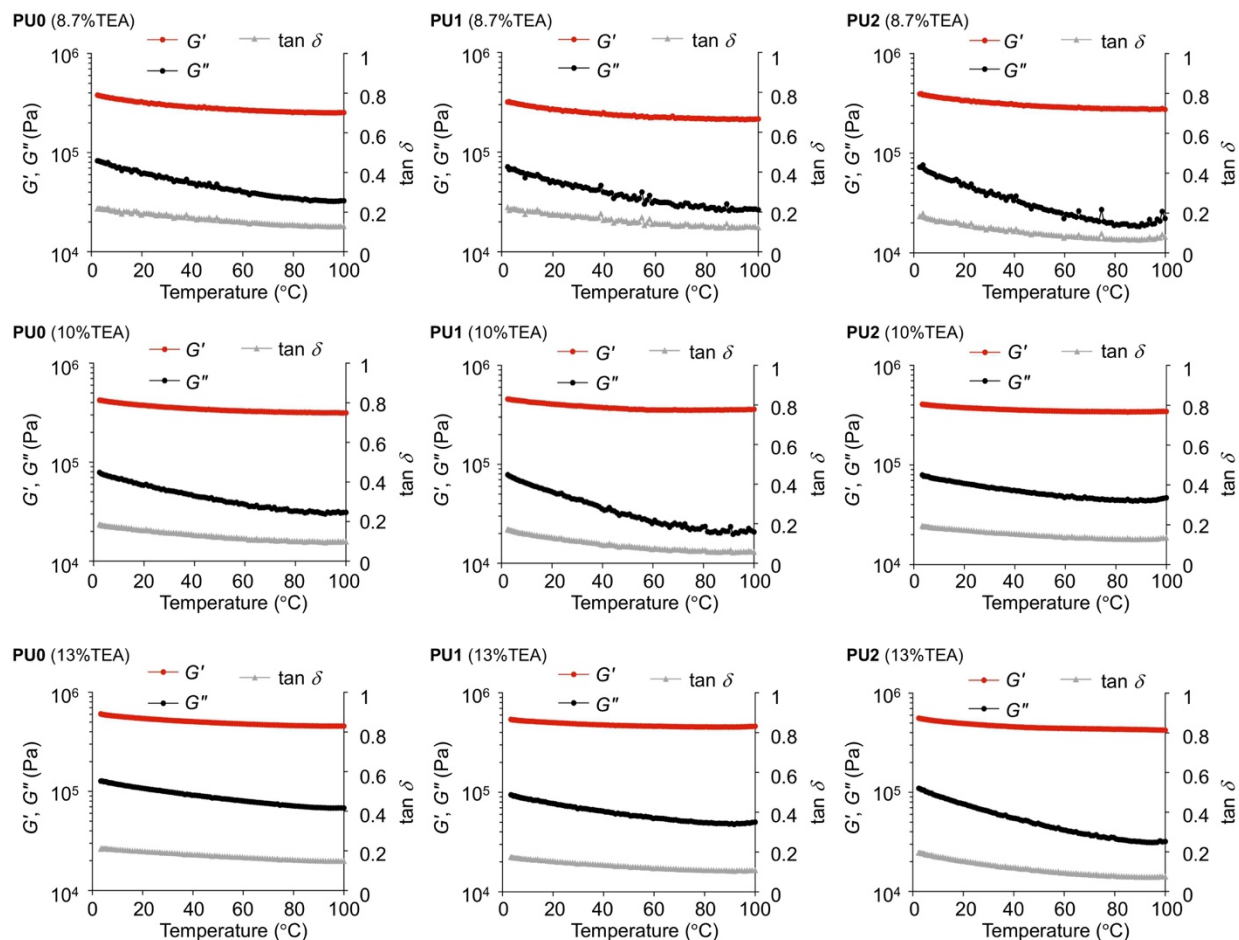


Fig. S26. Dynamic viscoelasticity of the crosslinked PUs.

Table S20. Dynamic viscoelasticity of the PUs at 25 °C.

	G' (Pa) ^a	G'' (Pa) ^b	$\tan \delta$ ^c
PU0 (8.7%TEA)	3.1×10^5	5.9×10^4	0.19
PU1 (8.7%TEA)	2.6×10^5	4.8×10^4	0.18
PU2 (8.7%TEA)	3.3×10^5	4.2×10^4	0.13
PU0 (10%TEA)	3.7×10^5	5.5×10^4	0.15
PU1 (10%TEA)	3.9×10^5	4.8×10^4	0.12
PU2 (10%TEA)	3.7×10^5	6.2×10^4	0.17
PU0 (13%TEA)	5.3×10^5	1.0×10^5	0.19
PU1 (13%TEA)	4.9×10^5	7.3×10^4	0.15
PU2 (13%TEA)	4.8×10^5	7.0×10^4	0.15

^a Storage modulus at 25 °C. ^b Loss modulus at 25 °C. ^c Loss tangent obtained from G''/G' at 25 °C.

With higher crosslinking density (%TEA), the G' values increased significantly. The FLAP dopants in **PU1** and **PU2** did not affect the viscoelasticity of the bulk PU sample.

Mechanical properties of the rubbery polyurethanes (PUs)

Uniaxial tensile tests were carried out on dumbbell-shaped specimens. Rubbery samples were prepared by heating at 60 °C for 1 min with a blow dryer. Nominal stress, σ_N , is defined as f/S_0 , where applied force f is divided by the initial cross-sectional area S_0 (typically 1.5-mm thickness \times 6-mm width).

$$\sigma_N = \frac{f}{S_0}$$

Nominal strain, ε_N , is defined as $\Delta L/L_0$, where sample gauge length (ΔL) is divided by the initial length ($L_0 = 10$ mm).

$$\varepsilon_N = \frac{\Delta L}{L_0}$$

Toughness was calculated as the integrated area under the stress–strain curve.

Young's modulus is defined as the slope of stress–strain curves at 0–10% strain. Tensile velocity was fixed at 100 mm min⁻¹, corresponding to strain rate of 0.17 s⁻¹.

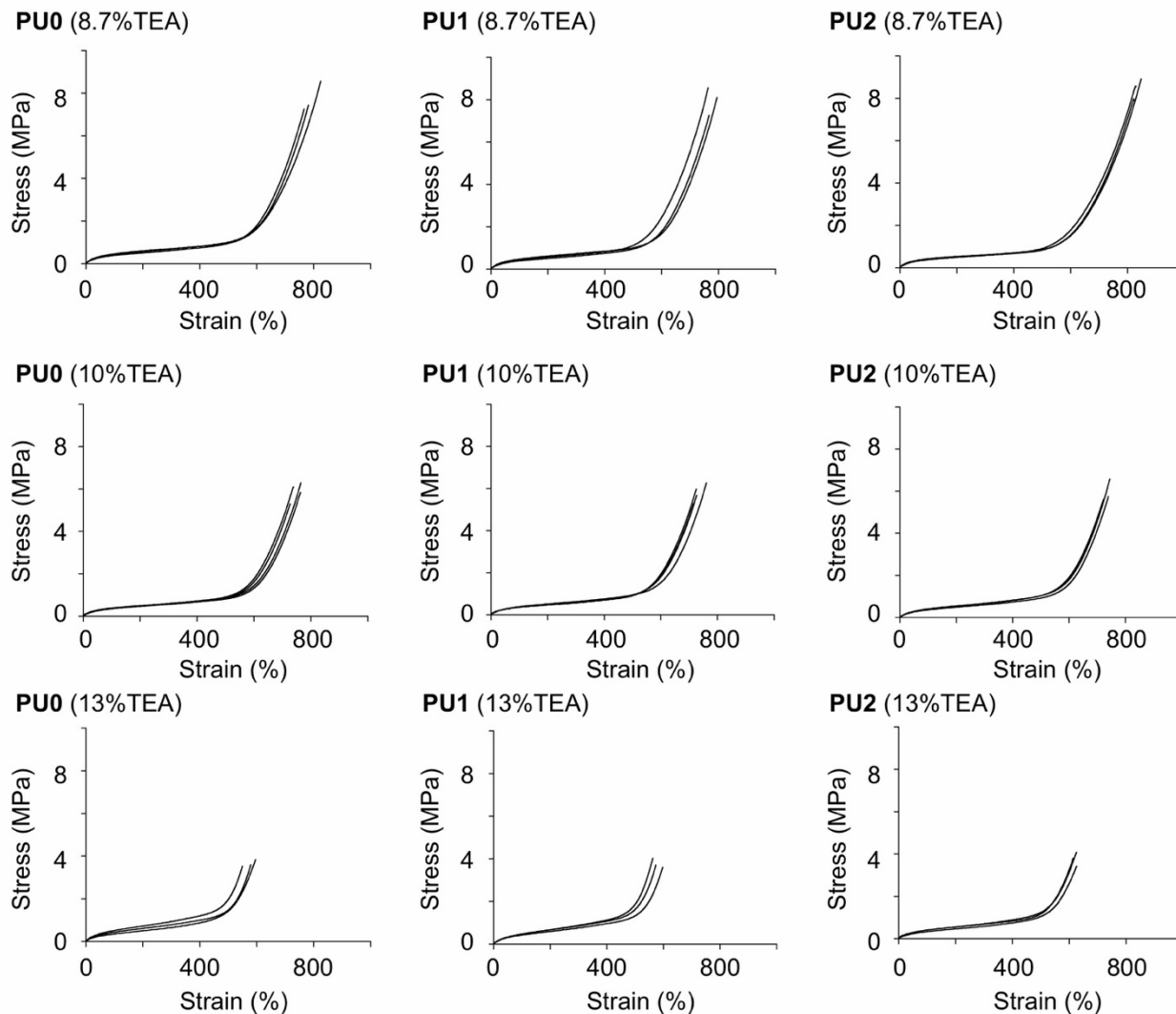


Fig. S27. Stress-strain curves of the rubbery PUs.

Table S21. Mechanical properties of the rubbery PUs in the uniaxial tensile testing.

	Rupture strain (%)	Rupture stress (MPa)	Toughness (MJ m^{-3})	Young's modulus (MPa)
PU0 (8.7%TEA)	801 ± 44	7.2 ± 1.9	12.0 ± 3.3	1.2 ± 0.1
PU1 (8.7%TEA)	791 ± 30	7.8 ± 0.7	12.3 ± 1.2	1.2 ± 0.2
PU2 (8.7%TEA)	824 ± 8	8.2 ± 0.3	12.6 ± 0.5	1.1 ± 0.1
PU0 (10%TEA)	749 ± 19	5.9 ± 0.4	8.7 ± 0.7	1.1 ± 0.1
PU1 (10%TEA)	732 ± 20	5.8 ± 0.4	8.6 ± 0.7	1.0 ± 0.1
PU2 (10%TEA)	733 ± 11	6.0 ± 0.4	9.2 ± 1.0	1.1 ± 0.1
PU0 (13%TEA)	575 ± 24	3.6 ± 0.2	5.4 ± 0.2	1.1 ± 0.1
PU1 (13%TEA)	577 ± 18	3.6 ± 0.4	5.6 ± 0.1	1.1 ± 0.1
PU2 (13%TEA)	616 ± 12	4.0 ± 0.5	5.8 ± 0.6	1.1 ± 0.2

Values of average \pm standard deviation of 3–4 specimen were shown.

Photophysical properties of the unstretched polyurethanes (PUs)

FL spectra in Figs. S28–S33 were recorded on a JASCO Spectrofluorometer FP-8500. The synthesized polyurethane (PU) films become semicrystalline when stored at room temperature (25 °C) for more than 2 days. Therefore, the rubbery samples were prepared by heating at 60 °C for 1 min with a blow dryer. While mechanical properties were largely dependent on the crystallinity (Fig. S39), FL spectra, FL quantum yields, and FL lifetimes of the unstretched PU films showed small differences (Table S22, Figs. S28–33). No excimer formation was observed in these conditions.

Table S22. Photophysical constants of semicrystalline and rubbery PU films with each crosslinking density (%TEA). $\lambda_{\text{ex}} = 365$ nm.

	Φ_{FL}	τ_{FL} (ns) ^a	k_{r} (s ⁻¹)	k_{nr} (s ⁻¹)
semicrystalline PU1 (8.7%TEA)	0.30	6.8	4.4×10^7	1.0×10^8
rubbery PU1 (8.7%TEA)	0.26	6.9	3.8×10^7	1.1×10^8
semicrystalline PU1 (10%TEA)	0.30	6.7	4.4×10^7	1.0×10^8
rubbery PU1 (10%TEA)	0.28	6.9	4.0×10^7	1.0×10^8
semicrystalline PU1 (13%TEA)	0.33	6.9	4.8×10^7	1.0×10^8
rubbery PU1 (13%TEA)	0.31	7.1	4.3×10^7	1.0×10^8
semicrystalline PU2 (8.7%TEA)	0.35	6.8	5.1×10^7	1.0×10^8
rubbery PU2 (8.7%TEA)	0.37	7.0	3.8×10^7	0.9×10^8
semicrystalline PU2 (10%TEA)	0.35	6.7	5.2×10^7	1.0×10^8
rubbery PU2 (10%TEA)	0.35	7.1	5.0×10^7	0.9×10^8
semicrystalline PU2 (13%TEA)	0.33	7.0	4.6×10^7	1.0×10^8
rubbery PU2 (13%TEA)	0.33	6.9	4.8×10^7	1.0×10^8

^a $\lambda_{\text{em}} = 470$ nm.

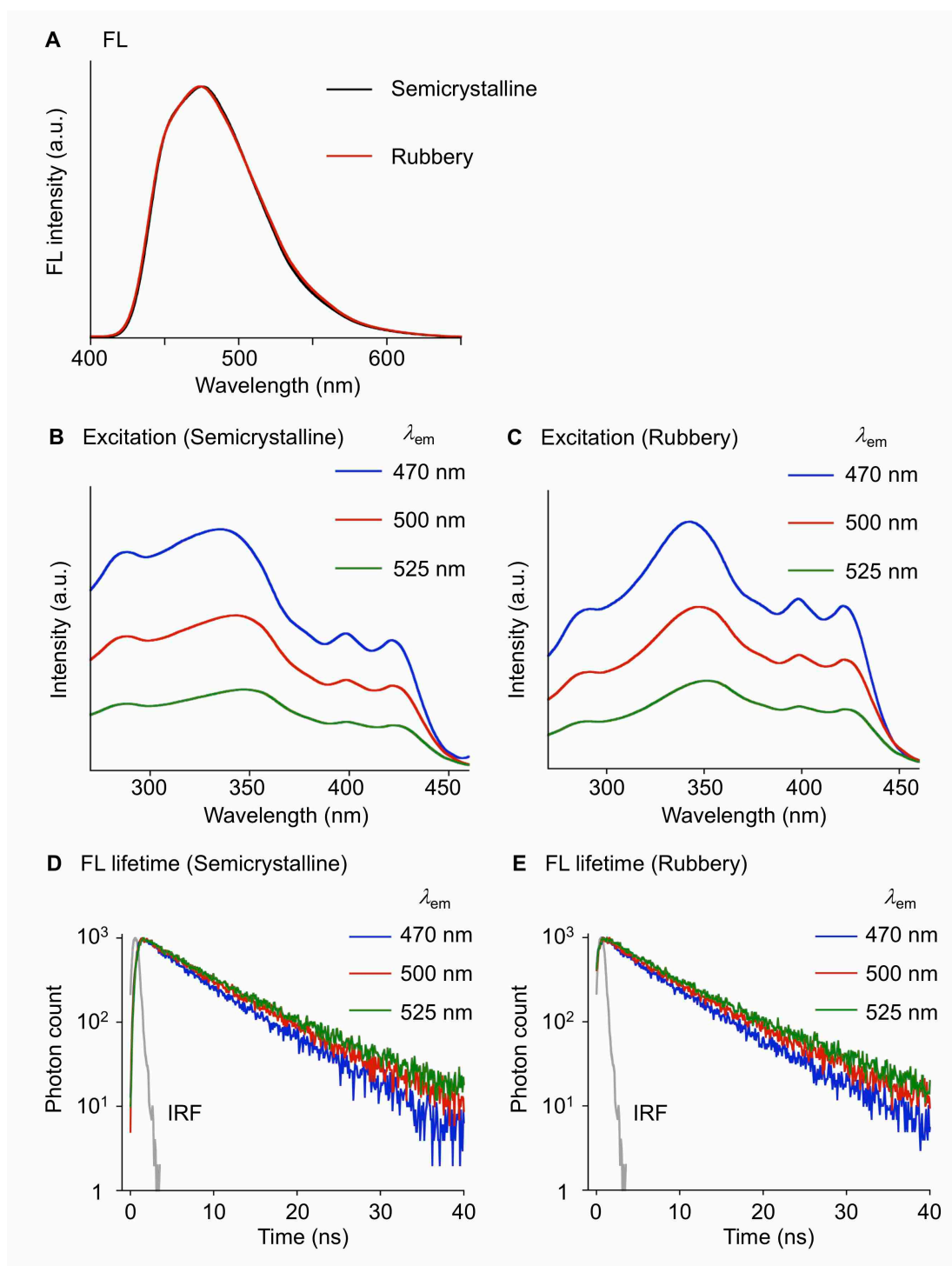


Fig. S28. Photophysical properties of semicrystalline and rubbery **PU1** films (8.7%TEA). **(A)** FL spectra ($\lambda_{ex} = 365$ nm), **(B, C)** excitation spectra, and **(D, E)** FL decay profiles.

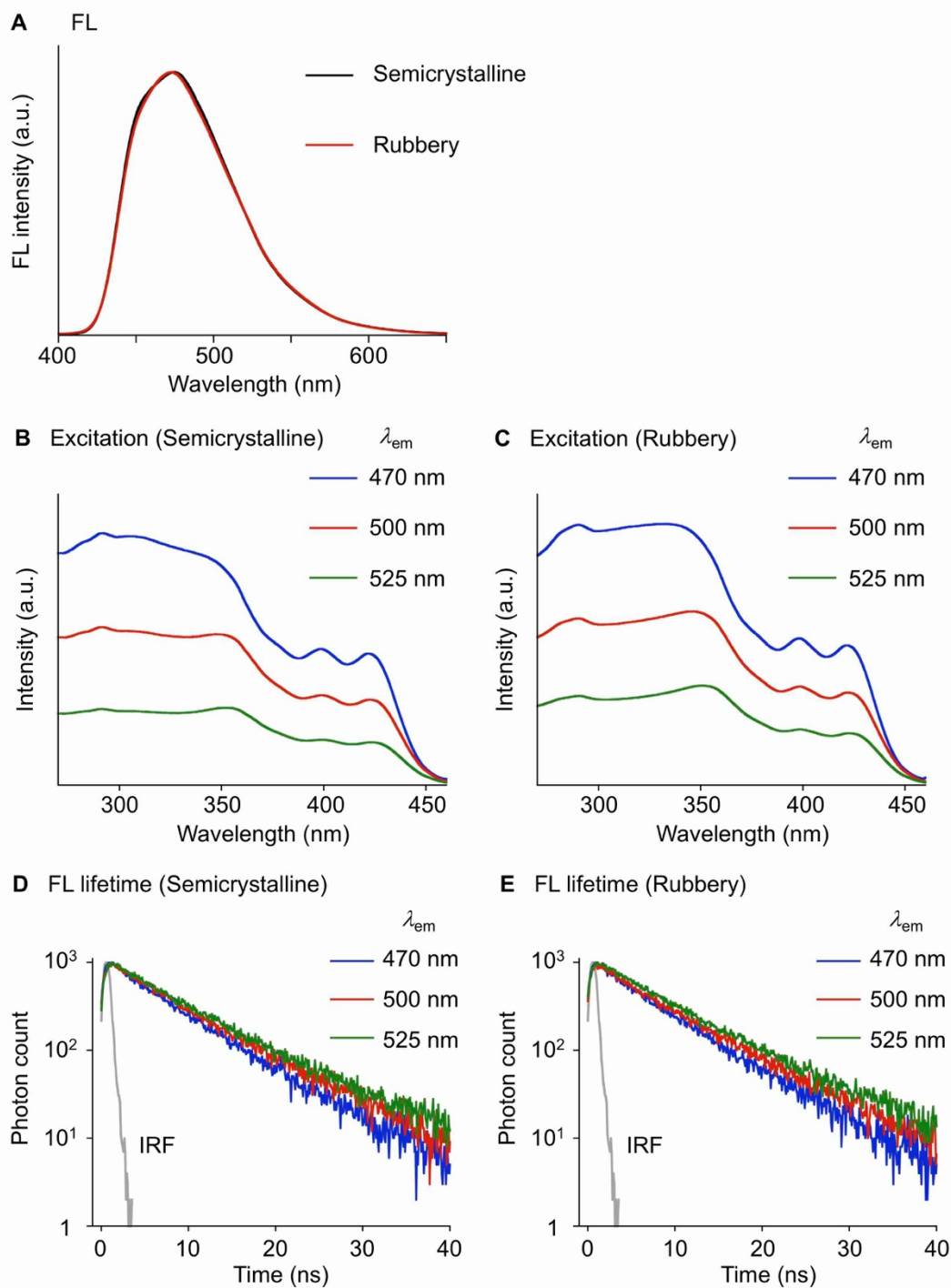


Fig. S29. Photophysical properties of semicrystalline and rubbery **PU1** films (10%TEA). **(A)** FL spectra ($\lambda_{\text{ex}} = 365$ nm), **(B, C)** excitation spectra, and **(D, E)** FL decay profiles.

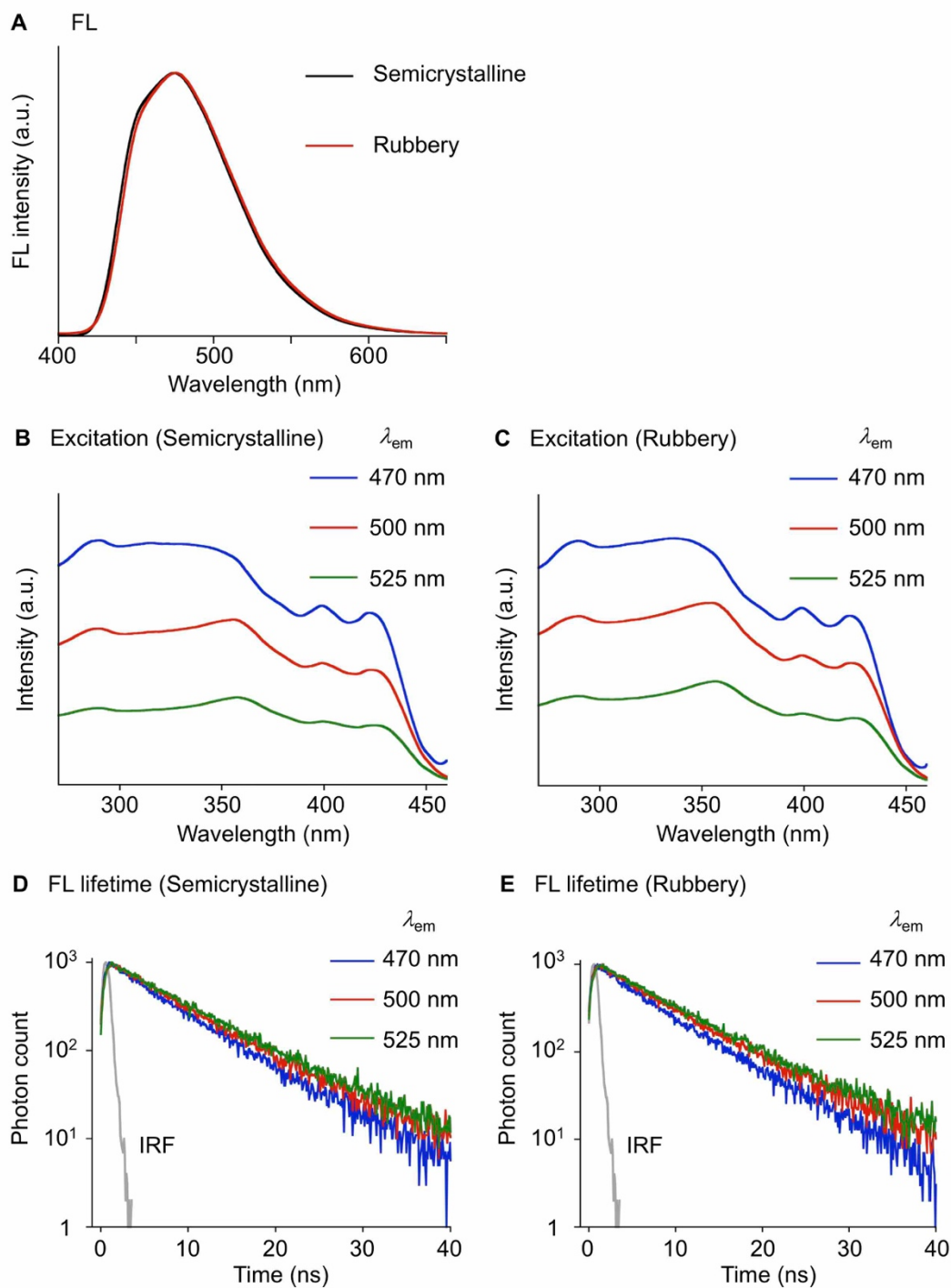


Fig. S30. Photophysical properties of semicrystalline and rubbery PU1 films (13%TEA). (A) FL spectra ($\lambda_{ex} = 365$ nm), (B, C) excitation spectra, and (D, E) FL decay profiles.

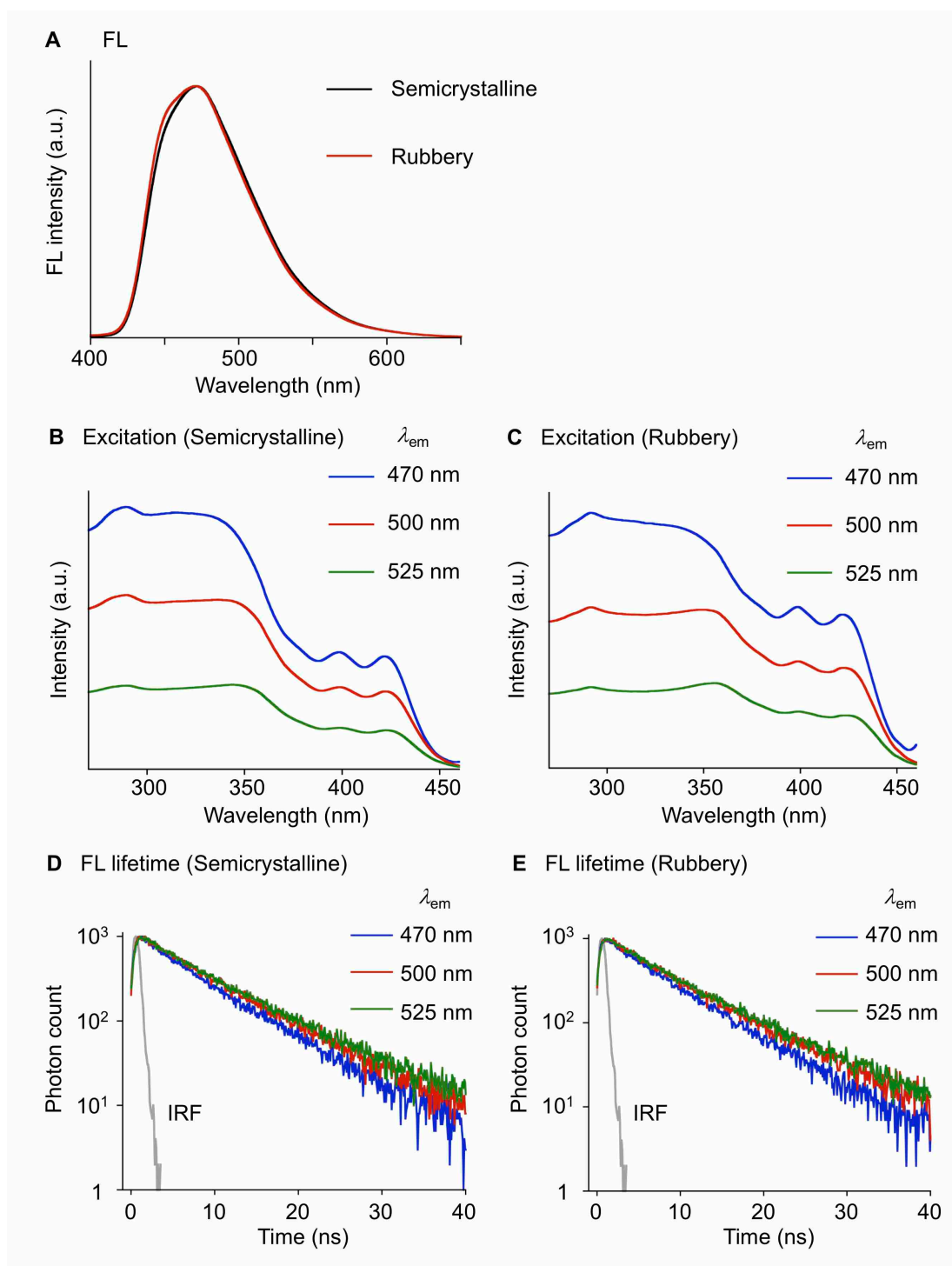


Fig. S31. Photophysical properties of semicrystalline and rubbery **PU2** films (8.7%TEA). **(A)** FL spectra ($\lambda_{\text{ex}} = 365$ nm), **(B, C)** excitation spectra, and **(D, E)** FL decay profiles.

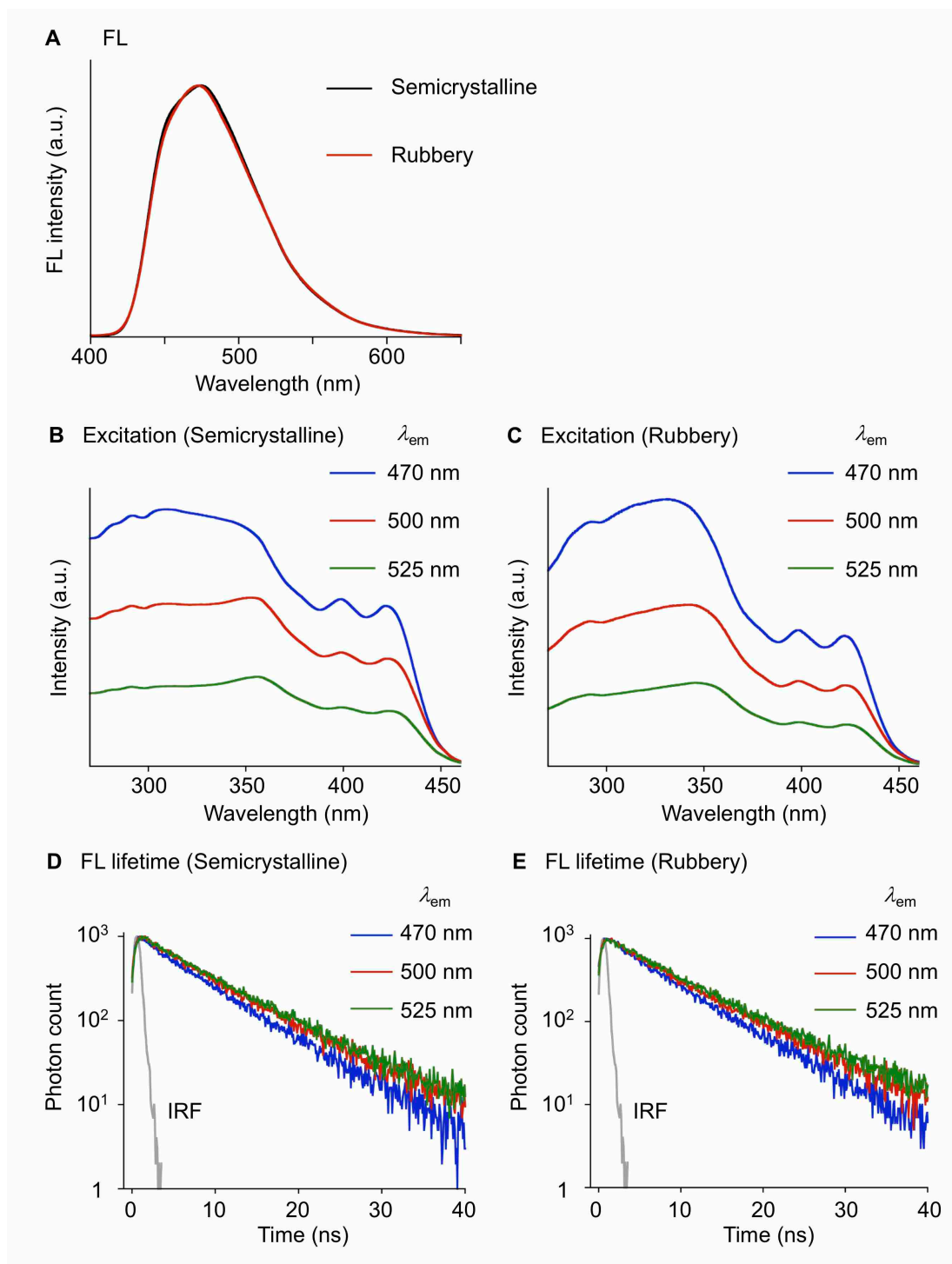


Fig. S32. Photophysical properties of semicrystalline and rubbery **PU2** films (10%TEA). **(A)** FL spectra ($\lambda_{\text{ex}} = 365$ nm), **(B, C)** excitation spectra, and **(D, E)** FL decay profiles.

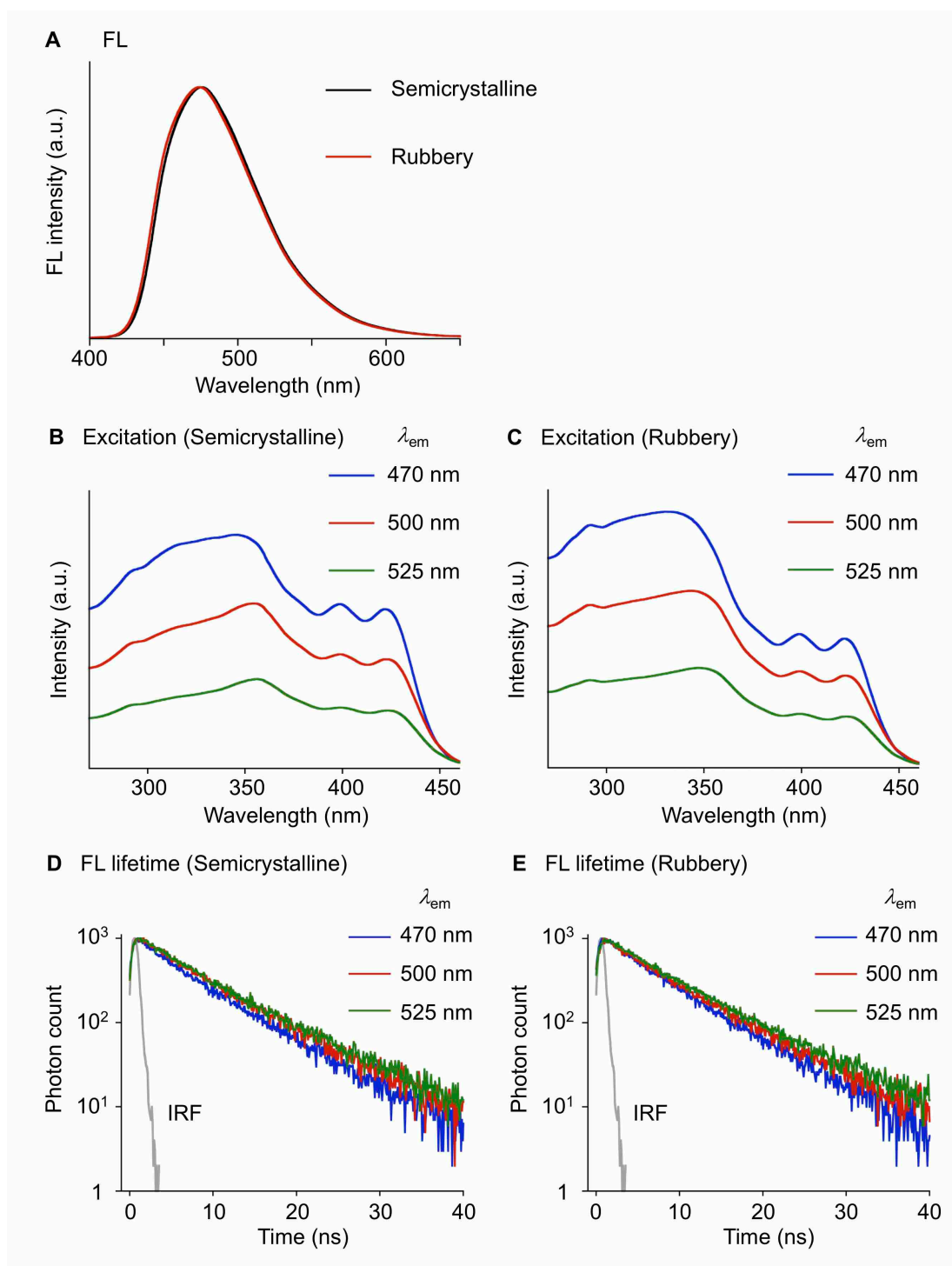


Fig. S33. Photophysical properties of semicrystalline and rubbery **PU2** films (13%TEA). **(A)** FL spectra ($\lambda_{\text{ex}} = 365$ nm), **(B, C)** excitation spectra, and **(D, E)** FL decay profiles.

Real-time monitoring of the FL and absorption spectra of the stretched PUs

During the tensile testing, time-dependent FL and absorption spectra were monitored using a multi-channel photodetector (Otsuka Electronics, MCPD-6800) equipped with an optical fiber. The FL spectra were recorded with 0.8-s exposure time and 2 accumulations (at 1.6-s intervals), in which a 365-nm LED was used for excitation. Absorption spectra were recorded on the same photodetecting system with a 1.6-s exposure time and 2 accumulations (at 3.2-s intervals). Before the tensile testing, reference absorption spectrum $I_0(\lambda)$ was measured with a 100-W tungsten light source fixed at a constant distance from the optical fiber head. Then, a PU specimen was set (and stretched) so that the specimen crossed the optical path to acquire absorption spectrum $I(\lambda)$. Absorbance A at each wavelength was obtained from $I_0(\lambda)$ and $I(\lambda)$ as below.

$$A = -\log\left(\frac{I}{I_0}\right)$$

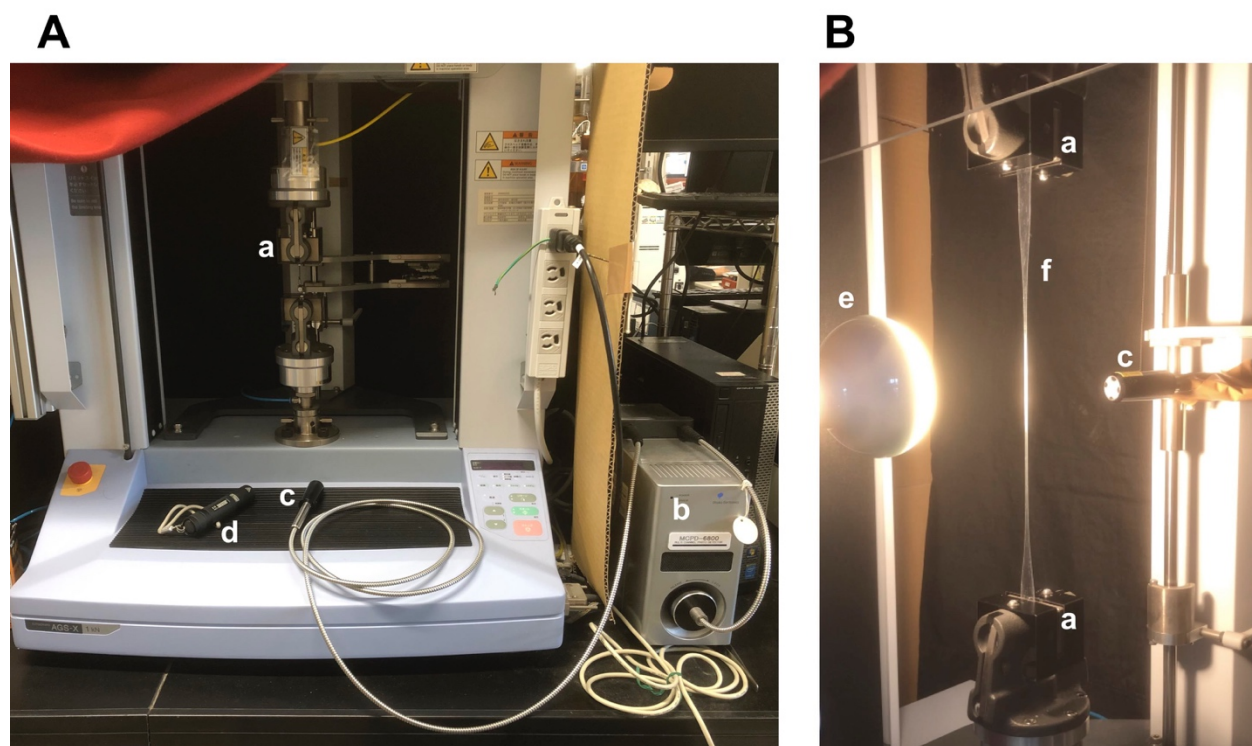


Fig. S34. Experimental setup for the real-time collection of (A) FL spectra and (B) absorption spectra of the stretched PU films.

- a:** Upper and lower grips of a tensile testing machine to hold a specimen.
- b:** Multi-channel photodetector.
- c:** Optical fiber head connected to **b**.
- d:** 365-nm LED (NICHIA, JAXMAN U1).
- e:** 100-W tungsten light (METRO).
- f:** PU specimen.

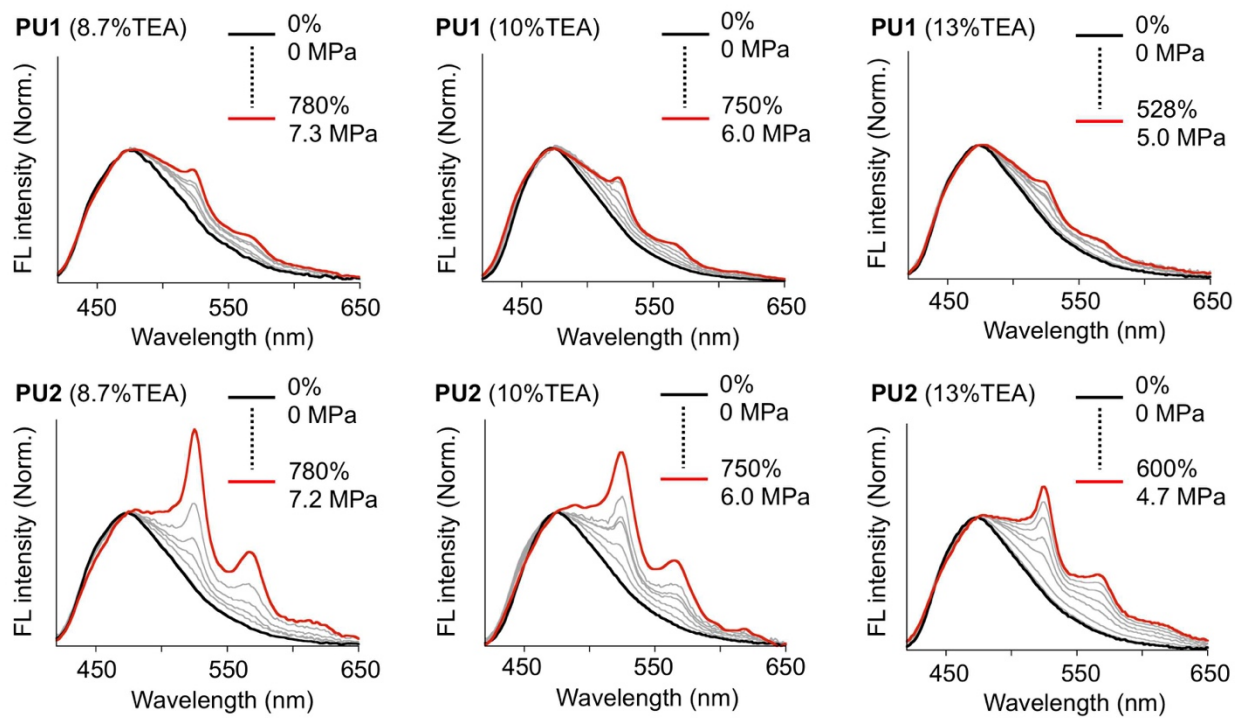


Fig. S35. FL spectral changes of the rubbery PUs. Normalized at 474 nm. $\lambda_{\text{ex}} = 365$ nm.

Loading–unloading cycle testing

To confirm the rapid reversibility of the stress-induced FL response, the loading and unloading cycle testing of **PU2** (10%TEA) was performed with ratiometric FL analysis (Fig. 4F in the main text). Fig. S36 shows mechanical profiles in the cycle test.

Start → **a**: Loading up to 300% strain (purple line).

a → **b**: Unloading up to stress of 0.1 MPa (blue line).

b → **c**: Loading up to 600% strain (green line).

c → **d**: Unloading up to stress of 0.1 MPa (orange line).

d → **e**: Loading up to rupture (red line).

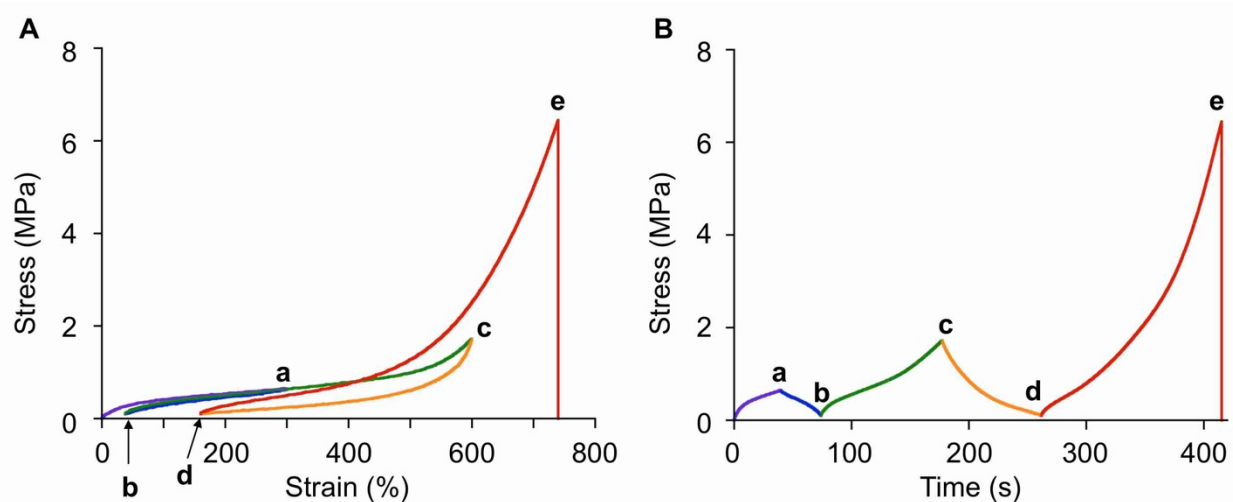


Fig. S36. Stress profile as a function of (A) strain and (B) time for the cycle testing.

Estimation of the stressed FLAP probe (%)

Percentage of the stressed FLAP probe over the FL switching threshold was estimated from the ratiometric FL analysis of the stretched PU films (Fig. 5 in the main text).

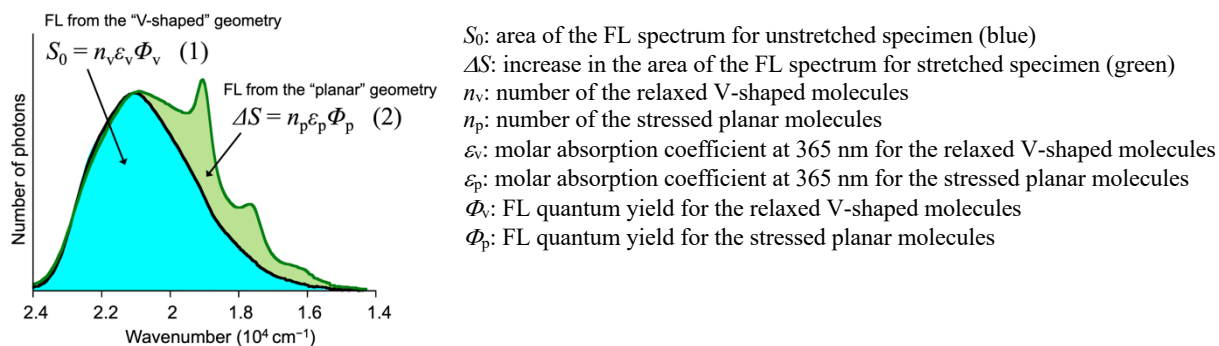


Fig. S37. Optical parameters for the estimation.

For the estimation, it was assumed that the FL emission was observed mainly from two types of independent species bearing the bent and planar geometries. Considering (1) and (2) in Fig. S37, the proportion of the stressed planar FLAP molecules can be expressed as follows,

$$\frac{n_p}{n_p + n_v} = \frac{1}{1 + \frac{n_v}{n_p}} = \frac{1}{1 + \frac{\epsilon_p \Phi_p \cdot S_0}{\epsilon_v \Phi_v \cdot \Delta S}} \quad (3)$$

Here, molar absorption coefficients were roughly estimated as $\epsilon_p = 140000 \text{ M}^{-1} \text{ cm}^{-1}$ for the planar geometry and $\epsilon_v = 70000 \text{ M}^{-1} \text{ cm}^{-1}$ for the bent geometry, considering TD-DFT calculation results at the TD PBE0/6-31+G(d) level of theory. The FL quantum yields of the independent planar and bent species were assumed to be comparable ($\Phi_v \approx \Phi_p$), because Φ_v was determined to be about 0.3 from the FL analysis of unstretched PU polymers with the FLAP dopant (Table S22), and Φ_p was referenced from the FL quantum yield (about 0.3) of the parent FLAP compounds in solution (Table S1).

Control experiments: Physical doping of FLAP into the polyurethane (PU)

PU3 was synthesized in the same procedure as **PU1** (10%TEA), in which **FLAP1** was replaced by **FLAP3** (31). **FLAP3** is not covalently connected to the polymer chain network of **PU3**, but simply dispersed inside **PU3**. Without extension, mechanical and photophysical properties of the **PU3** film are almost the same as those of **PU1** and **PU2**. On the other hand, no characteristic FL response was observed under the tensile testing, clearly indicating that the conformational planarization of the FLAP dopant cannot be induced without covalent connection between the FLAP molecule and the polymer chains.

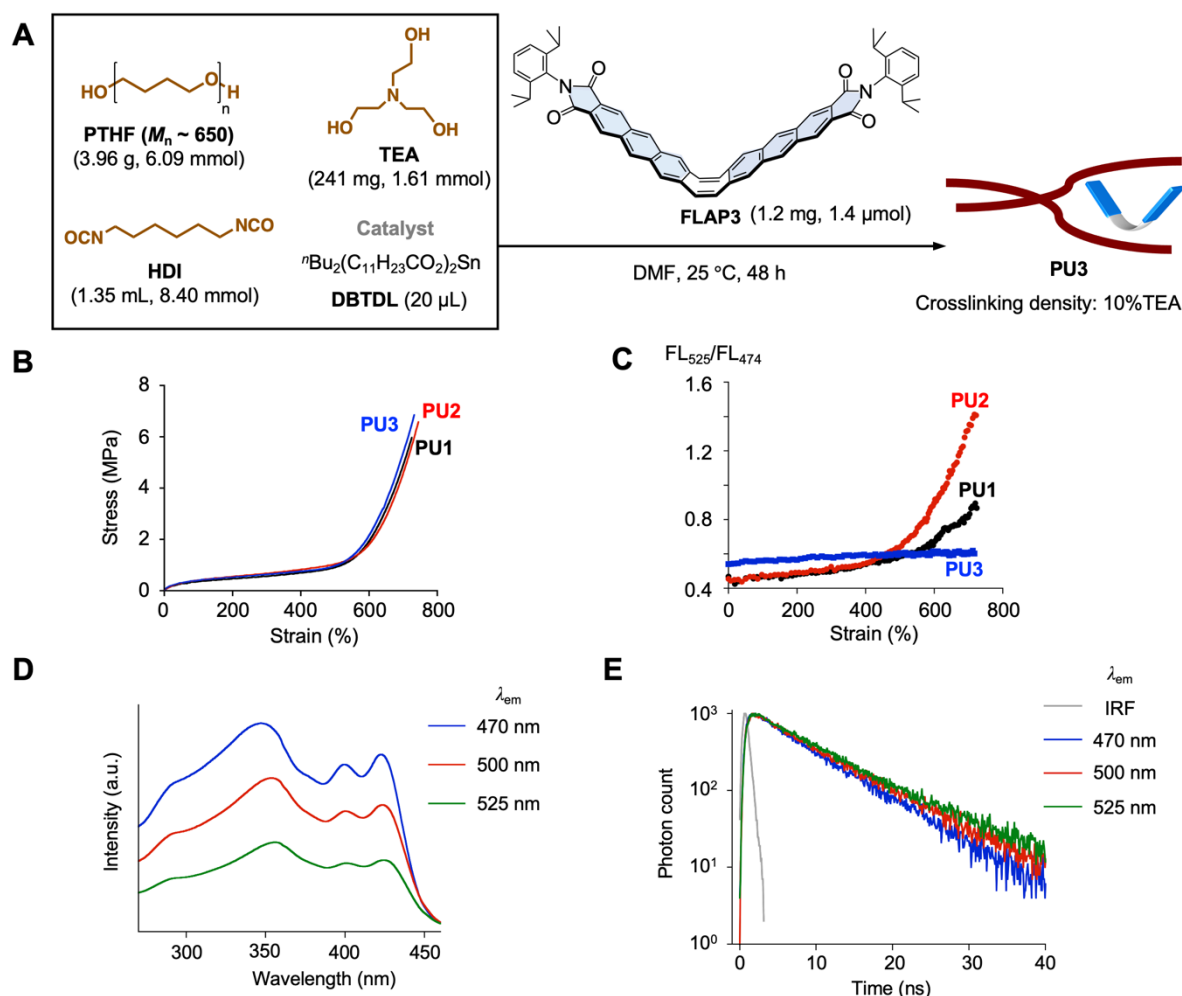


Fig. S38. (A) Synthesis of **PU3** (10%TEA). (B) Stress-strain curves of **PU1–PU3** (10%TEA). Strain rate: 0.17 s^{-1} . (C) FL ratiometric analysis of the stretched **PU1–PU3** films. (D) Excitation spectra of the unstretched **PU3** film. (E) FL lifetime profiles of the unstretched **PU3** film.

Table S23. Photophysical constants of the rubbery **PU3** films. $\lambda_{\text{ex}} = 365$ nm.

Φ_{FL}	τ_{FL} (ns) ^a	k_{r} (s^{-1})	k_{nr} (s^{-1})
0.30	7.1	4.2×10^7	1.0×10^8

^a $\lambda_{\text{em}} = 470$ nm. These values were comparable those of **PU1** and **PU2** in Table S22.

Semicrystalline polyurethanes (PUs)

Mechanical and photophysical properties of the semicrystalline PU samples, stored at room temperature (25 °C) for more than 2 days, were evaluated in the same protocols as the rubbery PU samples. Young's modulus is more than 10 times higher than that of the rubbery PU (Table S24). Accordingly, yield point at the early stage of the strain became more pronounced for the semicrystalline samples (Fig. S39), followed by typical necking behavior (Fig. S40). Since the necking occurs in a specific position, acquired FL spectra depend on the UV-irradiated area. Rupture strain significantly decreased in the sample with the higher crosslinking density (Table S24).

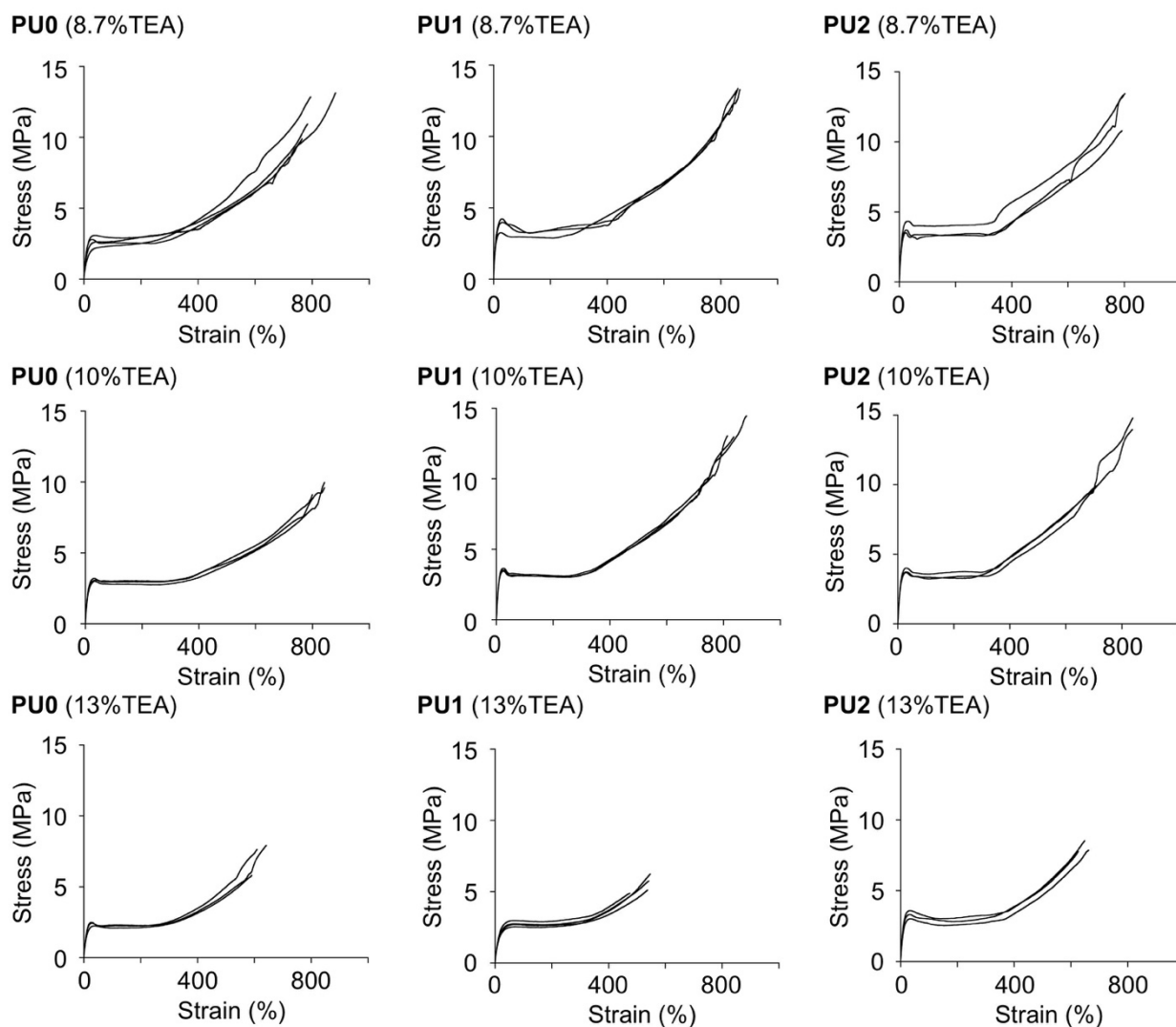


Fig. S39. Stress-strain curves of the semicrystalline PUs.

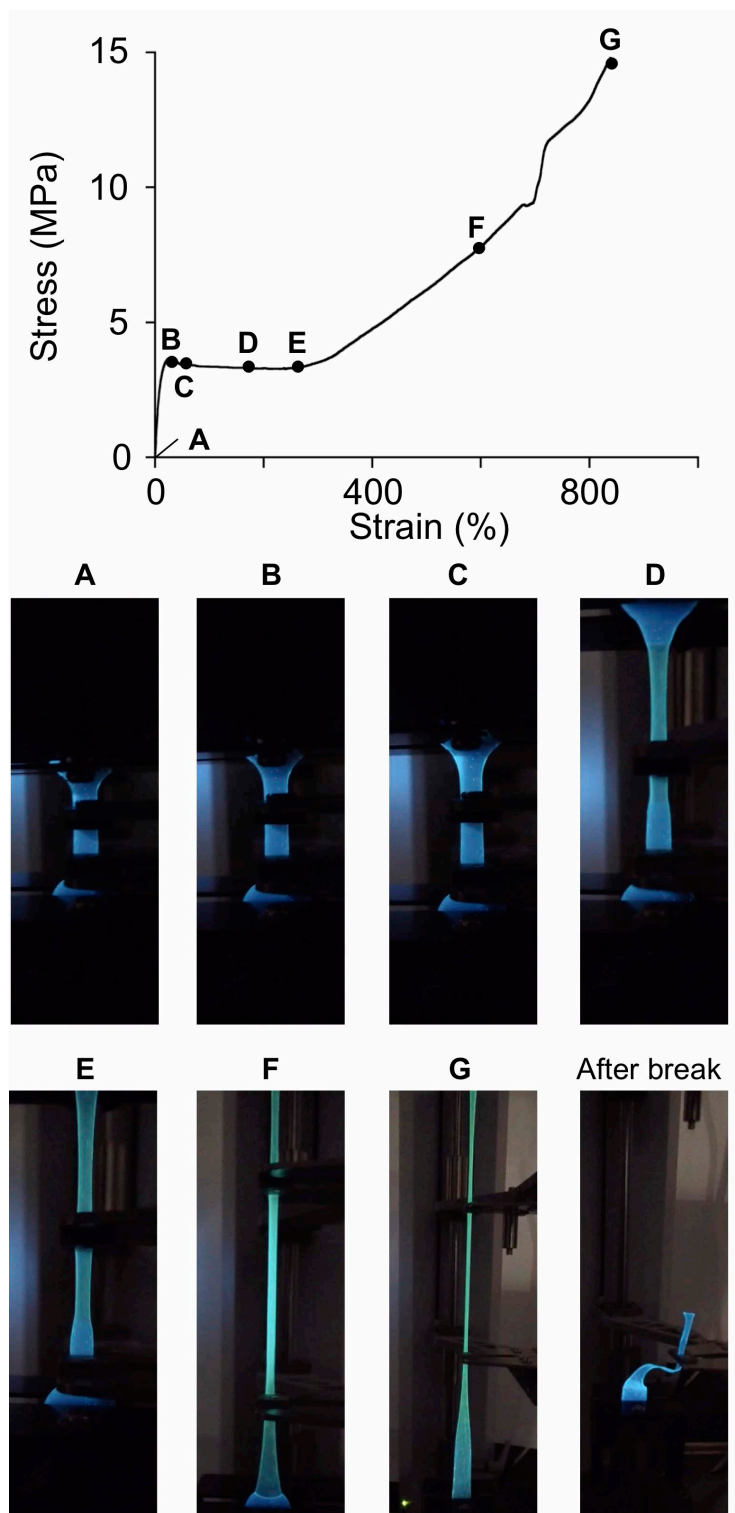


Fig. S40. A typical example of the stress-strain curve and the corresponding photographs of the stretched fluorescent specimen, in which the semicrystalline **PU2** (10%TEA) was applied to the tensile testing.

Table S24. Mechanical properties of the semicrystalline PUs in the uniaxial tensile testing.

	Rupture strain (%)	Rupture stress (MPa)	Toughness (MJ m ⁻³)	Young's modulus (MPa)
PU0 (8.7%TEA)	807 ± 52	11.7 ± 1.6	40.1 ± 5.3	18 ± 4
PU1 (8.7%TEA)	862 ± 5	13.3 ± 0.1	48.9 ± 0.9	30 ± 2
PU2 (8.7%TEA)	797 ± 5	12.5 ± 1.5	46.0 ± 5.0	30 ± 3
PU0 (10%TEA)	829 ± 25	9.6 ± 0.4	36.5 ± 1.4	22 ± 1
PU1 (10%TEA)	844 ± 34	13.5 ± 0.8	47.7 ± 4.0	28 ± 1
PU2 (10%TEA)	797 ± 72	12.9 ± 2.6	46.6 ± 8.5	28 ± 2
PU0 (13%TEA)	614 ± 26	7.1 ± 1.1	19.9 ± 2.4	17 ± 2
PU1 (13%TEA)	525 ± 34	5.5 ± 0.6	16.7 ± 1.1	15 ± 1
PU2 (13%TEA)	645 ± 18	8.1 ± 0.4	25.7 ± 1.8	24 ± 3

Average ± standard deviation of 3–4 specimens was shown.

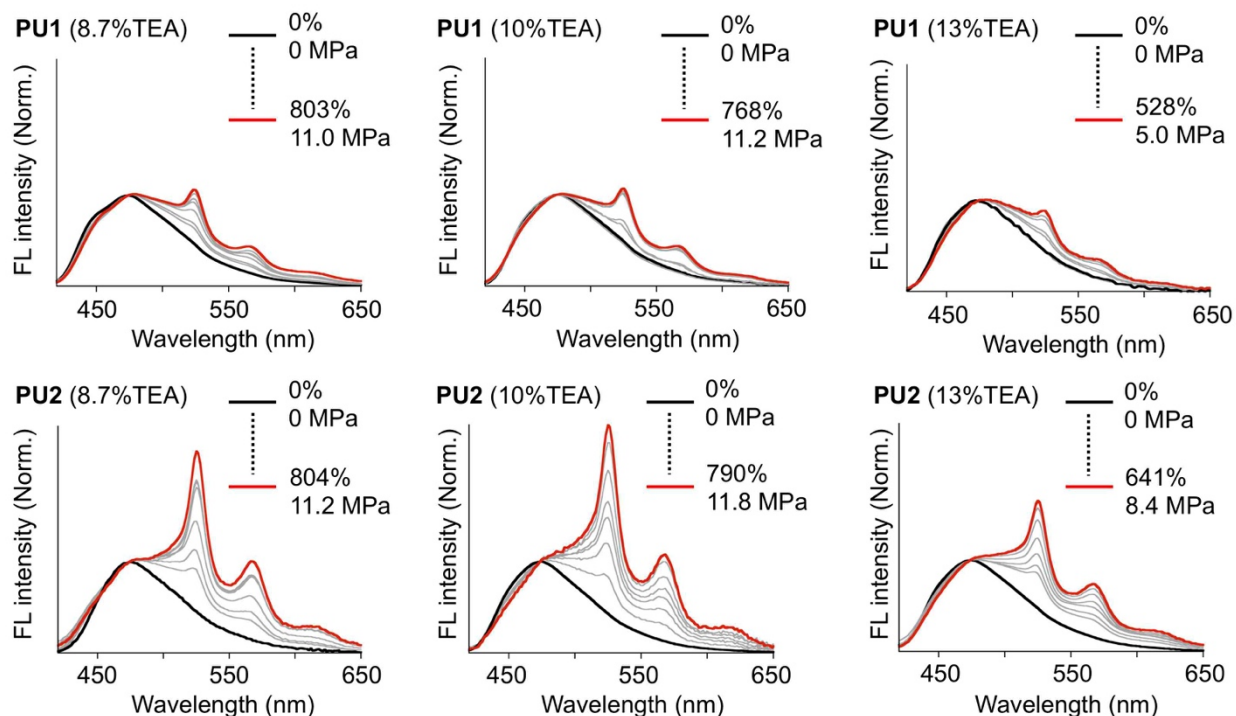


Fig. S41. FL spectral changes of the semicrystalline PUs. Normalized at 474 nm. $\lambda_{ex} = 365$ nm.

NMR spectra of new compounds

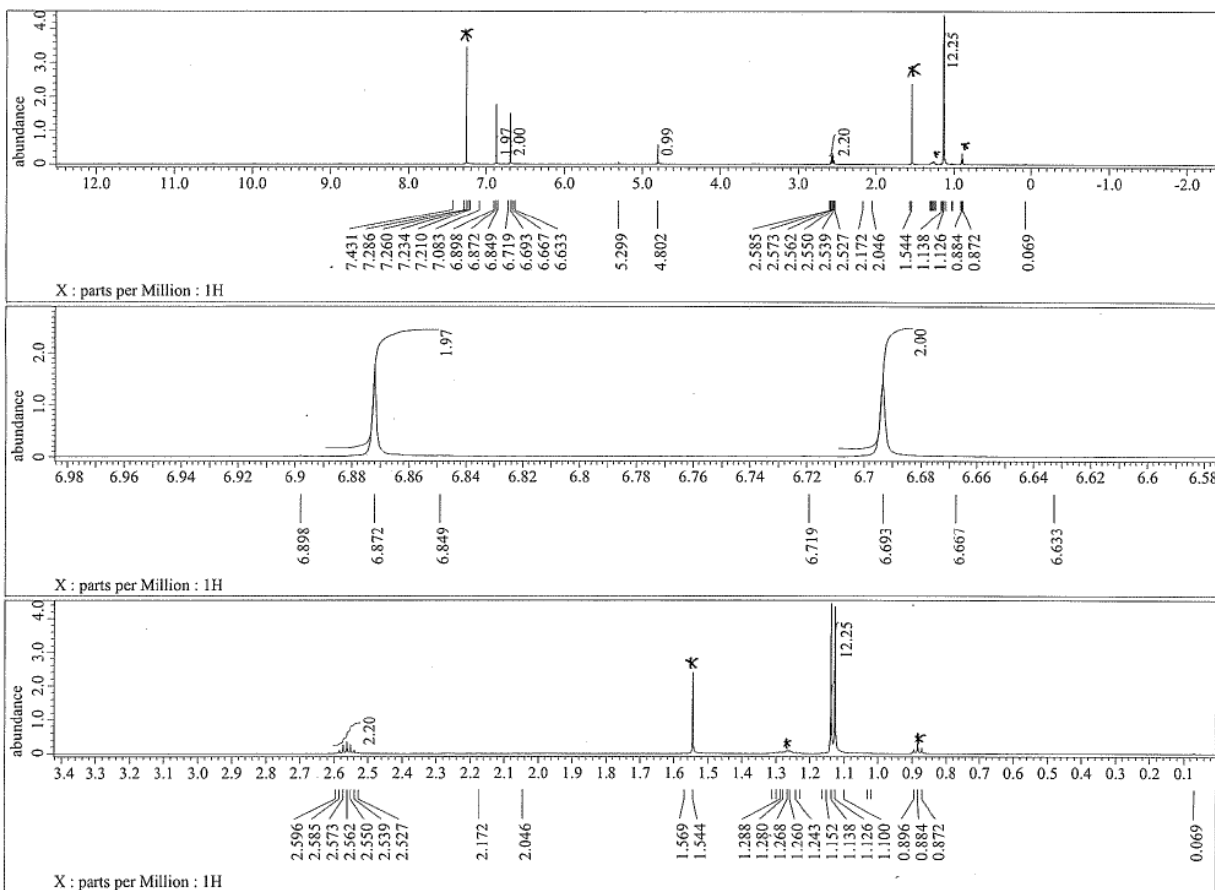


Fig. S42. ^1H NMR spectra of S1 in CDCl_3 at 25°C . The peaks marked with * indicate residual solvents.

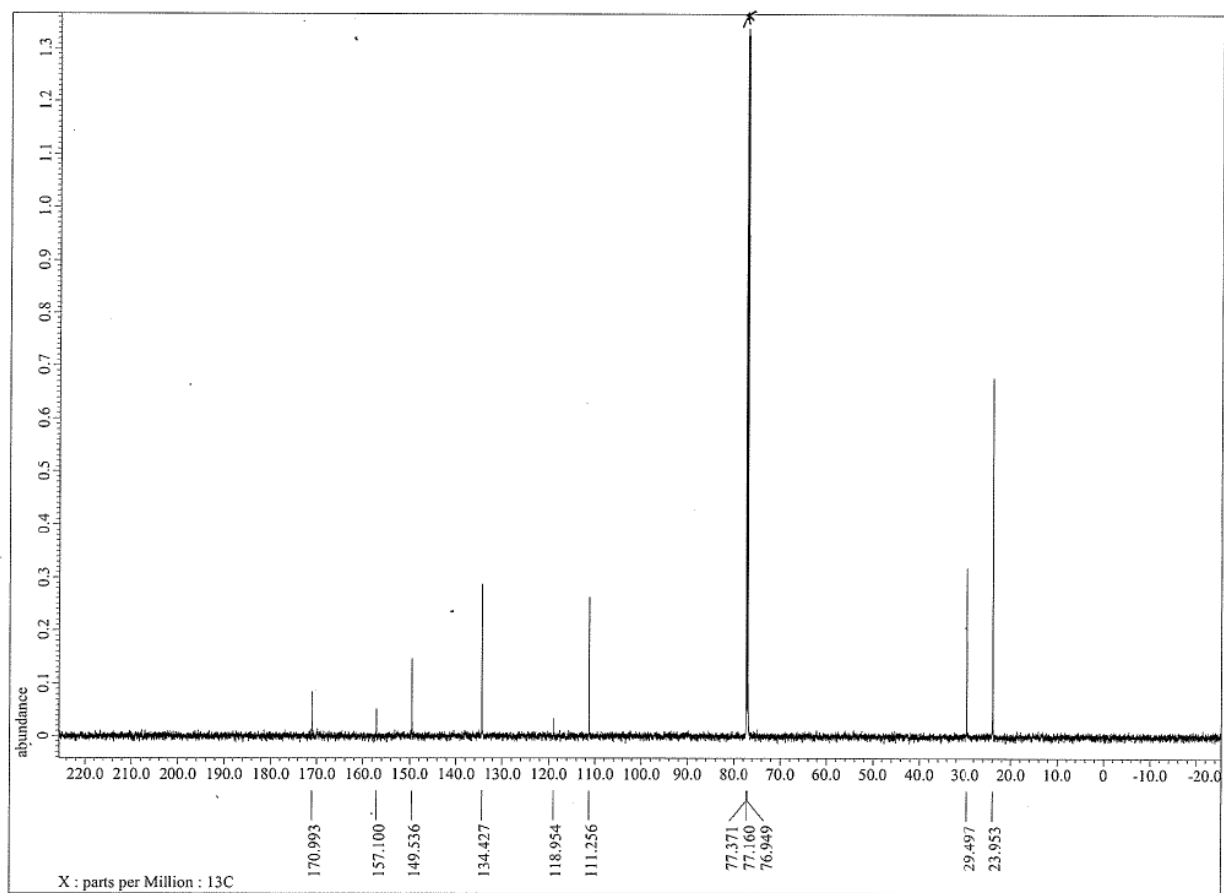


Fig. S43. ^{13}C NMR spectrum of **S1** in CDCl_3 at 25 °C. The peak marked with * indicates residual solvents.

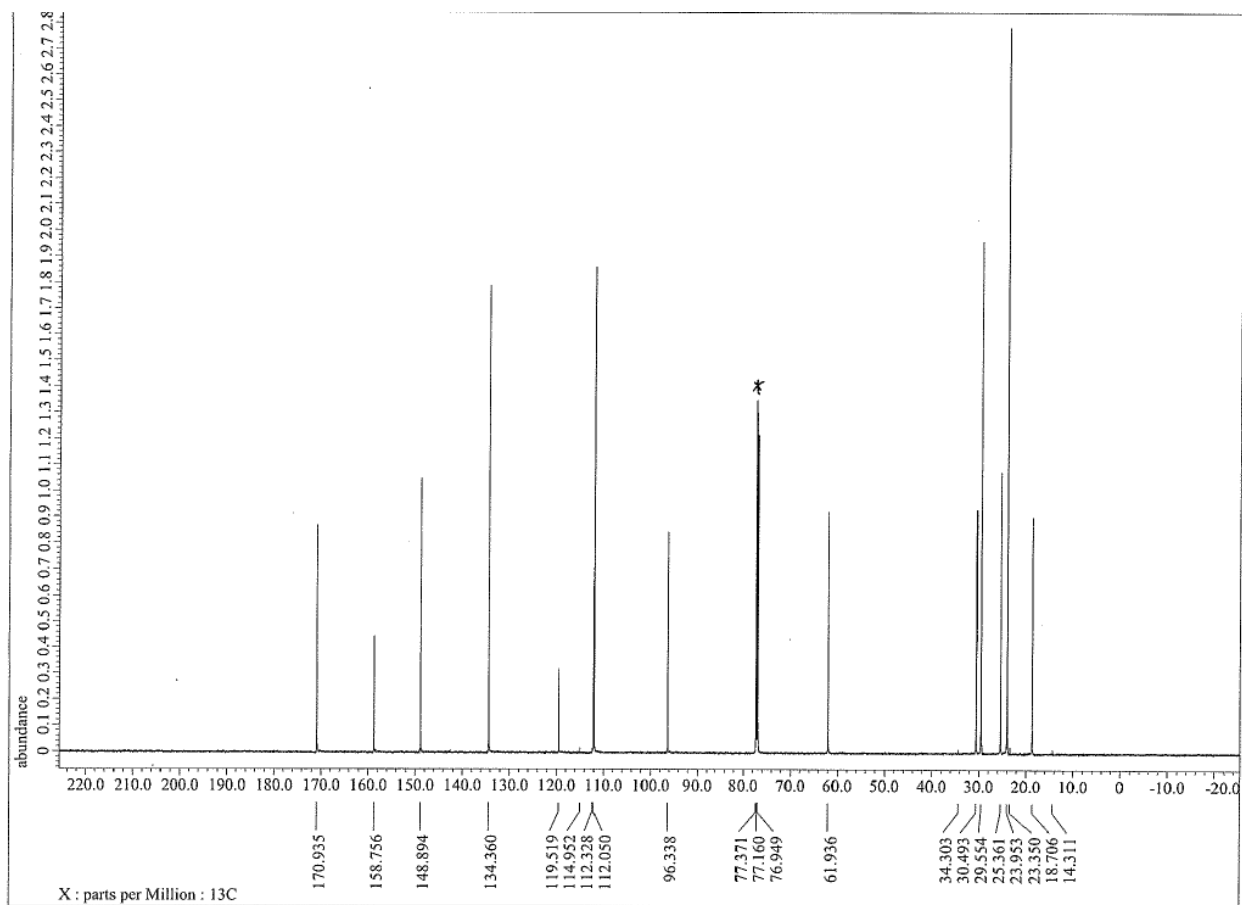


Fig. S45. ^{13}C NMR spectrum of **S2** in CDCl_3 at 25 °C. The peak marked with * indicates residual solvents.

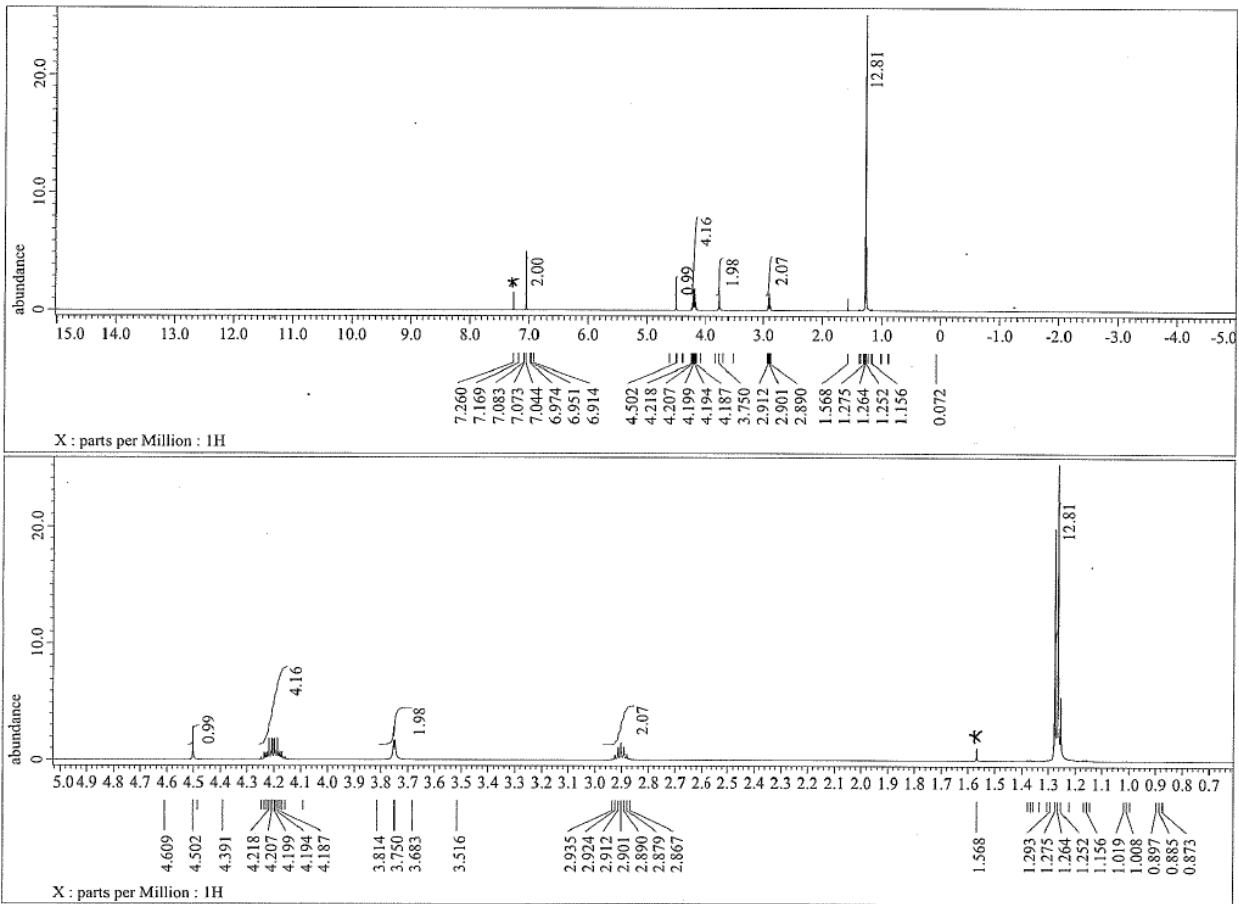


Fig. S46. ^1H NMR spectra of S3 in CDCl_3 at 25°C . The peaks marked with * indicate residual solvents.

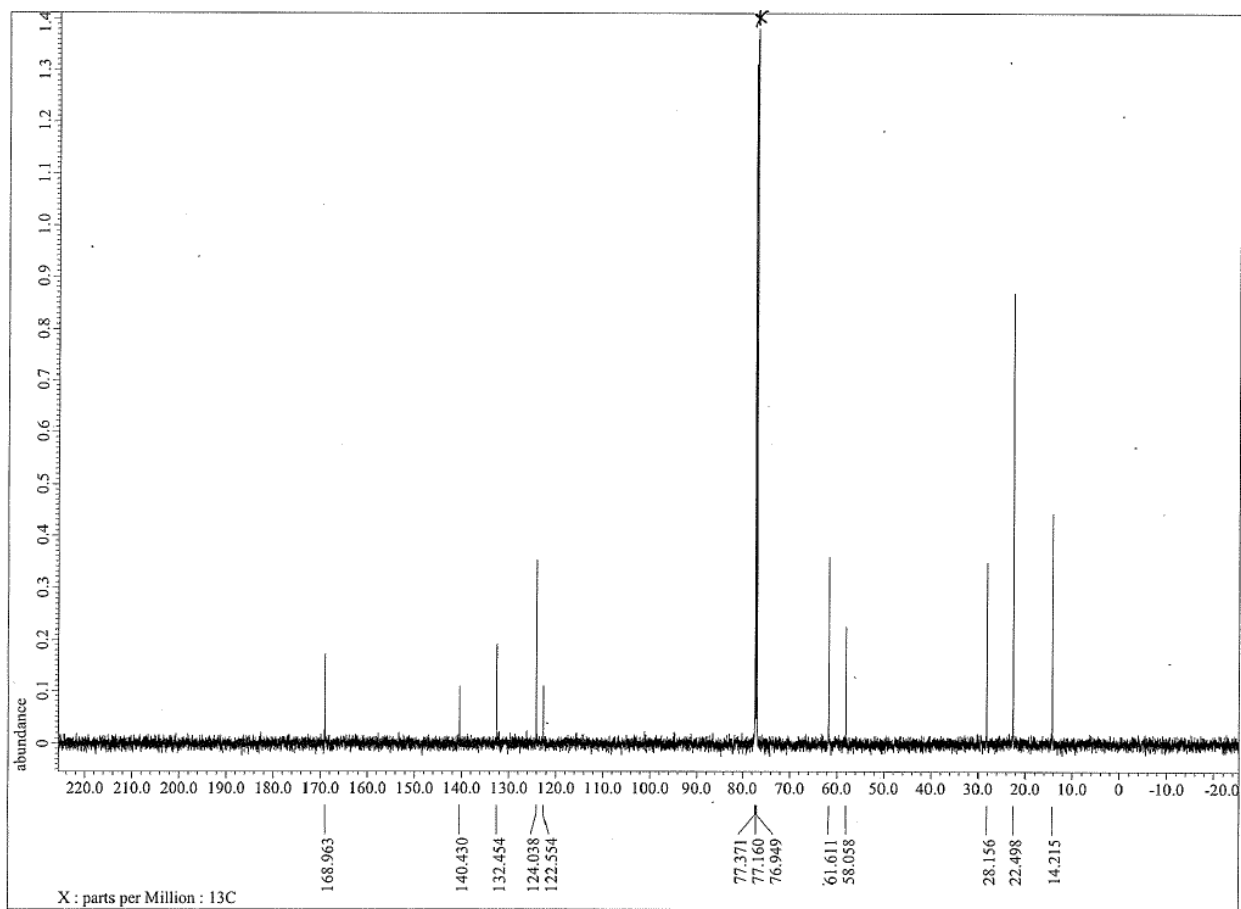


Fig. S47. ^{13}C NMR spectrum of **S3** in CDCl_3 at $25\text{ }^\circ\text{C}$. The peak marked with * indicates residual solvents.

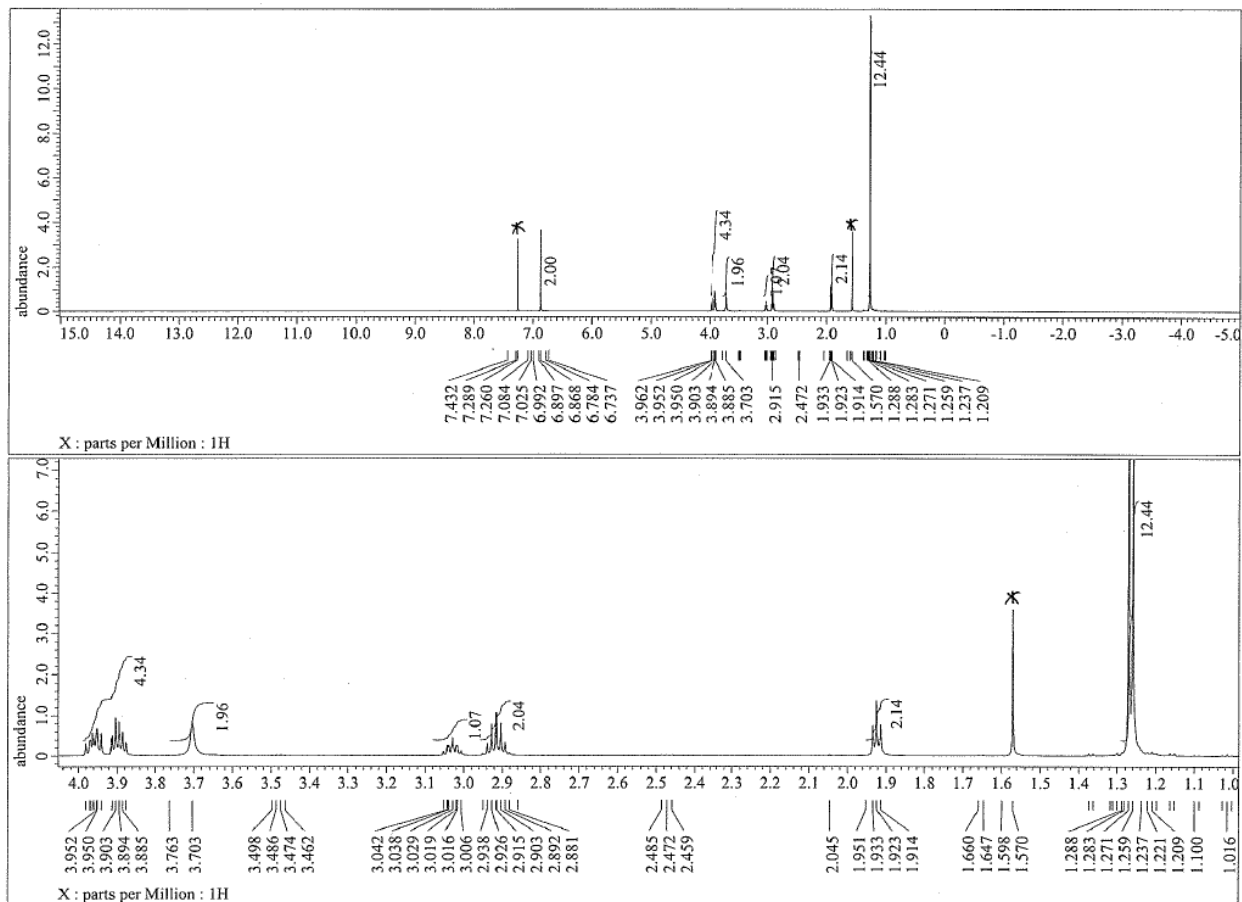


Fig. S48. ¹H NMR spectra of S4 in CDCl₃ at 25 °C. The peaks marked with * indicate residual solvents.

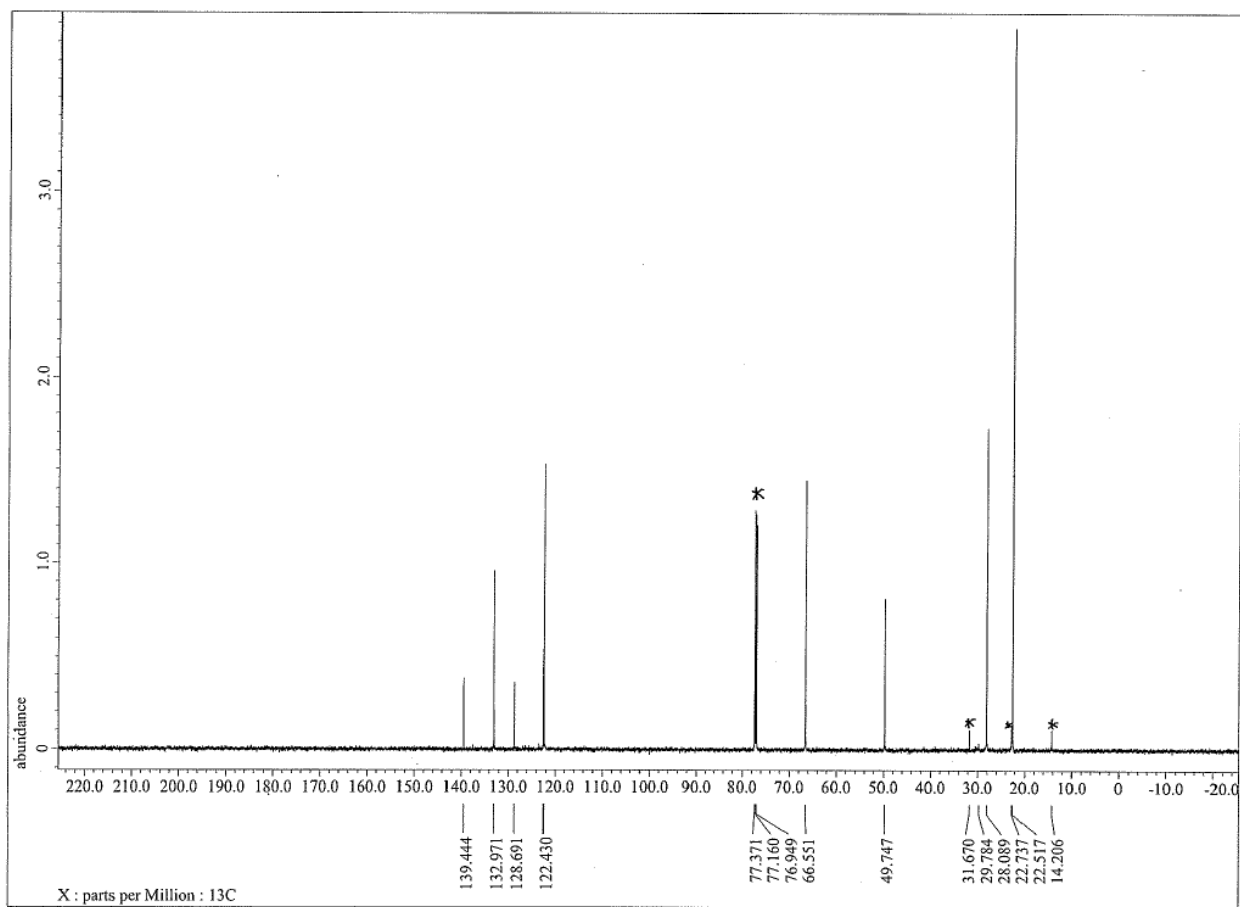


Fig. S49. ^{13}C NMR spectrum of **S4** in CDCl_3 at 25 °C. The peaks marked with * indicate residual solvents.

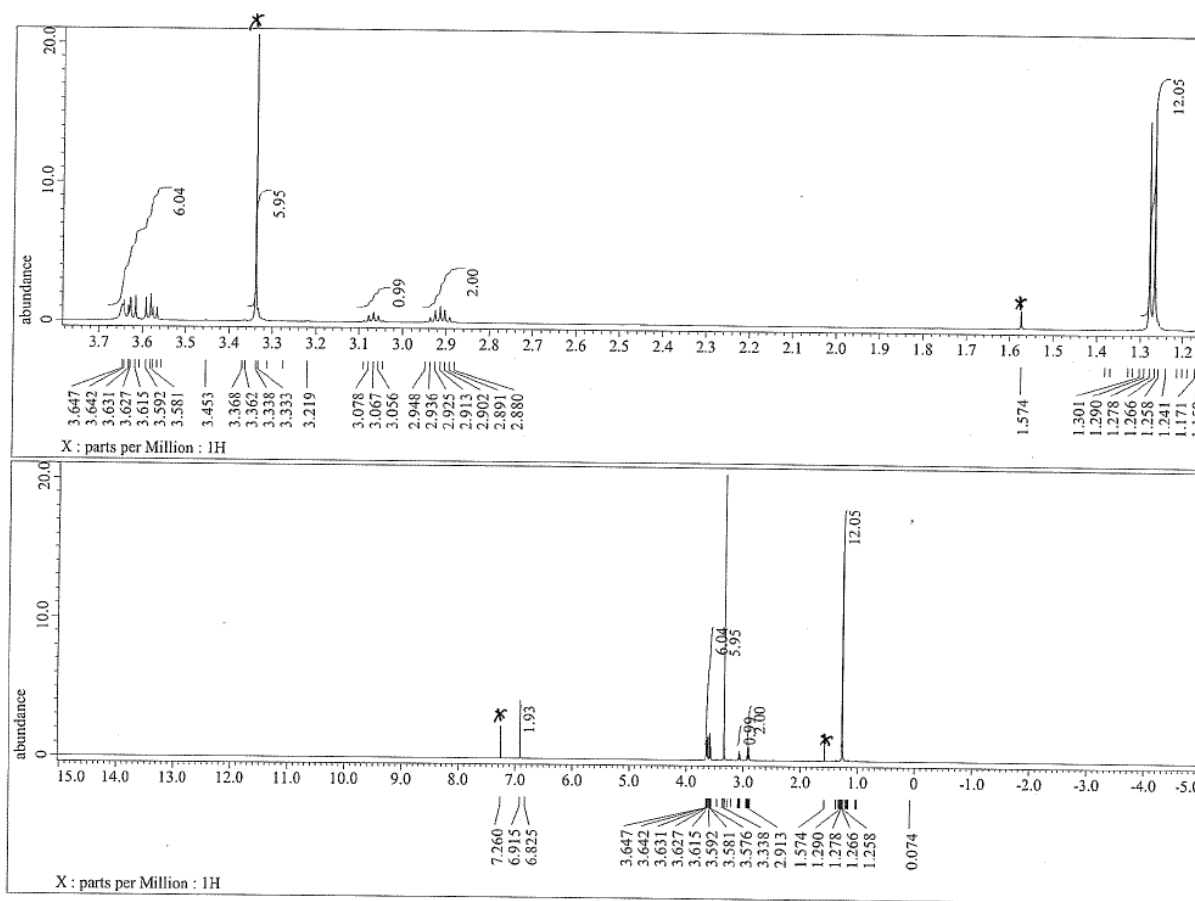


Fig. S50. ¹H NMR spectra of S5 in CDCl₃ at 25 °C. The peaks marked with * indicate residual solvents.

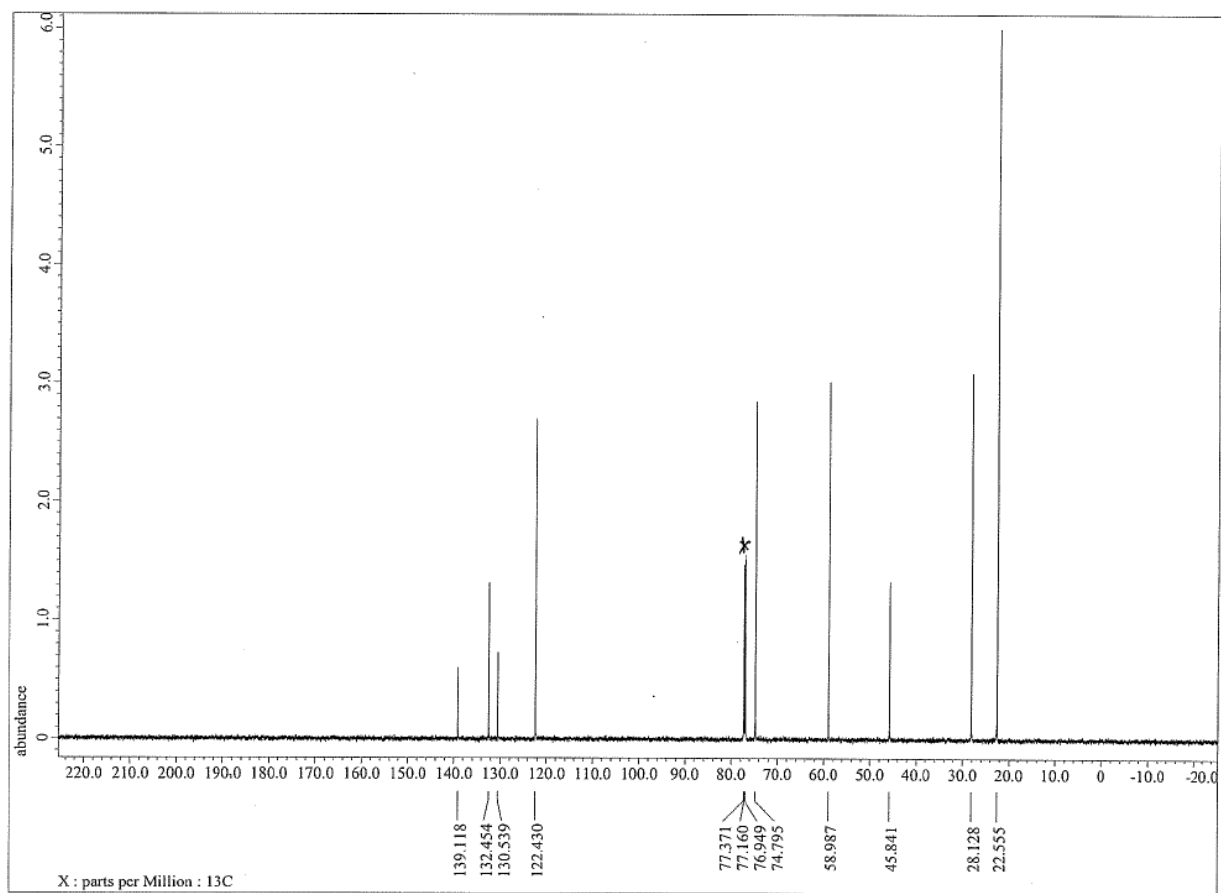


Fig. S51. ^{13}C NMR spectrum of **S5** in CDCl_3 at 25 °C. The peak marked with * indicates residual solvents.

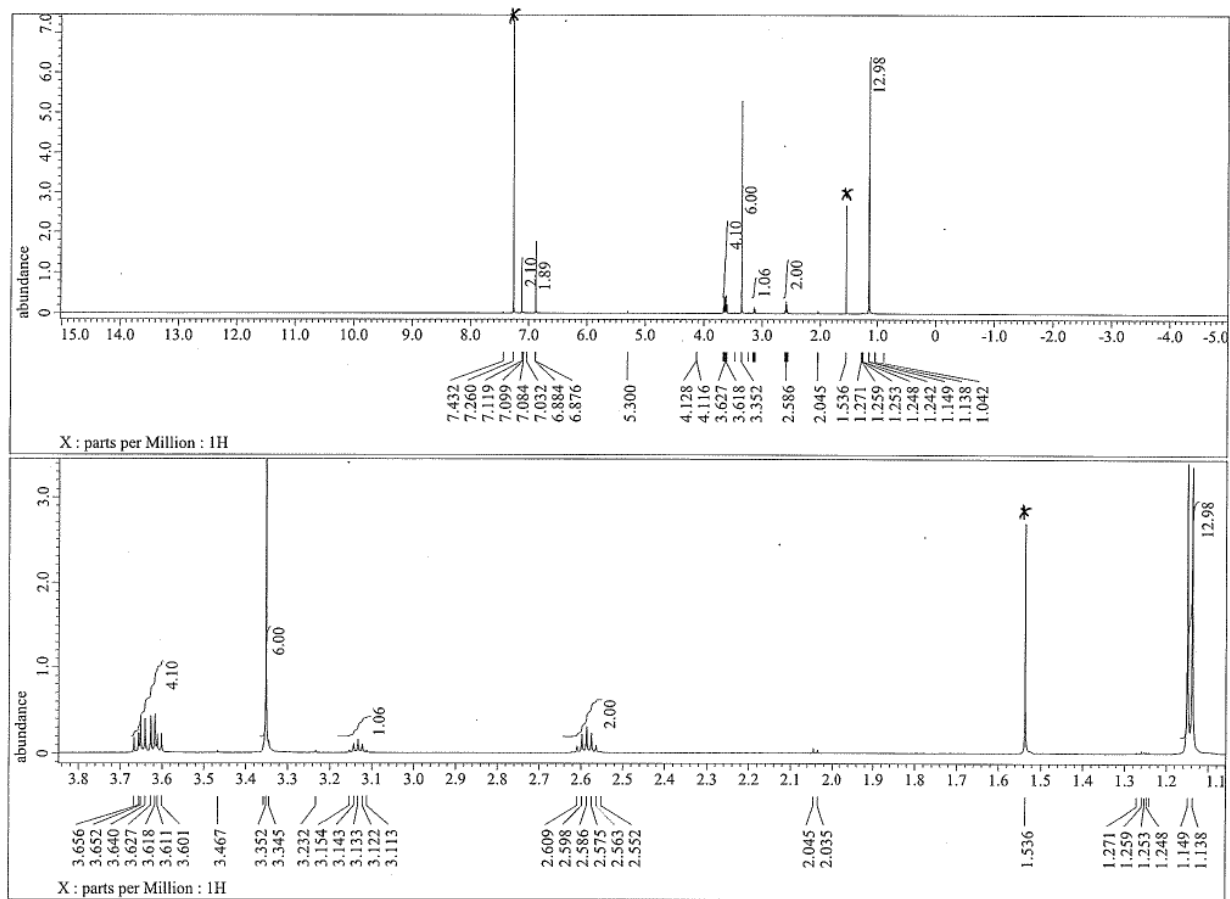


Fig. S52. ^1H NMR spectra of S6 in CDCl_3 at $25\text{ }^\circ\text{C}$. The peaks marked with * indicate residual solvents.

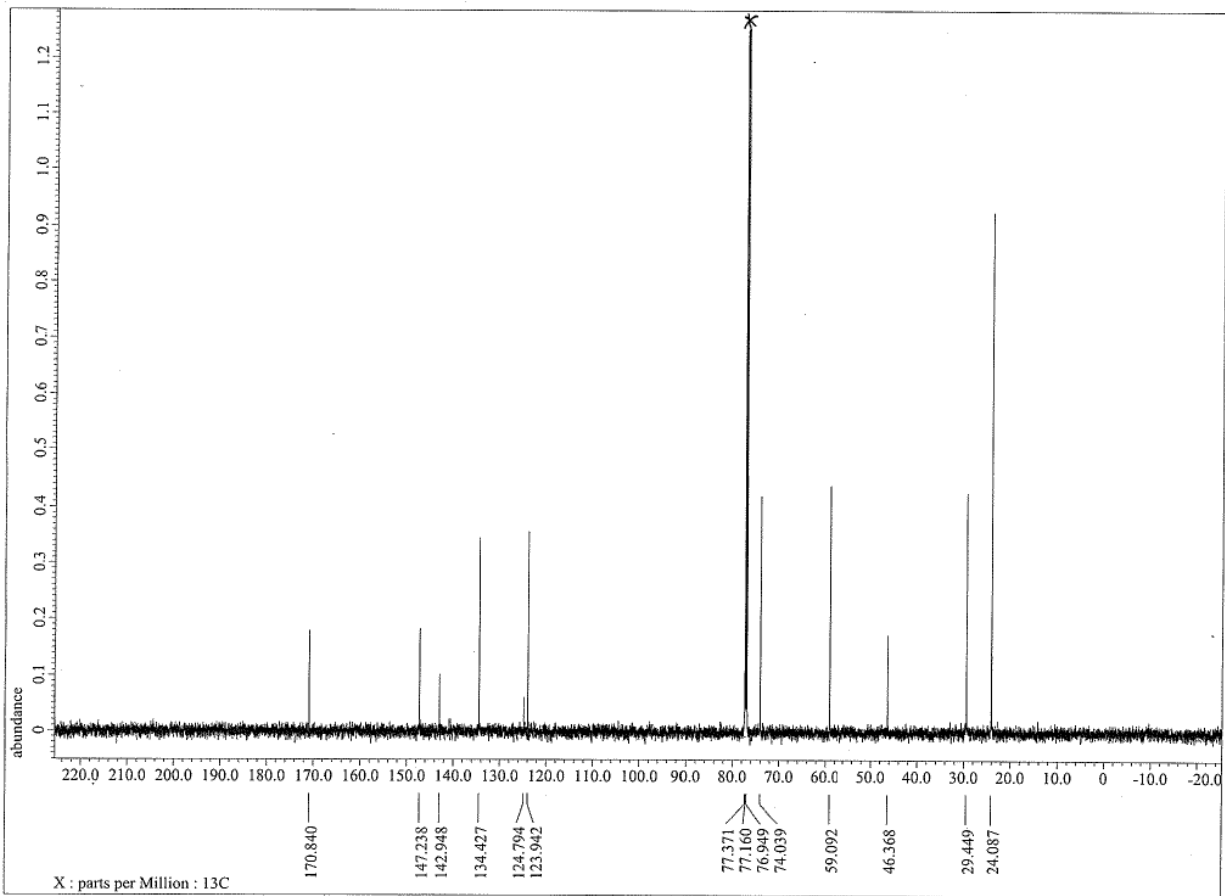


Fig. S53. ^{13}C NMR spectrum of **S6** in CDCl_3 at $25\text{ }^\circ\text{C}$. The peak marked with * indicates residual solvents.

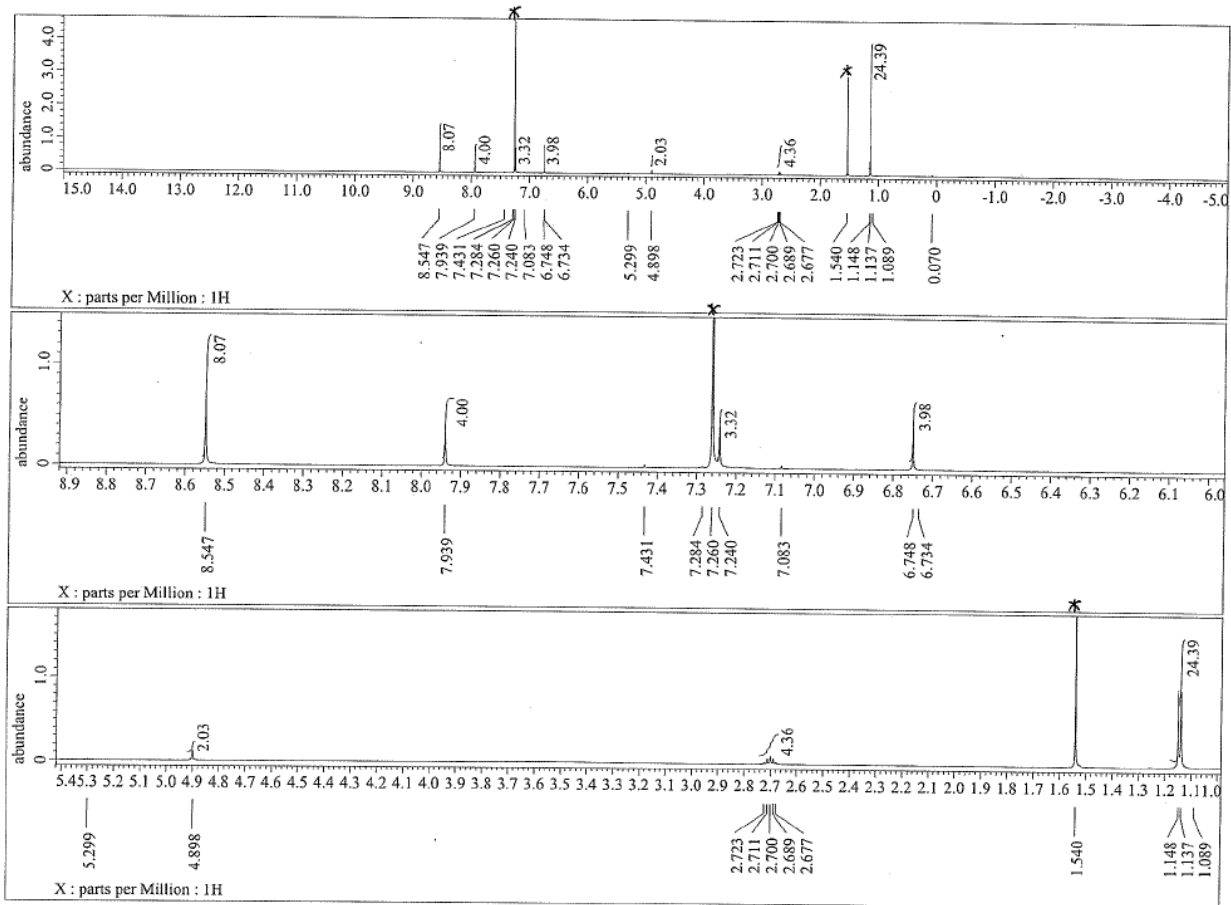


Fig. S54. ^1H NMR spectra of FLAP1 in CDCl_3 at $25\text{ }^\circ\text{C}$. The peaks marked with * indicate residual solvents.

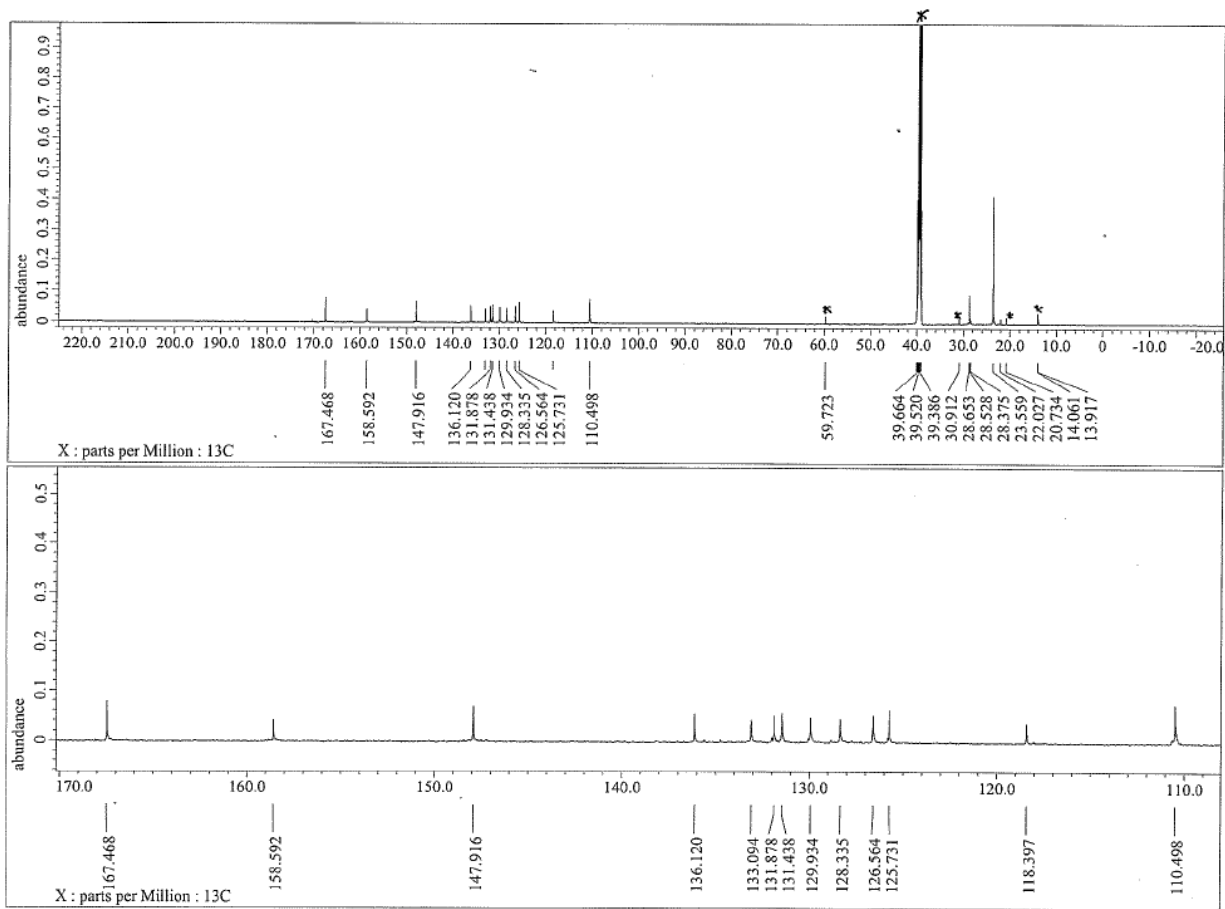


Fig. S55. ^{13}C NMR spectra of FLAP1 in $\text{DMSO-}d_6$ at $25\text{ }^\circ\text{C}$. The peaks marked with * indicate residual solvents.

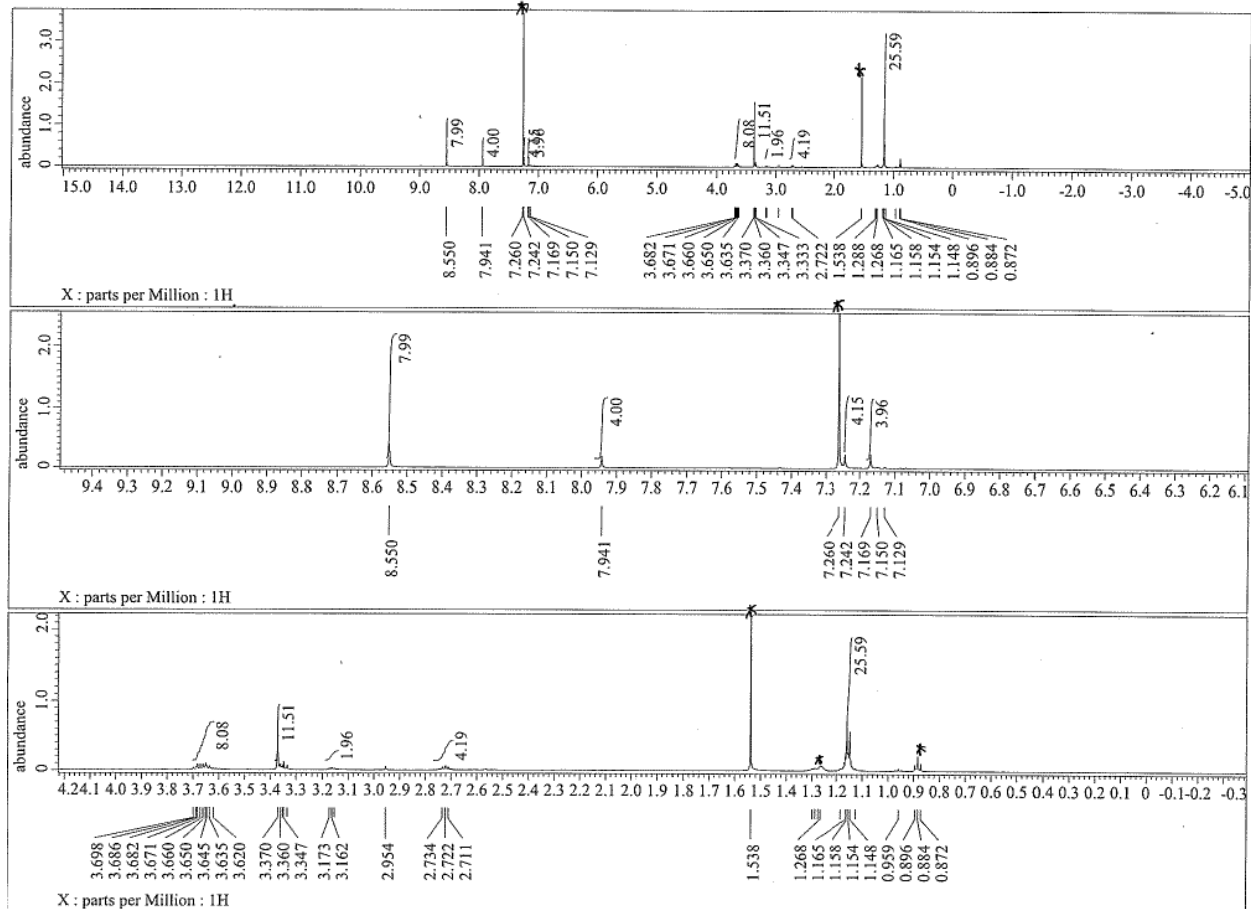


Fig. S56. ^1H NMR spectra of S8 in CDCl_3 at 25°C . The peaks marked with * indicate residual solvents.

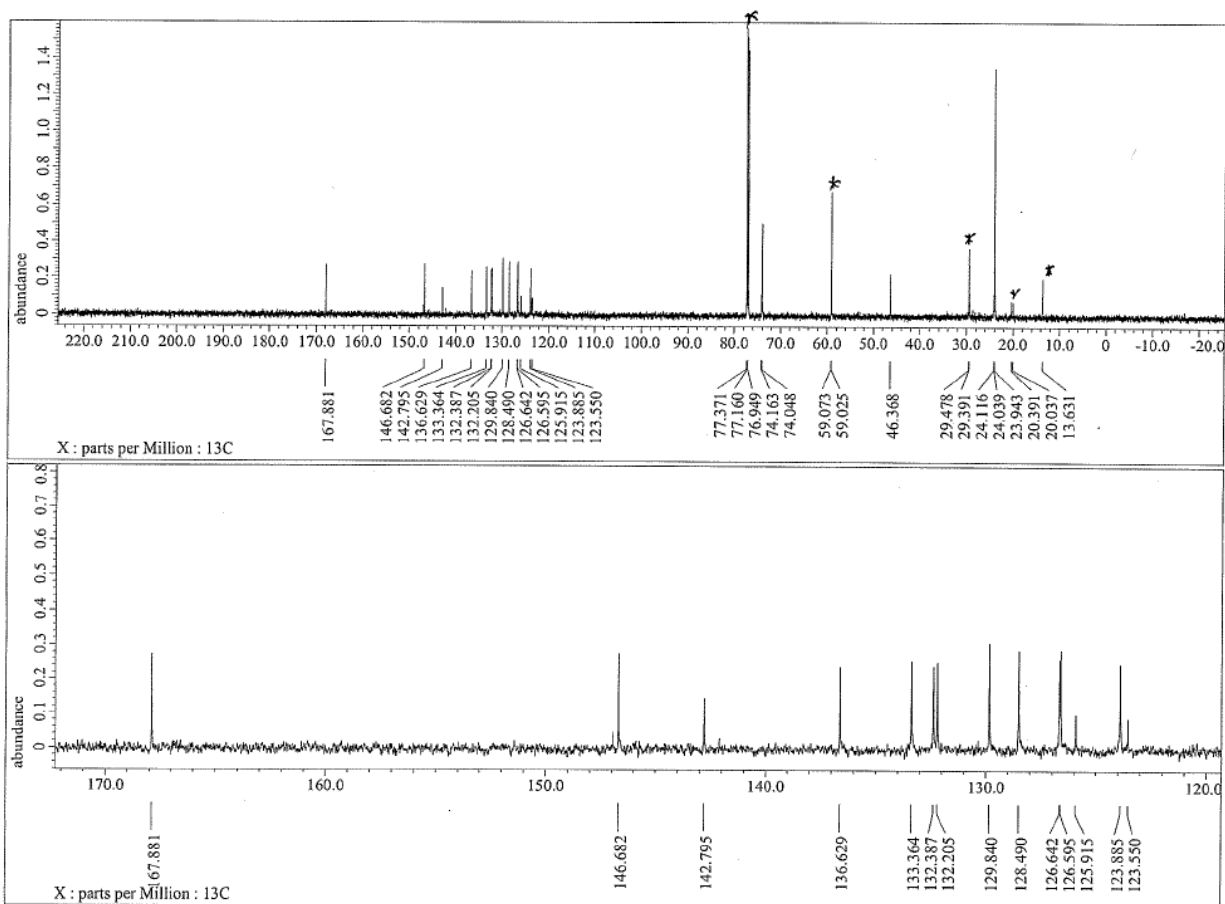


Fig. S57. ^{13}C NMR spectra of S8 in CDCl_3 at 25°C . The peaks marked with * indicate residual solvents.

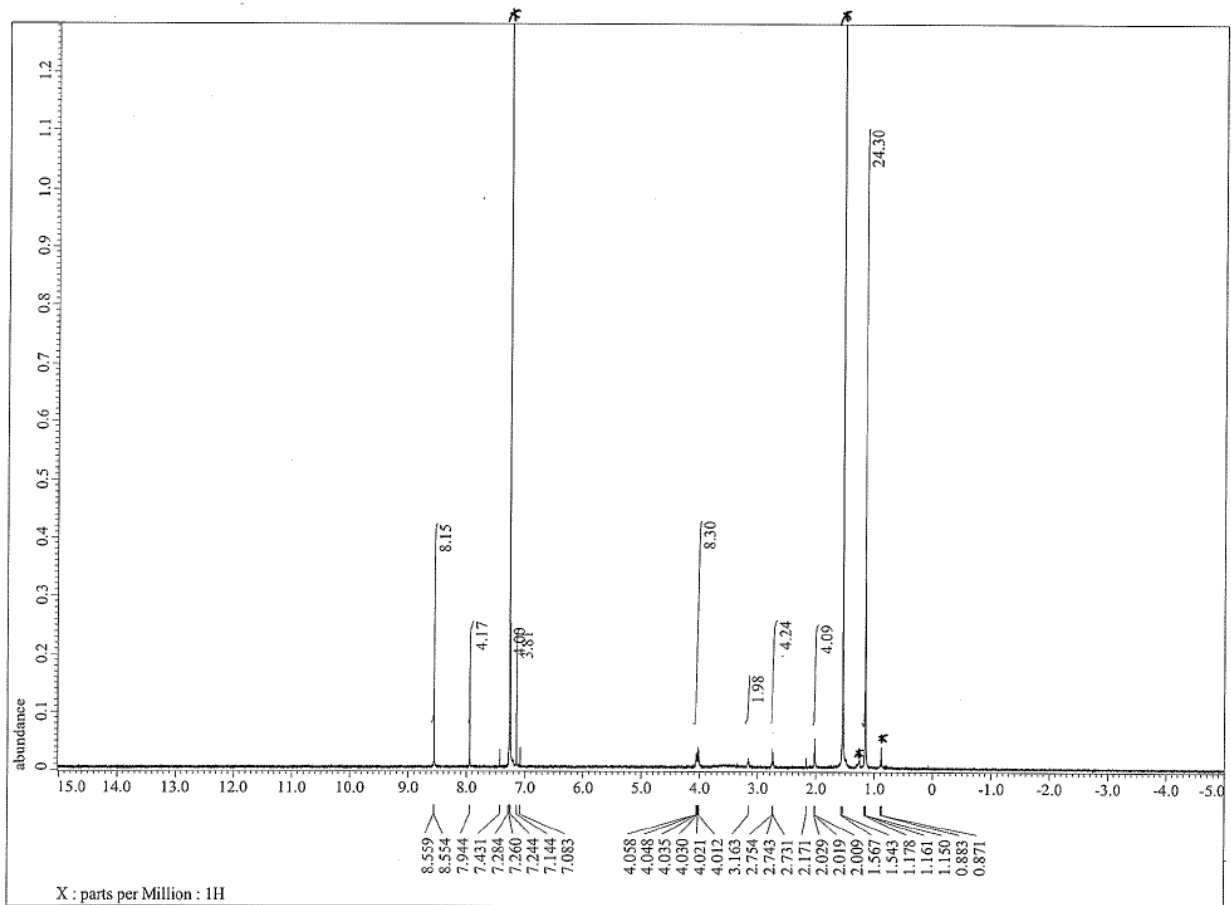


Fig. S58. ^1H NMR spectrum of **FLAP2** in CDCl_3 at 25 °C. The peaks marked with * indicate residual solvents.

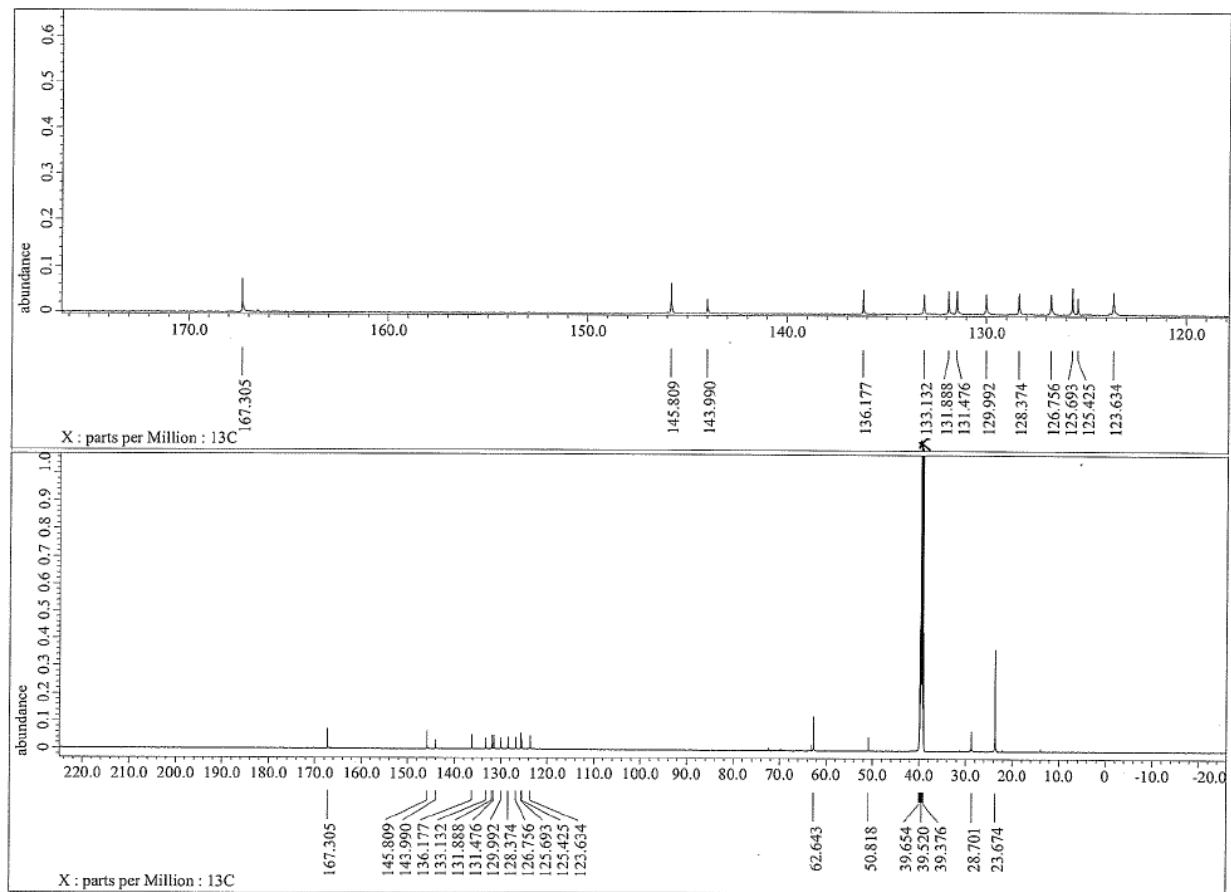


Fig. S59. ^{13}C NMR spectra of FLAP2 in $\text{DMSO-}d_6$ at $25\text{ }^\circ\text{C}$. The peak marked with * indicates residual solvents.

Mass spectra of new compounds

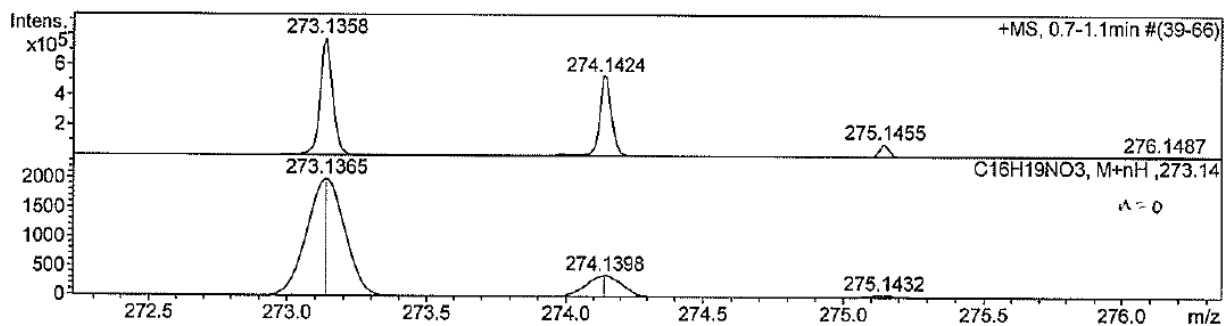


Fig. S60. HR-APCI-TOF mass spectra of S1. Top: observed, bottom: simulated.

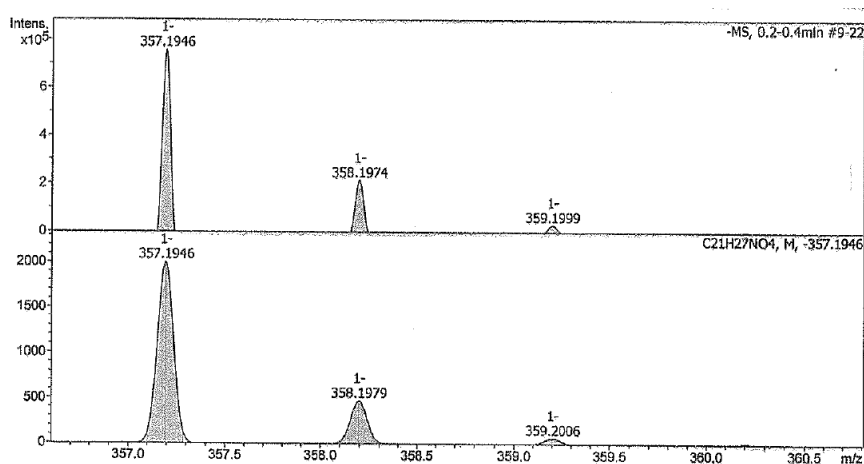


Fig. S61. HR-APCI-TOF mass spectra of S2. Top: observed, bottom: simulated.

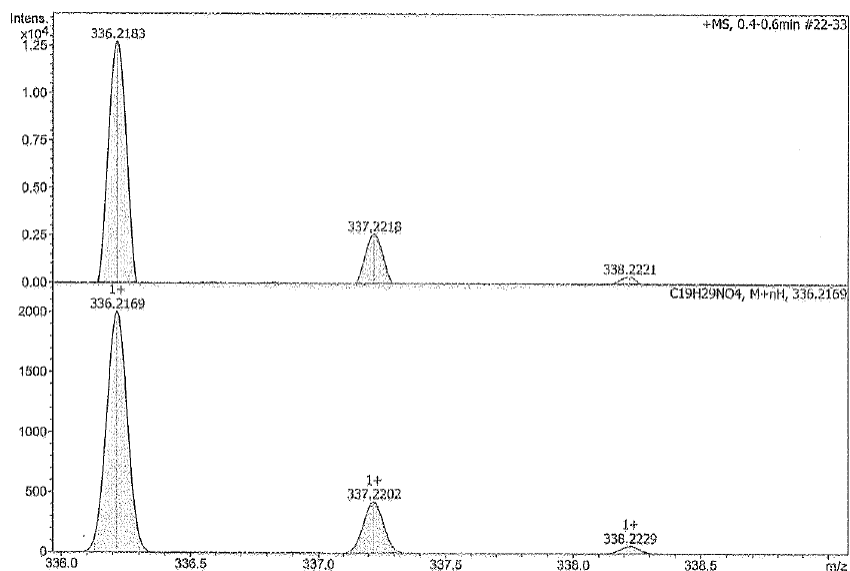


Fig. S62. HR-APCI-TOF mass spectra of S3. Top: observed, bottom: simulated.

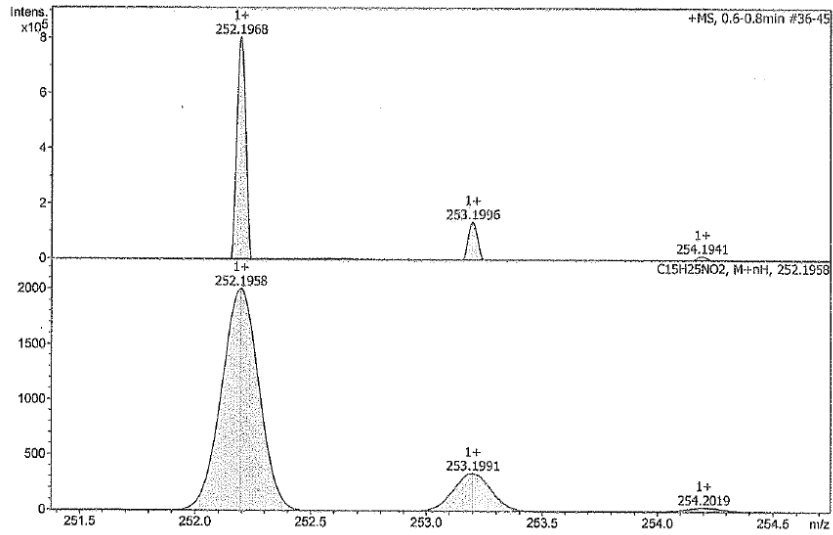


Fig. S63. HR-APCI-TOF mass spectra of S4. Top: observed, bottom: simulated.

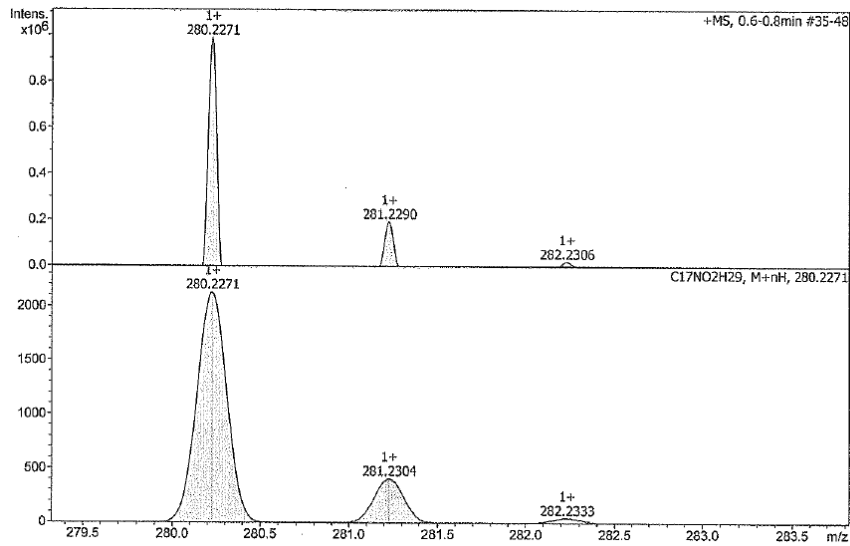


Fig. S64. HR-APCI-TOF mass spectra of S5. Top: observed, bottom: simulated.

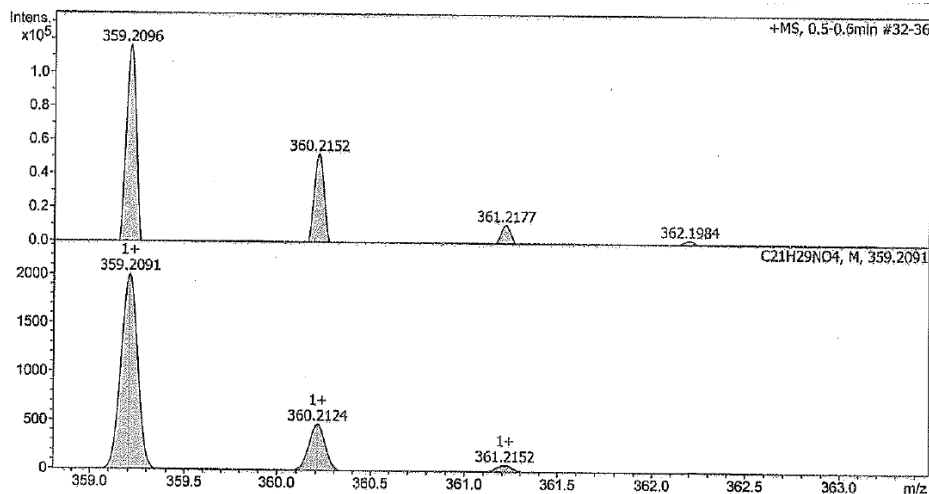


Fig. S65. HR-TOF mass spectra of S6. Top: observed, bottom: simulated.

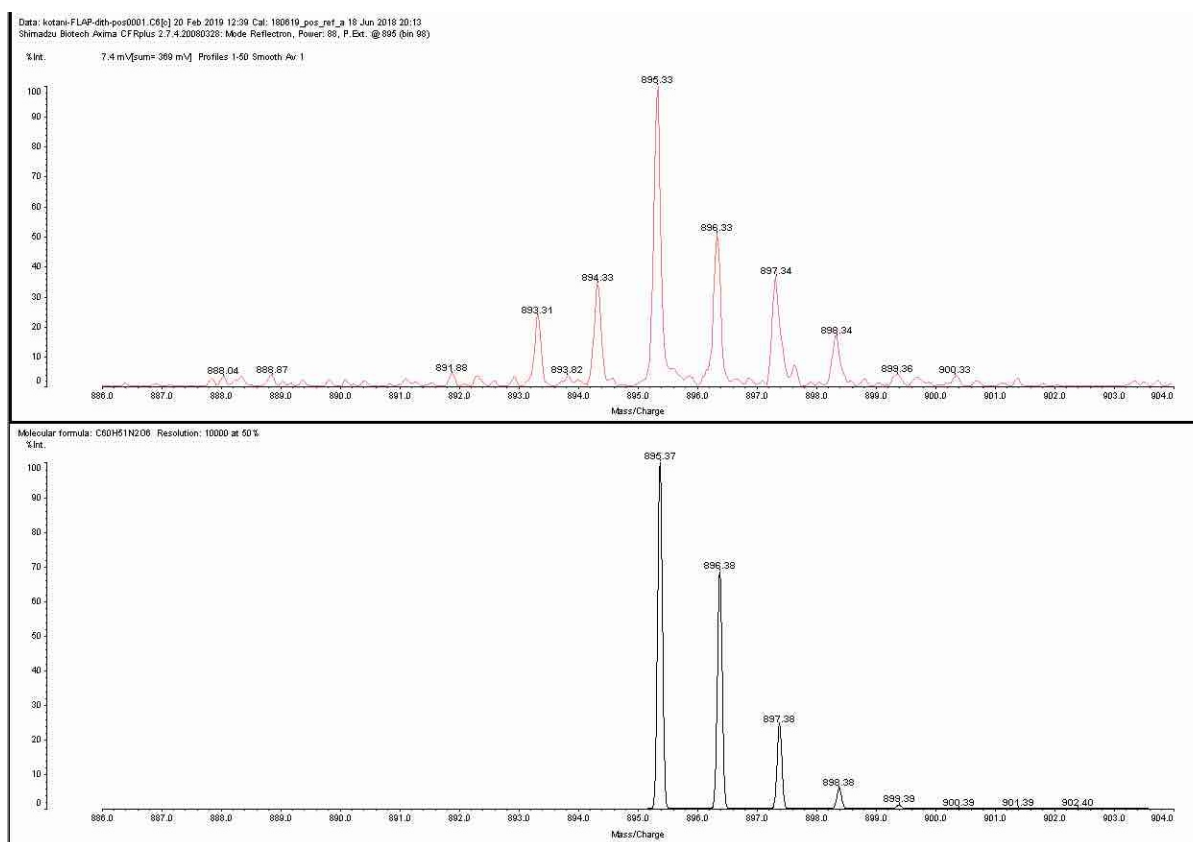


Fig. S66. HR-MALDI-TOF mass spectra of FLAP1. Top: observed, bottom: simulated.

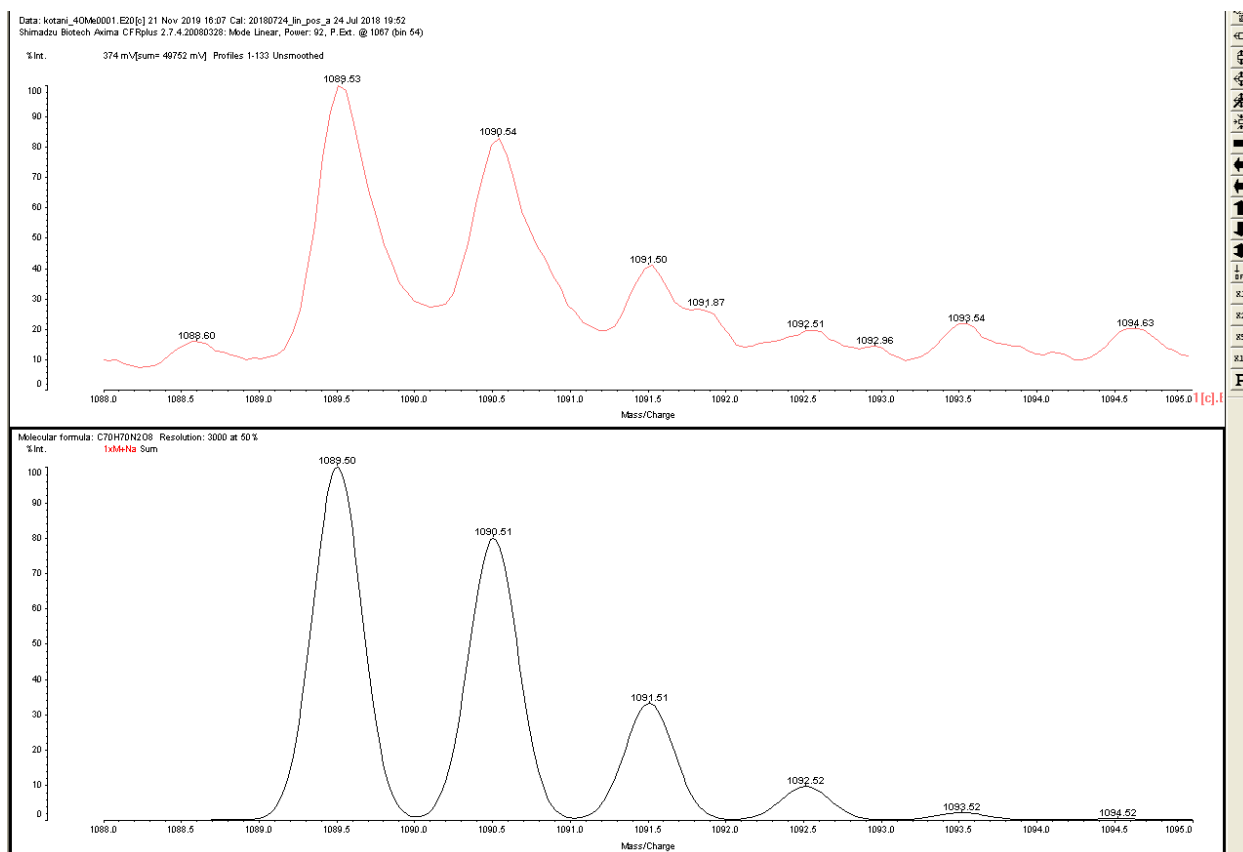


Fig. S67. HR-MALDI-TOF mass spectra of **S8**. Top: observed, bottom: simulated.

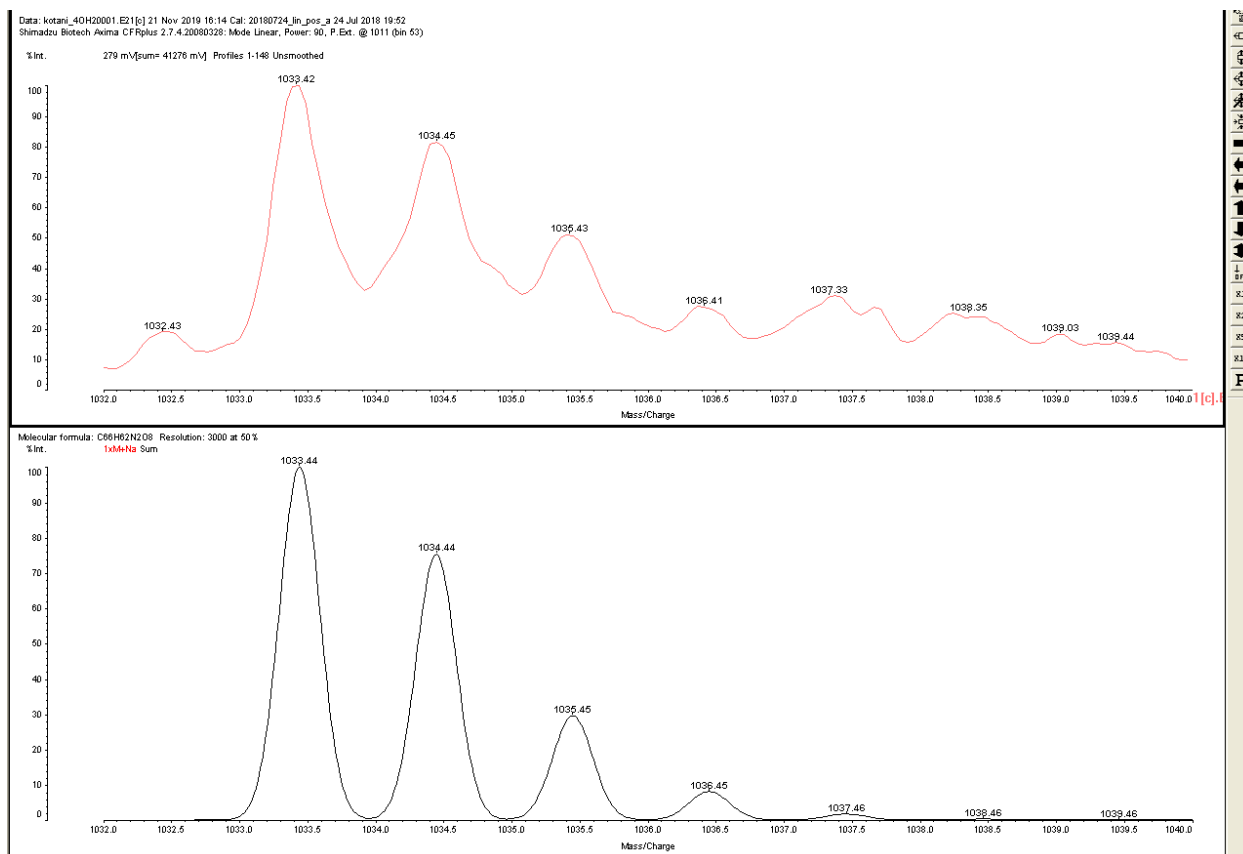


Fig. S68. HR-MALDI-TOF mass spectra of **FLAP2**. Top: observed, bottom: simulated.

Supplementary References

40. Gaussian 16, Revision A.03, M. J. Frisch, G. W. Trucks, H. B. Schlegel, G. E. Scuseria, M. A. Robb, J. R. Cheeseman, G. Scalmani, V. Barone, G. A. Petersson, H. Nakatsuji, X. Li, M. Caricato, A. V. Marenich, J. Bloino, B. G. Janesko, R. Gomperts, B. Mennucci, H. P. Hratchian, J. V. Ortiz, A. F. Izmaylov, J. L. Sonnenberg, D. Williams-Young, F. Ding, F. Lipparini, F. Egidi, J. Goings, B. Peng, A. Petrone, T. Henderson, D. Ranasinghe, V. G. Zakrzewski, J. Gao, N. Rega, G. Zheng, W. Liang, M. Hada, M. Ehara, K. Toyota, R. Fukuda, J. Hasegawa, M. Ishida, T. Nakajima, Y. Honda, O. Kitao, H. Nakai, T. Vreven, K. Throssell, J. A. Montgomery, Jr., J. E. Peralta, F. Ogliaro, M. J. Bearpark, J. J. Heyd, E. N. Brothers, K. N. Kudin, V. N. Staroverov, T. A. Keith, R. Kobayashi, J. Normand, K. Raghavachari, A. P. Rendell, J. C. Burant, S. S. Iyengar, J. Tomasi, M. Cossi, J. M. Millam, M. Klene, C. Adamo, R. Cammi, J. W. Ochterski, R. L. Martin, K. Morokuma, O. Farkas, J. B. Foresman, and D. J. Fox, Gaussian, Inc., Wallingford CT
41. J. L. Krinsky, A. Martínez, C. Godard, S. Castellón, C. Claver, Modular Synthesis of Functionalizable Alkoxy-Tethered N-Heterocyclic Carbene Ligands and an Active Catalyst for Buchwald–Hartwig Aminations. *Adv. Syn. Cat.* **356**, 460–474 (2014).
42. L. Zhang, X. Ren, Y. Zhang, K. Zhang, Step-Growth Polymerization Method for Ultrahigh Molecular Weight Polymers. *ACS Macro Lett.* **8**, 948–954 (2019).